SHAPE PRESERVING CONVERSION REACTIONS OF ALUMINA STRUCTURES USING METAL HALIDES: STRUCTURES, KINETICS, AND APPLICATIONS

A Dissertation
Presented to
The Academic Faculty

By

Taylor McLachlan Shapero

In Partial Fulfillment
Of the Requirements for the Degree
Doctor of Philosophy in Materials Science and Engineering

Georgia Institute of Technology

August 2016

SHAPE PRESERVING CONVERSION REACTIONS OF ALUMINA STRUCTURES USING METAL HALIDES: STRUCTURES, KINETICS, AND APPLICATIONS

Approved by:

Dr. Kenneth H. Sandhage, Advisor
School of Materials Science and Engineering
Georgia Institute of Technology

Dr. Lawrence Bottomley
School of Chemistry and Biochemistry
Georgia Institute of Technology

Dr. Hamid Garmestani
School of Materials Science and Engineering
Georgia Institute of Technology

Dr. Meilin Liu
School of Materials Science and Engineering
Georgia Institute of Technology

Dr. Preet Singh
School of Materials Science and Engineering
Georgia Institute of Technology

Date Approved: October 23, 2015

For my ever-patient, loving husband, Sam.

ACKNOWLEDGEMENTS

This work could not have been completed without the tremendous amount of support I have received over the course of my studies at Georgia Tech. First and foremost, I must thank my husband, Sam, for being my greatest cheerleader, editor, and therapist. He has been by my side since we met on our first day as PhD students at Georgia Tech and helped me stay on my feet anytime I thought I was falling. Without his love, support, and advice I would not have made it this far.

My team of supporters is much larger than my husband alone. My parents and grandparents have all shown enormous faith and patience in me being able to accomplish anything I set my mind to do. They have never doubted me or waivered in support and are always willing to lend a listening ear when I doubted myself or showed excitement over progress. They made it possible for me to obtain a debt-free world-class education without which, this journey would have been far more difficult. My sisters have always been my inspiration. Their excitement over scientific and mathematic fields motivated me to follow them and become a scientist and engineer. Seeing their triumphs always allowed me to realize that I was capable of pursuing equally challenging quests. I could not trade my big sisters for the world.

Still, I've relied on a much larger team of supporters than my husband, parents, grandparents, and sisters. The rest of my family, my step families, in-laws, and other relatives, deserves acknowledgement here for their unwavering encouragement and love. My friends, old and new, have also provided me great reinforcement and loving words that have carried me through. I am indebted to all of my family and friends for seeing me

through to this moment and I can only hope that my future career will allow me to improve the world around them.

My success as a PhD student in Materials Science and Engineering was not possible without the gracious, unending, and tireless support of my advisor, Dr. Ken Sandhage. His passion for knowledge and the materials science field has always motivated me to be the best scientist and engineer I can be, and his determination to see every task through to the end will always inspire me. With him, I have been undeservingly fortunate to not worry for a moment about research ideas hindering my success. I would also like to thank the other members of my dissertation committee for giving their time and advice to help me succeed.

I would especially like to thank Dr. Daniel Berrigan for his willingness to work with me, his technical expertise, and his kindness. I want to credit Dr. Samuel Shian for teaching me the basics on which my project was built. Other lab mates including Dr. Yunshu Zhang, Dr. Ye Cai, Dr. Yunnan Fang, Dr. Samuel Shian, Dr. David Lipke, Dr. Jonathan Vernon, Dr. Stanley Davis, Dr. Craig Cameron, Dr. Ari Gordin, Dr. Brandon Goodwin, Dr. Philip Brooke, Ben deGlee, and Patrick Shower were each instrumental to my success and I want to thank them for their scientific and technical advice and willingness to work on ideas together.

I want to thank several individuals at the Air Force Research Lab (AFRL) at Wright-Patterson Air Force Base for their support and advice. Dr. Michael Durstock's team including Dr. Tae-Sik Kang, Dr. Giorgio Bazzan, Dr. Benjamin Leever, and James Deneault, and also Dr. Rajesh Naik, Dr. Matthew Dickerson, and Dr. Lawrence Drummy helped me realize the need for substantial open and collaborative research efforts to obtain

the most impactful and useful results. The community at AFRL is always willing to help and discuss projects and technical issues and for that, I am extremely grateful.

I am also grateful for the support I have received from Georgia State University Perimeter College's Math, Computer Science, and Engineering Department. As a tenure-track Instructor of Engineering, I have been able to work with a very supportive and engaged faculty, and I have confirmed that my passion lies in being in the classroom and working with students who are learning fundamental engineering and critical thinking skills.

Finally, I am grateful for the financial support provided to me by multiple organizations. The Philanthropic Educational Organization (P.E.O.) Scholar Award and the family of Betty Cook Karrh who endowed the award I received were quite generous in supporting my success as a female pursuing a doctoral degree. Notably, the P.E.O. Georgia Chapter B's desire to for me to succeed provided me great motivation. I also received support from the University System of Georgia's Tuition Assistance Program for employees. This research was conducted as part of the Air Force Center of Excellence on Bio-nano-enabled Inorganic/Organic Nanocomposites and Improved Cognition (BIONIC) which was supported by the Materials and Manufacturing Directorate and the Human Effectiveness Directorate of AFRL, Georgia Tech, and Air Force Office of Scientific Research (Award No. FA9550-09-1-0162) with Dr. Charles Lee as program manager.

TABLE OF CONTENTS

Page

LIST OF TABLES

LIST OF FIGURES

LIST OF SYMBOLS AND ABBREVIATIONS

N719	cis-di(thiocyanato)-N-N'-bis(2,2'-bipyridyl-4-carboxylic acid-4'-tetrabutylammonium carboxylate) ruthenium (II)
3-D	three dimensional
BASIC	Biological Assembly and Shape-preserving Inorganic Conversion
h	hour
TEM	transmission electron microscopy
DSSC	dye-sensitized solar cell
TCO	transparent conducting oxide
HOMO	highest occupied molecular orbital
LUMO	lowest unoccupied molecular orbital
AAO	anodic aluminum oxide
TH-AAO	through-hole anodic aluminum oxide
TH-PA-AAO	through-hole, phosphoric acid-derived anodic aluminum oxide
TH-SA-AAO	through-hole, sulfuric acid-derived anodic aluminum oxide
FTO	fluorine-doped tin oxide
FEG	field emission gun
SEM	scanning electron microscopy
XRD	X-ray diffraction
J-V	current density-voltage
AM 1.5G	air mass 1.5 global
TH-OA-AAO	through-hole, oxalic acid-derived anodic aluminum oxide

EDX	energy dispersive X-ray spectroscopy
TE	transmission electron
SE	scanning electron
HRTE	high-resolution transmission electron
SAED	selected area electron diffraction
ED	electron diffraction
V_{OC}	open-circuit voltage
J_{SC}	short-circuit current density
IV	current-voltage
1-D	one dimensional
MWTNT	multiwall titania nanotubes
SWTNT	single wall titania nanotubes
UV-Vis	ultraviolet-visible
FF	fill factor
η	efficiency
HTXRD	high-temperature X-ray diffraction
ALD	atomic layer deposition
TOF-SIMS	time-of-flight secondary ion mass spectrometry
SCM	shrinking core model

SUMMARY

Porous anodic aluminum oxide nanostructures provide hexagonally ordered arrays of pores with periodic distribution and tunable size and length. The research in this dissertation introduces a new process for partially converting the chemistry of the aluminum oxide nanostructure to titanium dioxide while retaining shape through a gaseous metal halide (TiF_4) reactive conversion process. By this process, oriented single and multi-wall titania nanotube arrays with tailored structures can be formed. This vapor-based process allows titania formation within small pores inaccessible to liquid-based approaches through an intermediary $TiOF_2$ product. The research explores applications of converted titania structures, including dye-sensitized solar cells. The reactive conversion kinetics of Al_2O_3 into $TiOF_2$ was studied to reveal two kinetic regimes likely limited by chemical reaction and solid-state diffusion allowing a stronger understanding of how the conversion reaction might be optimized in future applications. Other metal fluoride reactions with anodic aluminum oxide (Al_2O_3) are also studied (including the successful conversion of Al_2O_3 into Nb_2O_5) showing the versatility of converting anodic aluminum oxide for applications requiring certain other oxide materials.

CHAPTER 1 GAS/SOLID REACTIVE CONVERSION SYNTHESIS OF HIGH-ASPECT-RATIO, ALIGNED NANOTUBE ARRAYS FOR DYE-SENSITIZED SOLAR CELLS

1.1 Summary

The objective of this chapter is to demonstrate, for the first time, that a synthetic chemical conversion process, involving a novel shape-preserving, metathetic gas/solid reaction can be used to synthesize TiO_2 nanostructures via the controlled conversion of aluminum oxide (Al_2O_3) nanostructures. The Al_2O_3 template was exposed to gaseous TiF_4 followed by humid O_2(g). TiF_4 is a reactive halide which sublimes at 285°C and reacts with Al_2O_3 to form $TiOF_2$ and Al-bearing by-products. This reactive behavior has been harnessed to produce, in a time and temperature dependent fashion, a $TiOF_2$-bearing layer on exposed surfaces of Al_2O_3. Subsequent oxygenation in humid O_2(g) and sintering yielded a continuous, conformal, anatase TiO_2 product. Dissolution of the remaining underlying Al_2O_3 template and Al-bearing by-products produced high-aspect-ratio, aligned titania nanotube arrays. The TiO_2 nanotube arrays synthesized using this methodology were integrated into dye-sensitized solar cells (using Ru-based N719 dye) with light harvesting efficiencies of 4.4 ± 0.3%.

1.2 Introduction

1.2.1 Introduction to Reactive Conversion Processes

Three-dimensional chemical conversion of nanostructured templates is an attractive

approach for producing complex structures due to the wide range of intricate 3-D structures of specific chemistries available via mass production and the scalability of many chemical conversion methods.[4-7] Primarily, the potential capability to mass produce nanostructured devices with tailored chemistry in a gaseous environment is a great advantage due to the ability of gases to readily penetrate fine-scale porosity or narrow cavities with high diffusivity. The mass diffusivity of gases through small pores is typically at least one order of magnitude greater than bulk diffusivity of liquids, and several orders of magnitude greater than liquid diffusivity through small pores.[8] Previous research has resulted in the BASIC process, which stands for **B**iological **A**ssembly and **S**hape-preserving **I**norganic **C**onversion.[9] BASIC introduces the chemical tailoring of silica structures, such as diatom frustules, while maintaining the original structure. One successful method for changing the chemistry of silica-based diatom frustules was a gas/silica displacement reaction method where silica frustules were converted into replicas of MgO (via an oxidation-reduction displacement reaction with Mg(g)) or TiO_2 (via a metathetic displacement reaction with TiF_4(g)).[3,4]

The following net shape-preserving, metathetic, gas-solid displacement reaction was examined to convert SiO_2 diatom frustules into TiO_2 replicas.[3,4]

$$TiF_4(g) + SiO_2(s) \rightarrow TiO_2(s) + SiF_4(g) \quad (1)$$

This net reaction allowed for the formation of the anatase polymorph of titania with the release of silicon fluoride vapor. Multiple species of diatoms and other siliceous precursors were examined including high aspect ratio structures (*Corethron criophilum* diatom frustule) and synthetic scaffold structures.[10] The net reaction was realized as a sequence of two sub-reactions. *Aulacoseira* diatom frustules (Figure 1.1(a)) were initially exposed to TiF_4(g) under a carefully chosen temperature (350°C), reaction time (2 h), and SiO_2 (diatom) to TiF_4 weight ratio in an otherwise inert atmosphere.[3] This resulted in a solid $TiOF_2$ product (Figure 1.1(b)). At higher reaction temperatures (500°C – 700°C) or TiF_4-SiO_2 molar ratios ≥ 4.9:1, titania was directly generated, but, the starting diatom frustule shape was not preserved and relatively coarse plate-shaped crystals were produced.

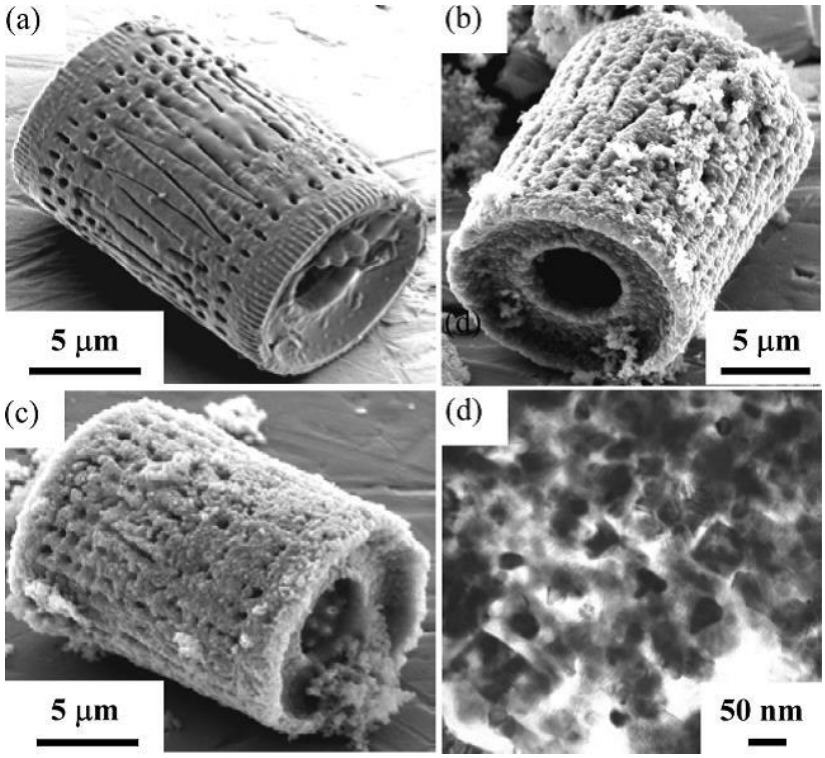

Figure 1.1. Secondary electron images of *Aulacoseira* diatom frustules: (a) before treatment; (b) after exposure to TiF_4(g) for 2 h at 350 °C; (c) after subsequent exposure to pure O_2 for 2 h at 350 °C. (d) A transmission electron image of a cross-section of a frustule after exposure to TiF_4(g) for 2 h at 350 °C and then to pure O_2 for 2 h at 350 °C. Reproduced from Unocic, *et al.* with permission from The Royal Society of Chemistry.[3]

In the formation of $TiOF_2$, one or more of the following reactions was likely followed, as each has a considerably negative Gibbs free energy change:

$$TiF_4(g) + \frac{1}{2}SiO_2(s) \rightarrow TiOF_2(s) + \frac{1}{2}SiF_4(g) \quad (2)$$

$$TiF_4(g) + \frac{2}{3}SiO_2(s) \rightarrow TiOF_2(s) + \frac{1}{3}Si_2OF_6(g) \quad (3)$$

$$TiF_4(g) + SiO_2(s) \rightarrow TiOF_2(s) + SiOF_2(g) \quad (4)$$

Subsequently, specimens were given a second heat treatment at 350°C for 2 h in pure, flowing oxygen in order to convert the titanium oxyfluoride frustules (Figure 1.1(c)) into titanium dioxide by the following reaction:[3]

$$TiOF_2(s) + \frac{1}{2}O_2 \rightarrow TiO_2(s) + F_2(g) \quad (5)$$

A longitudinal TEM cross-section of the resulting oxygen-treated nanostructure is shown in Figure 1.1(d). The specimen consisted of a porous network of fine oxide crystals (< 100 nm in size), and was found to be anatase by electron diffraction.

Unocic, *et al.*[3] were the first to demonstrate a metathetic halide gas-solid reaction that could convert a biologically self-assembled 3-D structure into a new nanocrystalline material without loss of the bioclastic shape or fine features. Nonetheless, they noted that such shape-preserving metathetic reactions could also be conducted on synthetic structures. They also showed that fluorine-doped TiO_2 could be obtained when oxygenation was only partially completed and was useful in inducing rapid hydrolysis of certain organophosphorous esters (often found in pesticides) at mild pH and temperatures and in the absence of light.[11]

1.2.2 Applications of TiO_2 Nanostructures Formed by Gas/Solid Reaction

Titanium dioxide (TiO_2) possesses many varied technological uses due to its optical,[12] chemical,[13] electrical,[14] photochemical,[15] and photovoltaic properties.[16] Various morphologies of TiO_2-based materials can be appealing for use in numerous applications (*e.g.*, nanotubes for high throughput (photo)catalysts, adsorbants, and dye-sensitized solar cells (DSSCs),[17-19] nanorods for bulk heterojunction solar cells,[20] nanowires or nanotubes for batteries,[21,22] nanotubes for sensitive and rapid gas detectors,[17] nanoparticles for precise fluid flow control devices,[23] functionalized hierarchical membranes for selective (bio)molecular separation,[24] and sol-gel matrices for biosensing[25]). In particular, aligned, high-aspect-ratio, nanotubular TiO_2-based materials can be appealing structures in these applications by providing relatively direct migration pathways for electrons or other species.

The objectives of the present work are: i) to demonstrate, for the first time, that a synthetic chemical conversion process, involving a shape-preserving, metathetic gas/solid reaction, can be used to synthesize TiO_2 nanostructures via the controlled conversion of aluminum oxide (Al_2O_3) nanostructures and ii) to explore their applicability in DSSCs. Possible convertible, nanostructured Al_2O_3 could include porous anodic alumina, nanotubes,[26] nanobelts,[27] nanobricks,[28] and nanocones,[29] among others. While many nanostructures of TiO_2 are already known, this process could produce new sizes and shapes of available TiO_2 nanostructures for many applications. Benefits of this gas/solid reaction over other coating or conversion methods include that the method presented herein is potentially capable of mass-scale production of TiO_2 nanostructures, uses gases as opposed to liquids, and is highly controllable.

1.2.3 Dye-Sensitized Solar Cells

A primary application of the TiO_2 nanotube arrays is in dye-sensitized solar cells.[30-33] The typical design (not to scale) of an aligned array DSSC is given in Figure 1.2. This 2-D schematic shows TiO_2 nanotubes/rods in the semiconducting layer. In the cell, light passes through a transparent conducting oxide (TCO) and a thin, transparent TiO_2 semiconducting layer before being absorbed by the dye (typically ruthenium based). Once absorbed, the electrons within the dye are excited from the highest occupied molecular orbital (HOMO or $E_{dye}(+/0)$) to the lowest unoccupied molecular orbital (LUMO or $E_{dye}(+/*)$) as shown in Figure 1.3. Electrons are then injected into the lower energy Fermi level of the TiO_2 and finally diffused to the electrode or TCO and through an external circuit where the extra energy is utilized before migrating to the counter electrode. At this point, it is important to understand the purpose of the electrolyte. Because the dye has given up electrons to the TiO_2, the electrolyte supplies electrons to replenish the dye molecules to their original state. The now oxidized and electron-deficient electrolyte recovers missing electrons by migrating toward the counter electrode, or cathode. Electrons migrating through the circuit reach the counter electrode and recombine with the oxidized electrolyte.

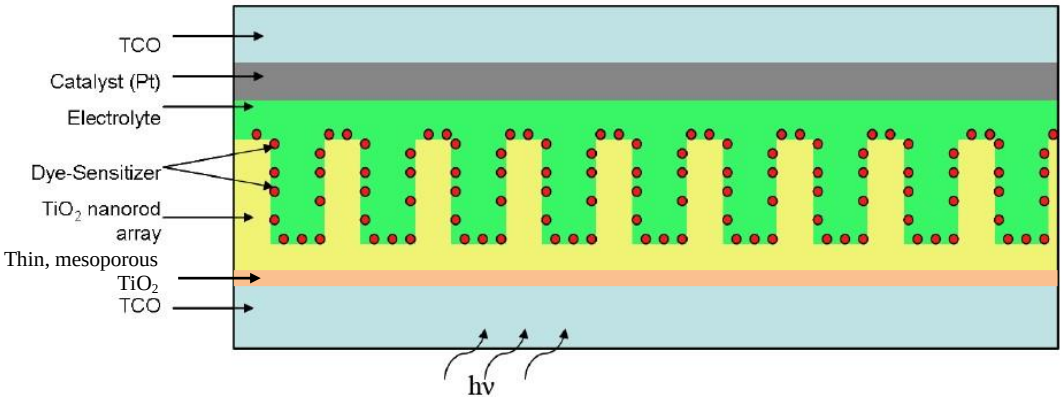

Figure 1.2. Schematic of layers in a dye-sensitized solar cell.

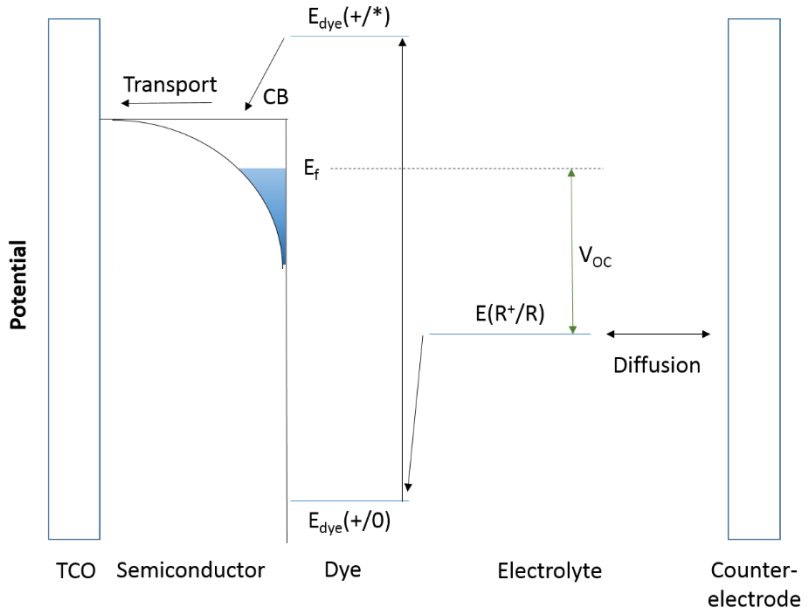

Figure 1.3. A kinetic diagram showing the essential DSSC processes as solid black arrows. The photovoltage (V_{OC}) generated depends on the difference between the redox potential, $E(R^+/R)$, of the electrolyte and the Fermi level, E_f, of TiO_2.

While this chapter will focus on using TiO_2 in the DSSC, other oxides have been tested in the literature. TiO_2 has traditionally served as the semiconductor of choice due to its stability, robustness, abundance, nontoxicity, and low price.[1] Like TiO_2 (E_g= 3.23 eV, anatase), ZnO (E_g= 3.37 eV, rock salt structure), and Nb_2O_5 (E_g= 3.493 eV, monoclinic structure) are also good candidates for filling the semiconductor role, for multiple reasons. All three of these metal oxides have dissimilar valence and conduction bands orbitals (In TiO_2, the valence band consists of hybridized oxygen 2p/titanium 3d orbitals while the conduction band is pure titanium 3d orbitals),[1] and can strongly influence the photovoltage, the fill-factor, the incident photon-to-current conversion efficiency (ICPE), and the efficiency of electron injection and collection.[34]

The model for the DSSC in this chapter varies from original designs.[16,35-37] A major change within the architecture is that of the solid semiconducting (TiO_2) layer—the

electrolyte is liquid and able to infiltrate the TiO_2 structure. The application of semiconducting nanostructures in DSSCs has been widely studied since the early 1990's. Incorporating TiO_2 thin films as the semiconductor, Brian O'Regan and Michael Gratzel invented the Gratzel Cell, the first operational DSSC with >1% efficiency, in 1991.[16] O'Regan and Gratzel initially intended DSSCs as a reasonably affordable alternative to tradition *p-n* junction photovoltaics whose expense prohibited their profitable manufacture and sale on a large scale. Although dye-sensitized solar cells had been implemented before, previous designs harvested less than 1% of monochromatic light due to their use of smooth (low surface area) semiconducting surfaces among other reasons.[38,39] Such low absorption could not be augmented by increasing the thickness of the dye layer. Instead, O'Regan et al. manufactured a low-cost device with a high surface area TiO_2 semiconductor film. This novel design harvested 46% of incident light with a light-to-electrical conversion above 7%. They noted that, by increasing the contact area between TiO_2 and the dye, the probability that an incident photon would be absorbed was significantly improved.

The semiconductor of choice, generally TiO_2, simultaneously takes on two responsibilities in a DSSC: i) passing/scattering sunlight through to the dye-sensitizer which harvests the light, and ii) conducting the electrons, transferred from the dye by photon absorption, to the electrode. To be efficient, the photons must be absorbed by the sensitizer for charge separation. Since the invention of the Gratzel cell, many researchers have examined methods for nanostructuring TiO_2 to maximize surface area while being careful not to increase the traps and diffusion path lengths for electrons.[31,32,34-37,40-43]

There are multiple known sources of electron loss and energy collection due (at least in part) to the semiconductor. Of these loss mechanisms, there is some loss when an

electron is injected into the semiconductor from the sensitizer. By matching the Fermi energy of the semiconductor closely with the lowest unoccupied molecular orbital (LUMO) energy of the sensitizer (the energy from which electrons in the sensitizer are transferred), one can minimize injection loss. For this reason, anatase TiO_2 (with a larger energy gap and a higher conduction band energy that better matches the LUMO level of the dye) is typically preferred in the DSSC over rutile TiO_2.[1] While other semiconducting metal oxides have larger bandgaps which could yield a greater photovoltage, their conduction band edges are higher than the LUMO level of common dyes. For example, Nb_2O_5 has a bandgap of ~3.8 eV, but a conduction band that is approximately 0.8 eV higher than that of anatase TiO_2. The LUMO energy level of N719 dye at an interface with anatase TiO_2 is approximately 0.3 eV larger than the conduction band edge for anatase. Therefore, a photosensitive dye such as N719 would need to be excited well above the LUMO (approximately 0.5 eV) for electron injection into the Nb_2O_5 conduction band).[44,45]

Electrons in the semiconductor can also be lost by back transfer into the electrolyte, by recombination with holes in the oxidized dye molecules, or by phonon relaxation within the semiconductor.[46] The crystallography and defect structure can affect the mobility of electrons within the semiconductor. If there are traps at the grain boundaries due to surface energy states or defects, then electron mobility could be limited.[46] Such factors as decreasing the number of grain boundaries an electron must pass through to reach the electrode can increase the mobility and decrease the probability of electron-electron hole recombination.[46] Furthermore, due to the significant loss mechanisms, it is imperative to ensure that the 3-D structure of the semiconductor allows the dye to absorb the maximum possible light by maximizing the contact area between the dye and the TiO_2.

For these reasons, DSSC devices with TiO_2 have been structured to increase efficiency by controlling light-scattering, repressing charge recombination, and modifying the semiconductor morphology to allow for maximum electron collection.[1,31,34,37,40,41,47,48] While many have focused their research on the variations in electron transport in TiO_2 due to crystallographic structure or doping, the 3-D nanostructure must also be considered before constructing a DSSC.[1,31,34,40,42,49-51] With the success of O'Regan and Gratzel in 1991, numerous groups have worked to generate and characterize different TiO_2 nanostructures, such as nanowires, nanotubes, nanorods, and nanopowders.[47,52-57] O'Regan's TiO_2 layer consisted of nanoparticles deposited as a porous film. By altering processing parameters of the mesoporous, anatase TiO_2, such as the precipitation pH, precursor chemistry, hydrolysis rate, and autoclaving pH, Barbe and Gratzel reached efficiencies near 10% by 1996.[36]

Several groups have continued to work with nanocrystalline porous TiO_2 films and have increased the surface area by increasing porosity and decreasing particle size.[37,50] However, it was quickly noted that a significant number of grain boundaries (with fine grain sizes) and the random network of nanoparticles (with highly porous films) increases the likelihood of electron trapping, diminishing the efficiency. Benkstein, *et al.* used percolation theory as "evidence that the network geometry strongly influences the electron transport dynamics in mesoporous nanoparticle TiO_2 films".[50] Modeling electron transport by random-walk through a simulated mesoporous TiO_2, they were able to show that as porosity increases, the diffusion path for electrons lengthens and found a corresponding decrease in efficiencies. Since then, researchers have been working to incorporate one dimensional nanostructures, such as nanotubes, to decrease the diffusion path length, as

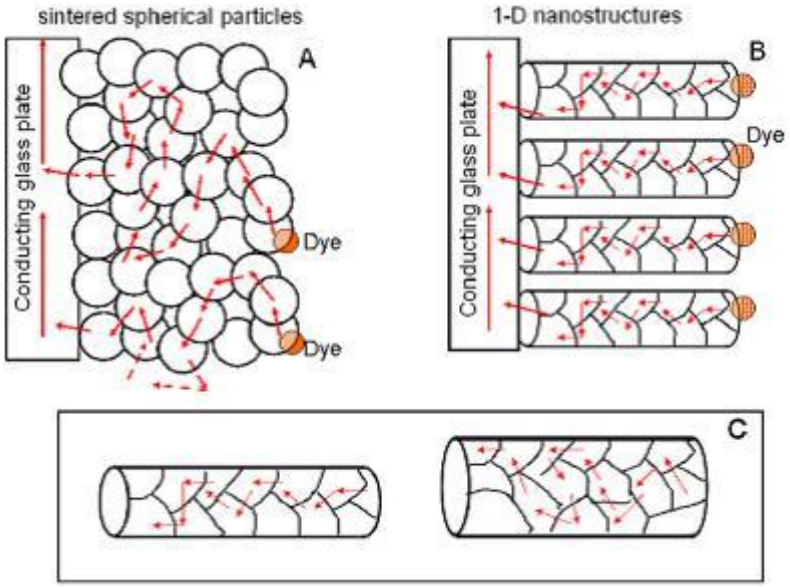

Figure 1.4. Schematic of electron diffusion through (A) nanoparticles, (B) 1-D nanostructures, and (C) 1-D nanostructures of differing diameters as shown by Jose, *et al*.[1] Reused with permission from John Wiley and Sons.

seen in Figure 1.4.

Previous researchers have synthesized aligned nanotubes, and fabrication of nanotube arrays with further tailored structures to enhance performance is still under investigation.[58] Anodization of aluminum has long been utilized to create self-ordered porous alumina with tunable pore sizes and thicknesses. There are several techniques for utilizing porous anodic aluminum oxide (AAO) as templates to create TiO_2 nanotubes, including surface sol-gel processing, protein-enabled layer-by-layer processing, and atomic layer deposition.[32,33,59] However, to date, while many researchers offer techniques for coating TiO_2 on alumina, there is no literature on methods for directly transforming Al_2O_3 into TiO_2.

Direct anodization of titanium to form TiO_2 nanotubes is also well reviewed and is capable of producing a wide range in tube pore sizes and array thicknesses encompassing

those included in this chapter.[60,61] However, Chapter 2 will introduce a new structure requiring the development of the reactive conversion method covered in Chapter 1. For this reason, the extent of control available for the reactive conversion of Al_2O_3 into TiO_2 is thoroughly studied here.

The proposed synthesis route using AAO allows for dimensional control (via control of both the initial AAO architecture and the reaction conditions), and substrate transferability. Aligned TiO_2 nanochannel arrays surrounding a soluble alumina template 10's of μm in length can be synthesized in as little as 30 min.

1.3 Experimental Procedures

The synthesis of aligned TiO_2 nanochannel arrays for the present work consists of the following steps: (i) synthesis of through-channel AAO templates; (ii) partial halide gas/solid displacement reaction of AAO to $TiOF_2$ using TiF_4 (see reaction equation 6); (iii) oxygenation and firing to form anatase TiO_2, and (iv) selective dissolution of remaining alumina and residual Al-bearing species in aqueous NaOH. The dissolution of residual Al-bearing species could result in porous TiO_2 nanochannel walls which would affect the surface area of the TiO_2.

$$3TiF_4(g) + Al_2O_3(s) \rightarrow 3TiOF_2(s) + 2AlF_3(s) \quad (6)$$

1.3.1 Syntheses of TH-AAO Templates

Through-hole anodic aluminum oxide (TH-AAO) templates were formed following galvanostatic anodization and controlled etching processes.[32] Variation in the diameters of the anodic pores was controlled by, and dependent on, the anodization solution, temperature, current density, and pore widening parameters chosen. Three anodization

conditions for AAO templates were explored for creation of TH-AAO and conversion to TiO_2. Table 1.1 identifies the pore diameters (average of 50 measurements on each of 3 AAOs of each type given with ± one standard deviation error ranges) synthesized in these experiments (see also the representative SE images in Figure 1.12). The anodization setup is illustrated in Figure 1.5.

Table 1.1. Anodization conditions and resulting average pore diameters.

Anodization Solution	Current & Temperature	Average Pore Diameter
1.515 M H_3PO_4	6 mA cm^{-2}, 4°C	284 ± 8 nm
0.5 M H_2SO_4	6 mA cm^{-2}, 10°C	55 ± 3 nm
0.3 M $H_2C_2O_4$	10 mA cm^{-2}, 15°C	90 ± 4 nm

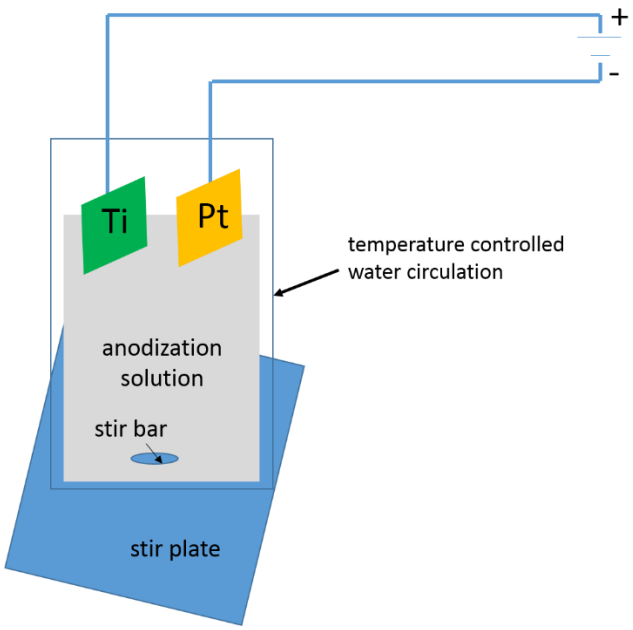

Figure 1.5. Schematic of setup for Ti anodization using a Pt counter electrode.

1.3.1.1 Synthesis of TH-AAO with Large Diameter Channels

High-purity aluminum sheets (99.999%, 1 mm thick, Goodfellow, Co., Oakdale, PA) were converted into AAO templates with aligned, one-end-closed pore channels on top of an Al backing, following the anodization procedure reported by Kang, *et al.*[32] In short, aluminum substrates were exposed to a series of electrochemical polishing steps followed by a two-step galvanostatic anodization in an aqueous solution of phosphoric acid (1.515 M, 6 mA/cm^2, and 4°C).

The aluminum backing and the alumina barrier layer formed during the anodization process must be removed to transform the porous alumina films into alumina membranes with open channels running entirely through the membrane thickness. As shown in Figure 1.6, to allow for selective removal of the underlying Al backing, the anodized Al_2O_3 surface was first coated with a thin nitrocellulose-based film (Double Duty nail polish, Sally Hansen, Morris Plains, NJ) using a brush and then allowed to dry for at least 2 h. The Al backing was gently ground mechanically to remove any minor buildup of Al_2O_3 on the back surface and along the sides. The Al backing was then selectively dissolved in an aqueous solution of 0.25 M copper (II) chloride dihydrate (Sigma-Aldrich, St. Louis, MO, USA) in 6.0 M HCl at room temperature for 20 min.[62] The removal of Al exposed the Al_2O_3 barrier layer located at the closed end of the pore channels. This exposed Al_2O_3 barrier layer was dissolved by immersion in 3 M NaOH for 18 min at room temperature, so as to open and widen the pore channels. The nitrocellulose-based mask that had coated and protected the Al_2O_3 membrane was removed by dissolution in 99.5% acetone at room temperature for 30 min. The resulting TH-PA-AAO (Through-Hole, Phosphoric Acid-derived, Anodic Aluminum Oxide) template was heated in air to 500 ºC for 1 h at a 10 ºC min^{-1} ramp to pyrolyze organics.

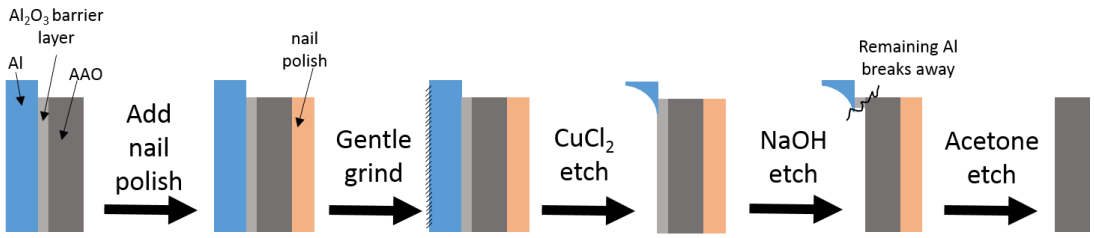

Figure 1.6. Schematic illustrating steps taken to form a TH-AAO after anodization.

1.3.1.2 Synthesis of TH-AAO with Smaller Diameter Channels

To create TH-AAO templates with smaller channel diameters, other anodization solutions can be used. Aqueous sulfuric acid anodization solutions have been show by Li, *et al*. to produce highly uniform channels with tunable lengths and with 60 nm interchannel spacing.[63] Using high purity (99.999%) aluminum, the substrates were cleaned and electropolished before anodization in 0.5 M aqueous sulfuric acid at 10°C and 6 mA/cm^2. Subsequently, the remaining aluminum was removed using the procedure outlined above and the channel bottoms were opened by chemical etching in gently stirred 5 wt% aqueous phosphoric acid at 30°C for 30 min. Aqueous oxalic acid solutions can also be used to generate anodic alumina templates with 20-100 nm channel diameters.[64] In such syntheses, high purity aluminum foil was cleaned and electropolished before anodization in 0.3 M aqueous oxalic acid solution at 10 mA/cm^2 and 15°C. After etching away the remaining aluminum backing, the channel bottoms were opened by chemical etching in gently stirred 5 wt% aqueous phosphoric acid solution at 25°C for 90 min.

1.3.2 Reactive Conversion of Al_2O_3 into TiO_2

TH-PA-AAO and TH-SA-AAO templates were converted into TiO_2 by the

following procedure. The TH-AAO was loosely wrapped with nickel foil (25.4 μm thick, McMaster-Carr, Atlanta, GA) as shown in Figure 1.7. It was then placed inside a titanium ampoule (outer diameter 2.5 cm, wall thickness 2 mm, length 20 cm; McMaster-Carr, Cleveland, OH, USA), containing a molar ratio of TiF_4 (Advance Research Chemicals, Catoosa, OK) to AAO between 5.7:1 and 7.3:1, which was subsequently sealed via welding within an inert argon atmosphere with an oxygen partial pressure <1 ppm. A schematic illustration of the reaction ampoule after loading is shown in Figure 1.8. The ampoule was heated in a horizontal tube furnace (surrounded by flowing argon (99.999%, Airgas, Radnor Township, PA) to the desired temperature (180°C – 335°C) at a rate of 5°C min^{-1} and held at that temperature for the desired length of time (0.5 h – 8 h) to allow for vaporization of the TiF_4 and reaction of TiF_4(g) with Al_2O_3. After cooling, the ampoule was removed from the furnace, cut open, and the specimens were extracted,

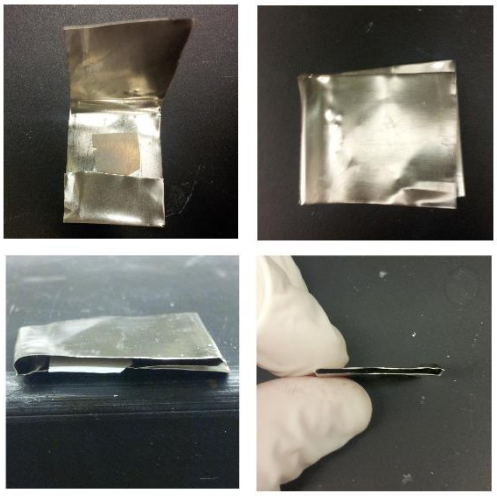

Figure 1.7. Images of nickel foil wrapped TH-AAO sample. Top left: TH-AAO sits on top of Nickel foil. Top right: top of nickel foil is gently folded over sample. Bottom left: TH-AAO has been moved to edge of nickel foil to show significant spacing for bulk TiF_4(g) to reach TH-AAO. Bottom right: cross section of nickel foil sandwiching is shown. TH-AAO cannot be seen.

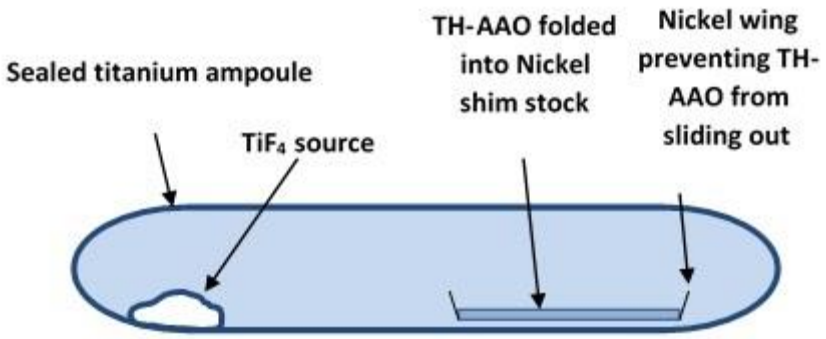

Figure 1.8. Schematic illustration of the sealed Ti ampoule in which the reaction of Al_2O_3 structures with TiF_4 was conducted.

resulting in a $TiOF_2$-bearing product layer on all surfaces of the TH-AAO. The ampoule was sufficiently gas-tight that residual TiF_4 was seen inside the ampoule upon sample extraction. The specimens were then oxygenated via reactions 7 and/or 8: a second heat treatment at 400°C for 4 h in pure, flowing oxygen that, before entering the furnace, was passed through a heated water bath (50°C) at a rate of 1 slpm. The measured humidity (using Model HMP234, Vaisala, Woburn, MA) at the gas outflow of the furnace was found to be at least 94% relative humidity. Finally, the specimens were fired in air to 650°C for 3 h to form the anatase TiO_2 polymorph.

$$TiOF_2(s) + H_2O(g) \rightarrow TiO_2(s) + 2HF(g) \quad (7)$$

$$2TiOF_2(s) + O_2(g) \rightarrow 2TiO_2(s) + 2F_2(g) \quad (8)$$

Afterwards, the specimens were mounted on glass slides using a thin nitrocellulose-based film (Double Duty nail polish, Sally Hansen) and etched in 3M NaOH for 1.5 h to selectively dissolve all remaining Al-bearing species, including any unreacted AAO and any Al-bearing byproducts. After rinsing, the glass-mounted specimens were then heated

in air to 500°C for 0.5 h to pyrolyze the nitrocellulose-based film resulting in free-standing, aligned TiO_2 nanotube membranes on glass. For transfer onto a working electrode, a 0.25" diameter circle of Scotch® tape was pressed onto an oversized section of the TiO_2 nanotube membranes and lifted off of the glass.

1.3.3 Photovoltaic Device Fabrication

DSSCs were prepared via a multi-step process beginning with preparation of the working electrode.[65] Fluorine-doped tin oxide (FTO) coated glass (2.54 cm x 1.27 cm x 2 mm thick, 13 Ω/□, Hartford Glass Company, Hartford City, IN) was cut into 0.5" x 1" x 2 mm pieces and cleaned via ultra-sonication for 20 min in a solution of 2.5 mg mL^{-1} detergent (Alconox Powder Detergent, VWR, West Chester, PA) dissolved in an aqueous solution of 50 vol% ethanol. After rinsing with deionized water and ethanol and drying for approximately 5 seconds under flowing nitrogen gas at room temperature, the FTO-coated side of the glass was partially masked with Kapton tape. The FTO glass was then submerged in an aqueous solution of 40 mM $TiCl_4$ (99% purity, Alfa Aesar, Ward Hill, MA) at 70 ºC for 0.5 h. After removing the Kapton mask (which allowed only the exposed FTO glass to interact with the $TiCl_4$ solution) and washing with water and ethanol, the treated FTO glass surface was partially masked by attaching a piece of Scotch® Magic™ tape (0.0625 mm thick) through which a 0.3125" diameter hole was punched. A TiO_2-bearing paste, composed of TiO_2 nanoparticles (20 nm average diameter, Ti-Nanoxide, T20/SP, Solaronix SA, Aubonne, Switzerland), was mixed in a 1:1 weight ratio with ethanol. After placing 10 μL of this mixture in and over the 0.3125" diameter hole in the tape, a doctor blade was wiped across the tape to remove excess TiO_2 paste located above the hole. The TiO_2 nanotube array adhered to Scotch® Magic™ tape (0.0625 mm thick)

was then placed on this layer of TiO_2 paste and the assembly was fired at 500 ºC for 1 h to pyrolyze the tape and to sinter-bond the array to the titania-coated FTO-bearing glass.

Afterwards, the electrode was exposed to a 0.2 M $TiCl_4$ (99 % purity, Alfa Aesar, Ward Hill, MA) solution at 70 ºC for 1 h, and then heated again to 500 ºC for 0.5 h. The $TiCl_4$ treatment improves film morphology by sealing the FTO from exposure to electrolyte while enhancing the surface area of TiO_2.[66] After an oxygen plasma treatment of the assembly for 10 min at 10.1 W (PDC-002, Harrick Plasma, Ithaca, NY), the working electrode was submerged in light-harvesting solution (0.3 mM t-butanol in a 1:1 volume ratio with acetonitrile) of N719 dye (cis-di(thiocyanato)-N-N'-bis(2,2'-bipyridyl-4-carboxylic acid-4'-tetrabutylammonium carboxylate) ruthenium (II), (Solaronix, Aubonne, Switzerland) for 24 h at room temperature.

A counter electrode was prepared by sandblasting a 1 mm diameter hole in an FTO-bearing glass slide, and then depositing an ethanolic solution of 2 mg mL^{-1} H_2PtCl_6 (99% purity, Alfa Aesar, Ward Hill, MA) on the FTO followed by firing at 450 ºC for 15 min. A 25 μm thick disk-shaped thermoplastic spacer (Meltronix 1170-25, Surlyn, Solaronix, Aubonne, Switzerland) was used to separate the working electrode (the titania nanotube-bearing FTO) from the counter electrode (the Pt-coated FTO). A 0.3125" diameter hole was cut into the spacer so that the titania nanotube array on the working electrode could be positioned within the hole. The redox electrolyte solution, which was composed of 0.6 M 1-butyl-3-methyl imidazolium iodide (99% purity, Sigma-Aldrich, St. Louis, MO, USA), 0.1 M guanidinium thiocynanate (≥97% purity, Sigma-Aldrich, St. Louis, MO, USA), 0.03 M I_2 (≥99.8% purity, Sigma-Aldrich, St. Louis, MO, USA) and 0.5 M tert-butylpyridine (96% purity, Sigma-Aldrich, St. Louis, MO, USA) dissolved in a mixture of 85 vol%

acetonitrile (99.8% purity, Sigma-Aldrich, St. Louis, MO, USA) and 15 vol% valeronitrile (99.5% purity, Sigma-Aldrich, St. Louis, MO, USA), was infiltrated under vacuum (using a roughing pump for approximately 30 seconds or until all visible air bubbles in the solution were removed) through the hole in the FTO-bearing glass of the counter electrode into the space between the counter and working electrodes and into the titania nanotube array. The hole in the counter electrode was then sealed using a 60 μm thick thermoplast film (Meltronix 1162-60, Solaronix SA, Aubonne, Switzerland) and a cover glass slide. A completed device is shown in Figure 1.9. A schematic of the device cross-section is shown in Figure 1.10 and a flowchart describing the entire process is shown in Figure 1.11.

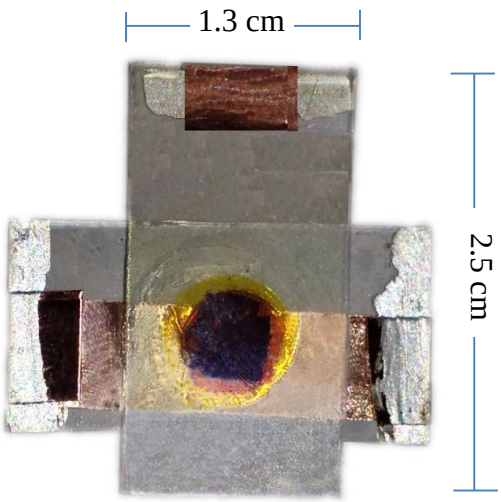

Figure 1.9. A completed titania nanotube-based DSSC with FTO glass that measured 1.3 cm by 2.5 cm.

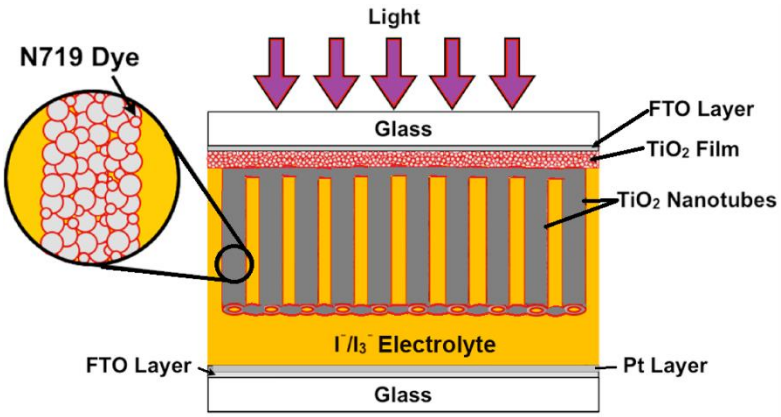

Figure 1.10. Schematic of the cross-section of a dye-sensitized solar cell containing interconnected TiO_2 nanotubes.

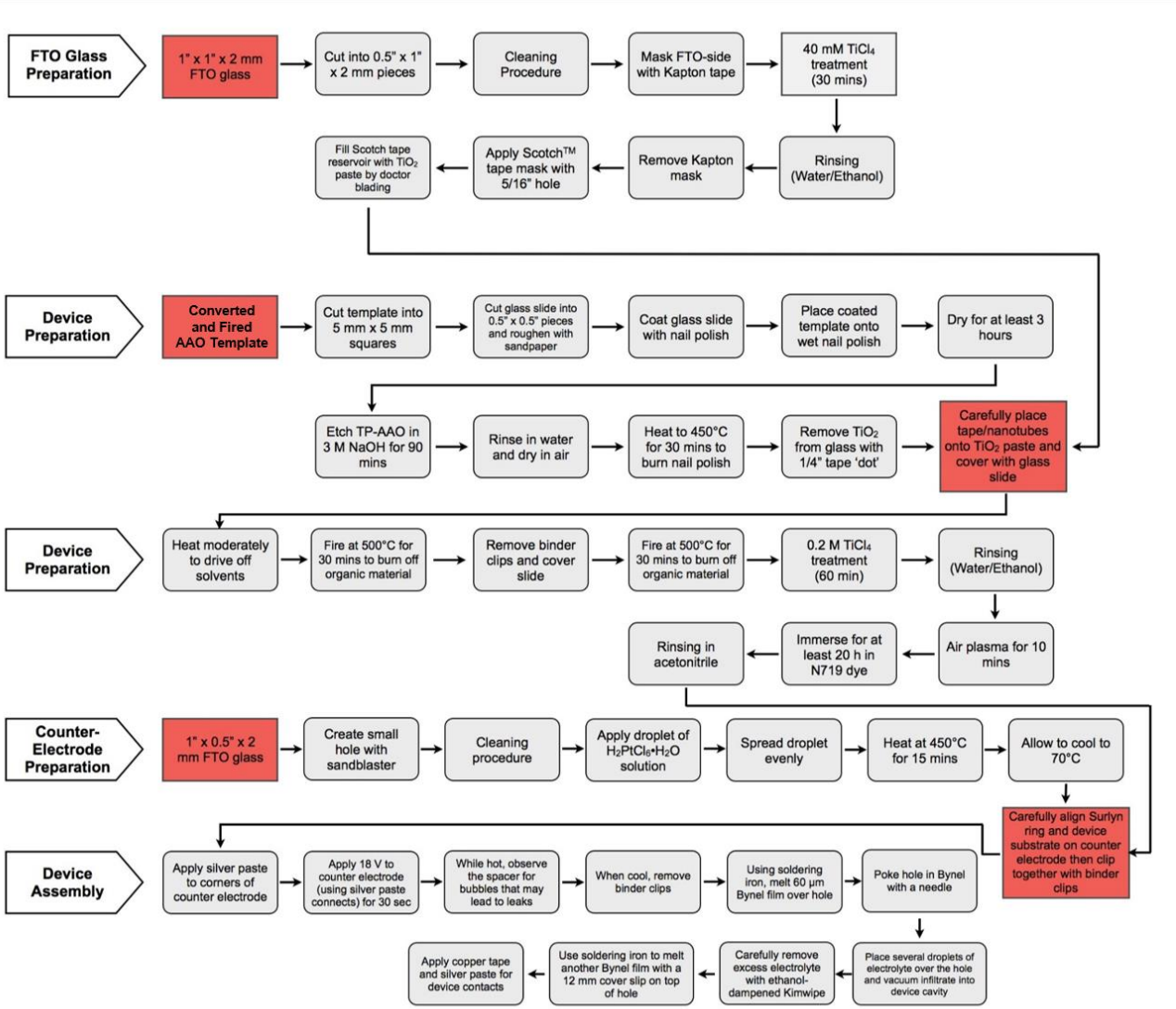

Figure 1.11. Flow Chart describing steps followed to prepare and assemble dye-sensitized solar cells for testing.

1.3.4 Characterization of the Nanotube Arrays and Cells

The micro/nanoscale morphologies of the TH-AAO templates and TiO_2 nanotube arrays were evaluated with scanning electron microscopy (1530 FEG SEM, LEO/Zeiss Electron Microscopy, Thornwood, NY or 1550 FEG SEM, LEO/Zeiss Electron Microscopy, Thornwood, NY) and transmission electron microscopy (JEOL 4000 EX, Japan Electron Optics Laboratory, Tachikawa, Tokyo or Technai F30 TEM, FEI, Hillsboro, OR, USA). Transmission electron microscopy was conducted by Dr. Ye Cai (Georgia Institute of Technology, Atlanta, GA, USA). Dimensional analyses were conducted using 10 measurements on 5 different imaged areas for 50 total measurements. The error range quoted for such measurements was the absolute range of values measured.

The crystal structures of the nanotube arrays were evaluated at room temperature via X-ray diffraction (XRD) analyses (Alpha-1, PANalytical Corp., Almelo, the Netherlands) on samples placed with the same side down as during conversion and via selected area electron diffraction analyses (JEOL 4000 EX) of cross-sections from the inside of the channels. XRD analyses were conducted using monochromatic $Cu_{K\alpha 1}$ (1.541 Å) radiation emanating from a 1.8 kW ceramic diffraction X-ray tube with a copper anode (45 kV, 40 mA) through a symmetrical Johannson monochromator. The incident beam optics were outfitted with 0.04 rad Soller slits, a 1º fixed anti-scatter slit, a ½º programmable divergence slit, and a 10 mm mask. The diffracted beam optics were outfitted with a 5.5 mm anti-scatter slit and 0.04 rad soller slits placed before the X'Celerator detector. Each pattern was produced with a summation of 12 identical 40 min scans conducted with Bragg-Brentano geometry and a step size of 0.01667º 2θ ranging from 20º to 70º 2θ. Current-voltage (*J-V*) measurements were conducted under airmass 1.5

global (AM 1.5G) conditions (Oriel 300 Watt solar simulator, 100 mW cm^{-2}) using an aperture with a measured area of 7.05 mm^2.

1.4 Results and Discussion

1.4.1 Anodic Al_2O_3 Templates

Two-step galvanostatic anodization processes were used to create anodic aluminum oxide TH-AAO with channel diameters dependent on the anodization conditions. The aluminum backing was then removed in a 6 M HCl, 0.25 M $CuCl_2$ solution. Subsequent immersion in 3 M NaOH or 5 wt% H_3PO_4 solution was used to remove the alumina barrier layer formed during anodization. Secondary electron images revealing the aligned pore channels in TH-AAO membranes are shown in Figure 1.12. The pore channels created in phosphoric acid (TH-PA-AAO membranes), as shown in Figure 1.12 (a) and (b), possessed an average diameter of 284 ± 8 nm and average height of 13.2 ± 0.2 μm after 2.5 h of anodization. In oxalic acid (TH-OA-AAO membranes), an average pore diameter of 90 ± 4 nm and average height of 11.7 ± 0.1 μm were obtained after 2.5 of anodization, as shown in Figure 1.12 (c) and (d). Anodization in sulfuric acid (TH-SA-AAO membranes) for 2 hours, yielded 55 ± 3 nm pore diameters and a 44 ± .4 μm average height, as shown in Figure 1.12 (e) and (f). However, these dimensions can be further tuned by varying the anodization and etching conditions. As generated, TH-AAO specimens scanned from the surface of the membranes were found to be amorphous by X-ray diffraction analyses as illustrated in Figure 1.13.

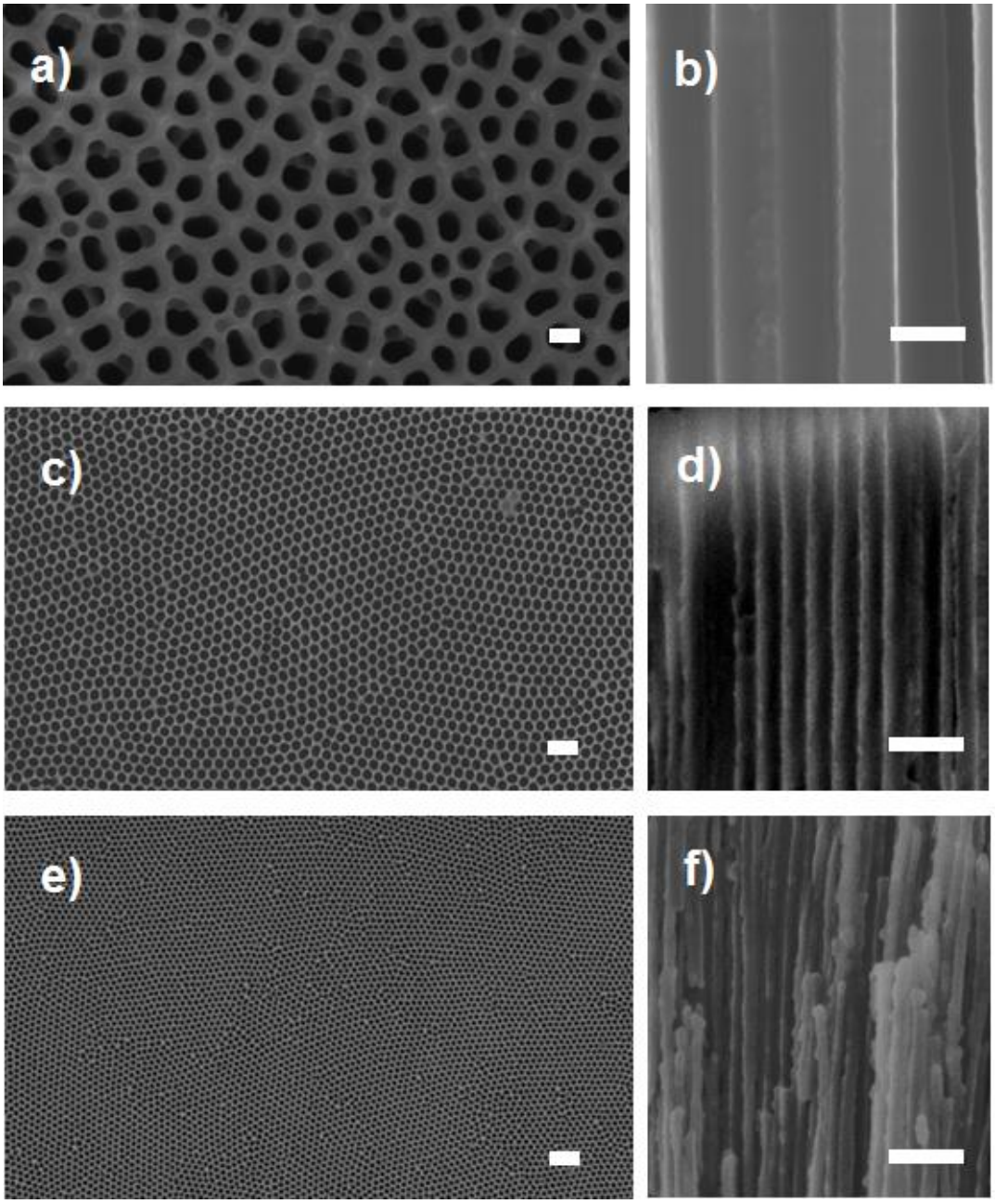

Figure 1.12. Secondary electron images of through-hole anodic aluminum oxide formed under different anodization solutions. TH-PA-AAO top (a) and cross-section (b). TH-OA-AAO top (c) and cross-section (d). TH-SA-AAO top (e) and cross-section (f). All scale bars are 200 nm.

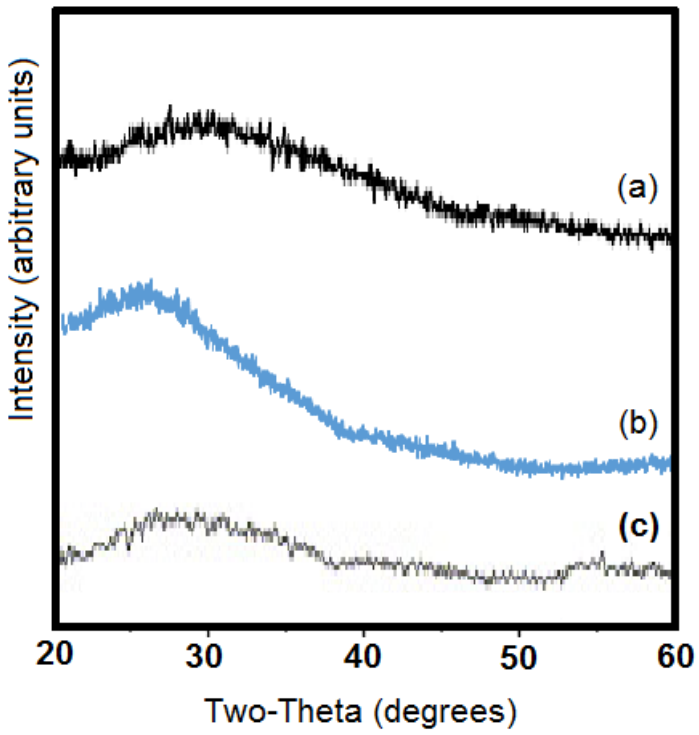

Figure 1.13. X-ray diffraction spectra of as-prepared (a) TH-PA-AAO, (b) TH-SA-AAO, and (c) TH-OA-AAO showing amorphous structures.

1.4.2 Reactive Conversion of TH-PA-AAO

A two-step metathetic gas/solid reactive conversion process was used to partially and controllably convert through-hole phosphoric-acid-derived anodic aluminum oxide (TH-PA-AAO) membranes into aligned nanotube arrays comprised of interconnected nanocrystalline TiO_2. The TH-PA-AAO was exposed to TiF_4 vapor in an otherwise inert (Ar) atmosphere and allowed to react for a set length of time, likely following one or more of the following reaction equations:

$$3TiF_4(g) + Al_2O_3(s) \rightarrow 3TiOF_2(s) + 2AlF_3(s) \quad (9)$$

$$TiF_4(g) + Al_2O_3(s) \rightarrow TiOF_2(s) + 2AlOF(s) \quad (10)$$

$$2TiF_4(g) + Al_2O_3(s) \rightarrow 2TiOF_2(s) + Al_2OF_4(s) \qquad (11)$$

In the above reactions, TiF_4 exists as a solid at room temperature and sublimes at 285°C and amorphous F-bearing Al products are water soluble.[67] Due to the possible glassy nature of aluminum fluorides and aluminum oxyfluorides (particularly in the presence of phosphorous), the chance of AlF_3 and Al_2O_3 reacting to form 3 AlOF as a secondary byproduct, and the imprecise measurability of weight changes of products and reactants, the exact reaction equation is unknown.[68,69] Attempts were made to fully convert Al_2O_3 nanopowder (Specific Surface Area (BET): >275 m^2/g, Strem Chemicals, Inc., Newburyport, MA) to track the weight change between reactant and products by reacting at 335 ºC for 24 h with powder bed depths less than 1 mm. The results of these experiments were unable to eliminate any potential byproducts because not all of the Al_2O_3 reacted (due to difficulty converting a measurably large mass in sufficiently thin layers to ensure gas penetration through all layers). Although there is no thermodynamic data available in the literature for solid $TiOF_2$, the formation of titanium oxyfluoride at ≥180°C from Al_2O_3 was apparently thermodynamically favorable, as indicated by TEM, SEM, and XRD analyses of the reacted samples, as will be shown later.

Early attempts to conduct a conversion at 350°C, in the manner described by Unocic, *et al.*[3], resulted in excessive grain growth of the $TiOF_2$ product on the top and bottom exposed surfaces, clogging the TH-PA-AAO channels before the reaction was able to create an interconnected product running along the complete length of the pore channels.

The growth of the $TiOF_2$ product layer was then controlled by lowering the reaction temperature to 335°C. By reacting at this temperature, while varying the time allowed for

reaction from 0.5 h to 8 h, the thickness of the product layer was controlled. Overall, the shapes of the nanochannels were preserved in the reacted samples. However, the smooth amorphous TH-PA-AAO surfaces transformed into rougher surfaces comprised of granular, interconnecting crystals. Figure 1.14, Figure 1.15, and Figure 1.16 illustrate the top (a), bottom (b), cross-section (c), and high magnification of the cross-section (d) of the TH-PA-AAO template for reaction times up to 8 h.

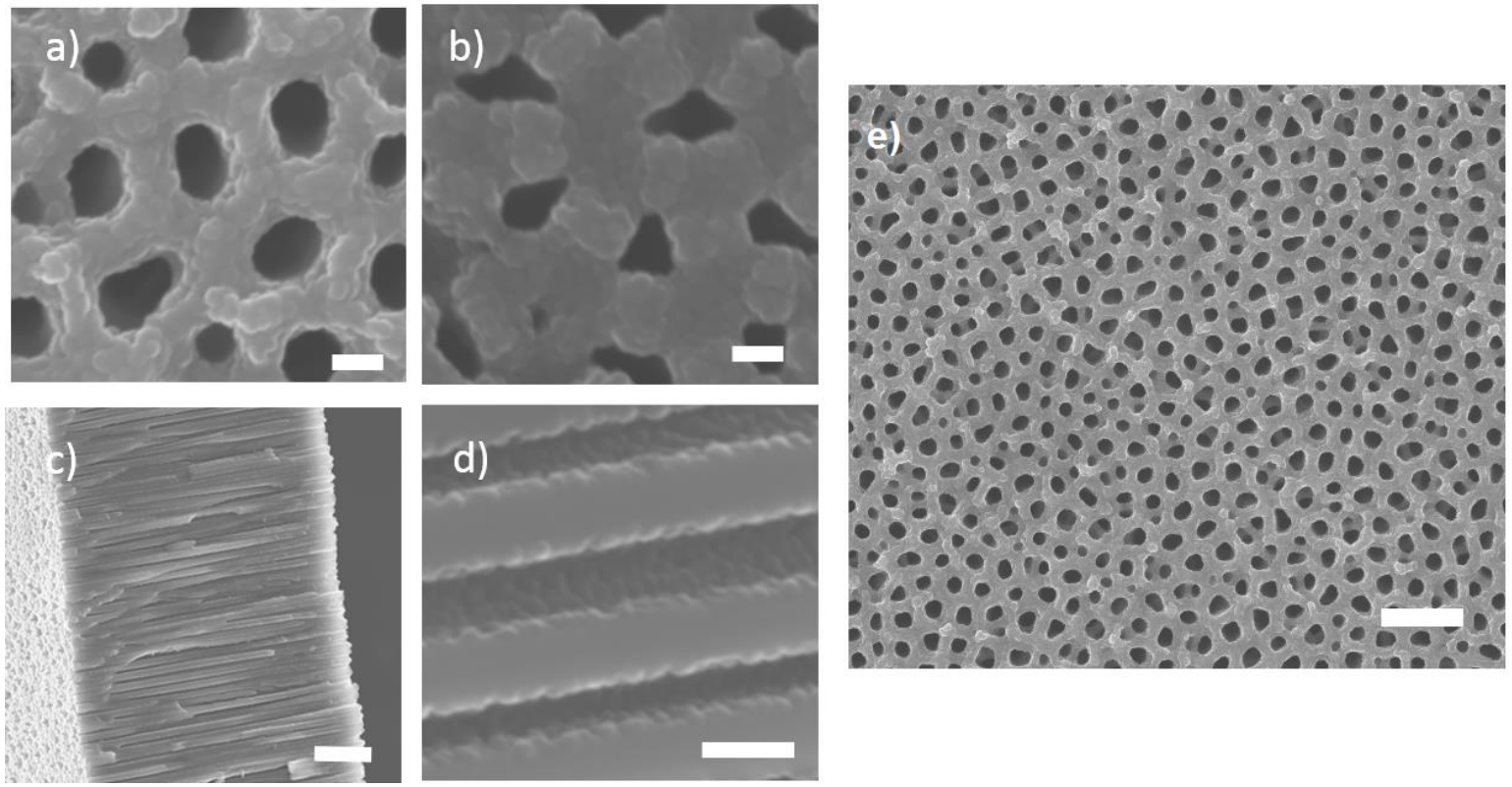

Figure 1.14. Secondary electron images of TH-PA-AAO after reaction with TiF_4(g) for 30 min at 335 °C viewed top-down at high magnification (a) and at low magnification (e), bottom-up at high magnification (b), and via cross-section at low magnification (c) and at high magnification (d). Scale bars for (a), (b), and (d) are 200 nm. The scale bar for (c) is 2 microns and for (e) is 1 micron.

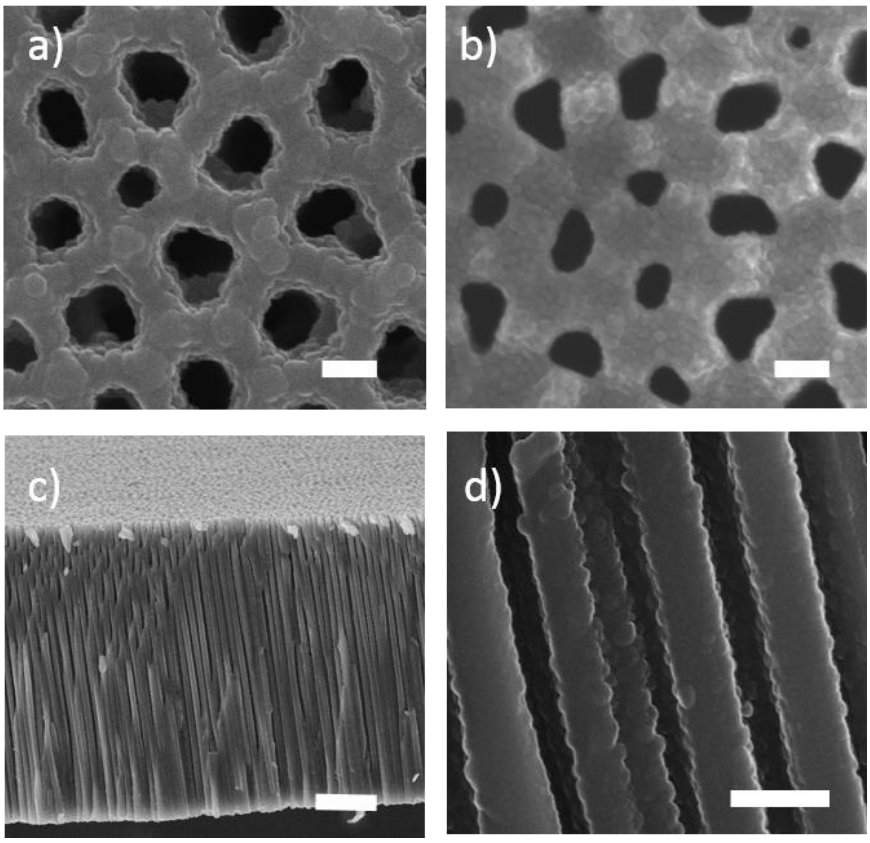

Figure 1.15. Secondary electron images of TH-PA-AAO after reaction with TiF_4(g) for 2 h at 335 °C viewed top-down (a), bottom-up (b), and via cross-section at low magnification(c) and at high magnification (d). Scale bars for (a), (b), and (d) are 200 nm. The scale bar for (c) is 2 microns.

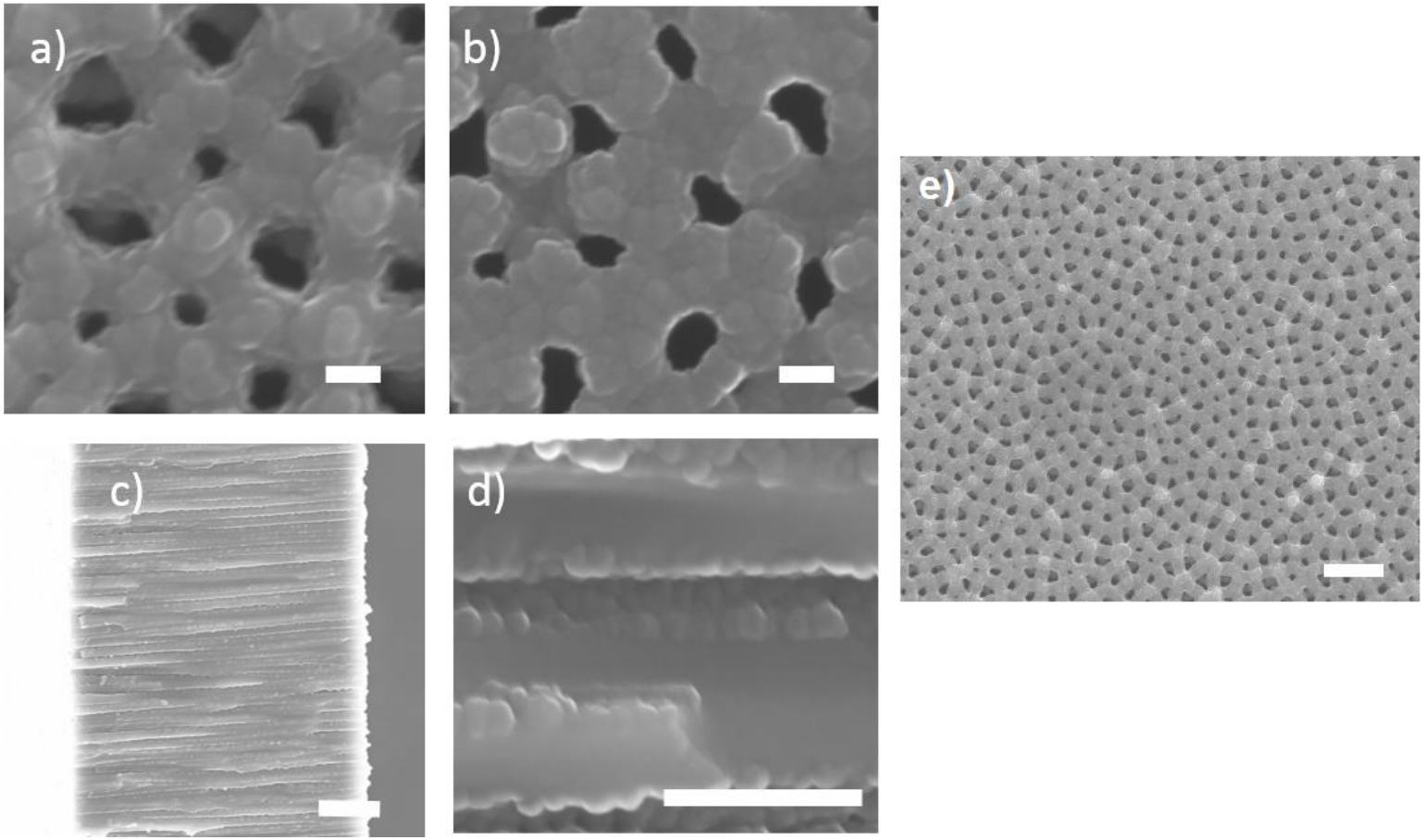

Figure 1.16. Secondary electron images of TH-PA-AAO after reaction with TiF_4(g) for 8 h at 335 °C viewed top-down at high magnification (a) and at low magnification (e), bottom-up at high magnification (b), and via cross-section at low magnification (c) and at high magnification (d). Scale bars for (a), (b), and (d) are 200 nm. The scale bar for (c) is 2 microns and for (e) is 1 micron.

By SEM, reaction was apparent within the first 0.5 h of reaction time. The reacted layer appears to coarsen and shrink the open diameter of the channels when reaction is allowed to occur for 8 h. The completion of reaction equations 9 and 10, forms, would result in volume expansions of 450% and 135% (powder diffraction files (PDF) 59-0871, 47-1659, 78-7622 and density of porous alumina as measured by Nielsch, *et al.,*[70] of 3.2 g/cm^2), respectively. Such significant volume increases apparently led to the decrease in average channel diameter from 284 nm ± 8 nm to 166 nm ± 45 nm after 8 h of reaction with TiF_4. The density of Al_2OF_4 was unknown, preventing calculation of an approximate volume change due to conversion to this material as shown in reaction equation 11. However, full conversion has not been realized on porous anodic alumina due to kinetic rate deceleration and closing of pores creating much longer diffusion pathways. Energy dispersive X-ray (EDX) spectroscopy provided information about the elemental makeup of each sample. As illustrated in Figure 1.17, before reaction TH-PA-AAO was comprised of aluminum, oxygen, and the dopant phosphorous, whereas after reaction for 0.5 – 8 h at 335°C, titanium and fluorine were also present.

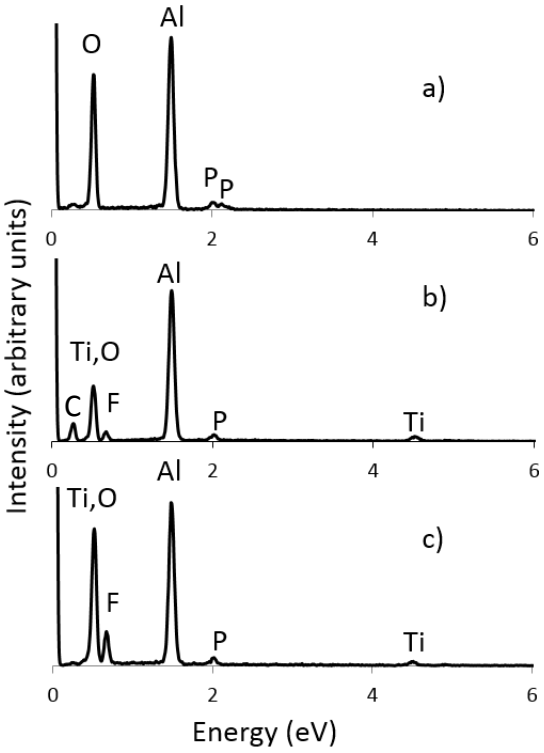

Figure 1.17. EDX spectra of TH-PA-AAO before reaction (a), after 30 minutes of reaction (b) and after 8 h of reaction at 335 °C (c) with TiF_4(g) reveals elemental composition of reaction specimens.

Upon examination by X-ray diffraction (XRD) analyses, the only crystalline material detected from top-down scans after reaction at 335°C from 0.5 – 8 h was $TiOF_2$ (see Figure 1.18) with a mean crystallite size of 9 ± 1 nm and 16 ± 1 nm by Scherrer analysis after 2 h and 8 h of reaction respectively. XRD data on the 0.5 h sample provided insufficient information (after >12 h of XRD scanning) for evaluation of the mean crystallite size of the sample. Transmission Electron (TE) microscopy reveals average product layer wall thicknesses of up to 45 ± 11 nm after 2 h and 57 ± 9 nm after 8 h at 335°C of reaction (see Figure 1.19).

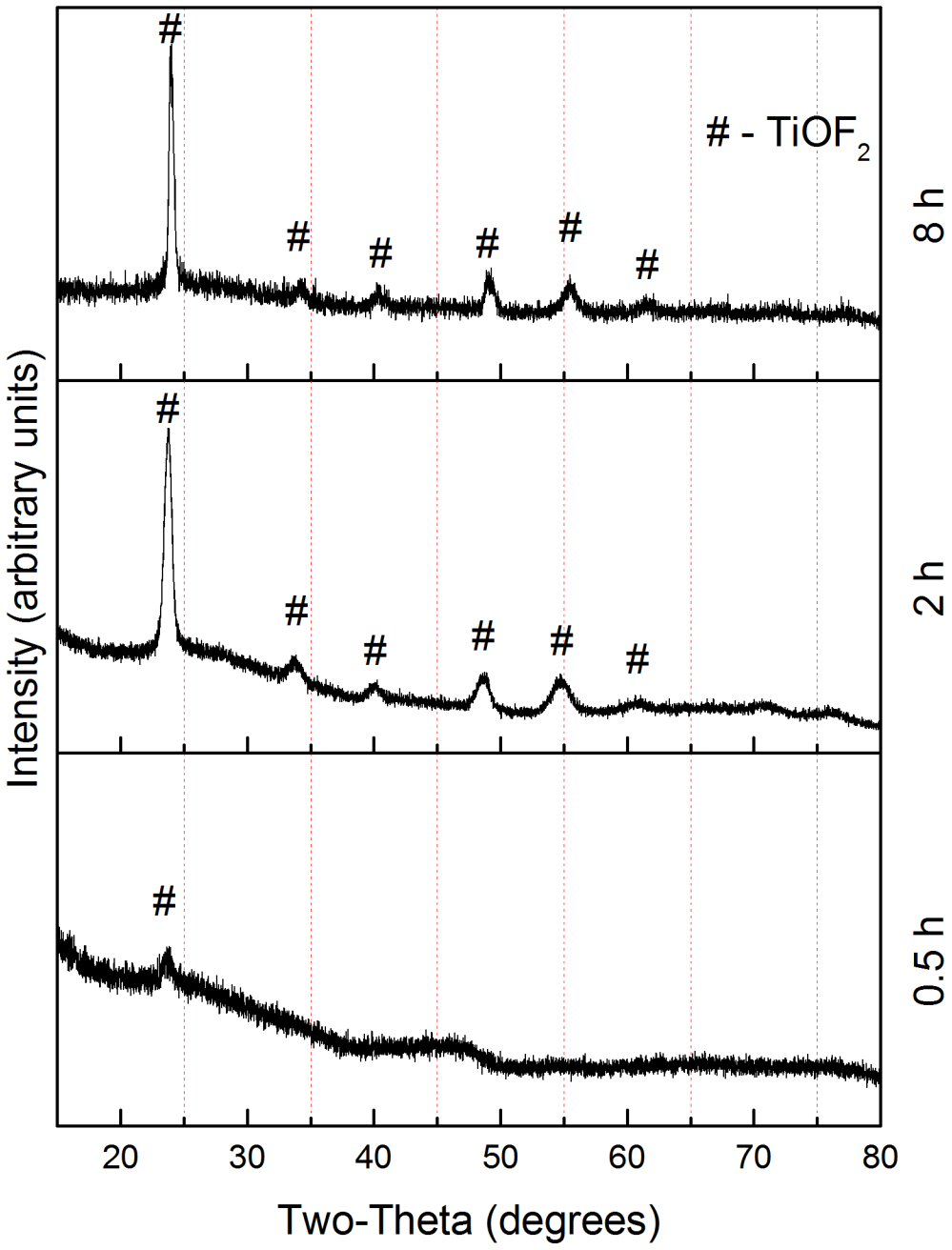

Figure 1.18. X-ray diffraction spectrum of TH-PA-AAO after reaction with TiF_4(g) at 335 °C for 0.5 h, 2 h, and 8 h showing on $TiOF_2$.

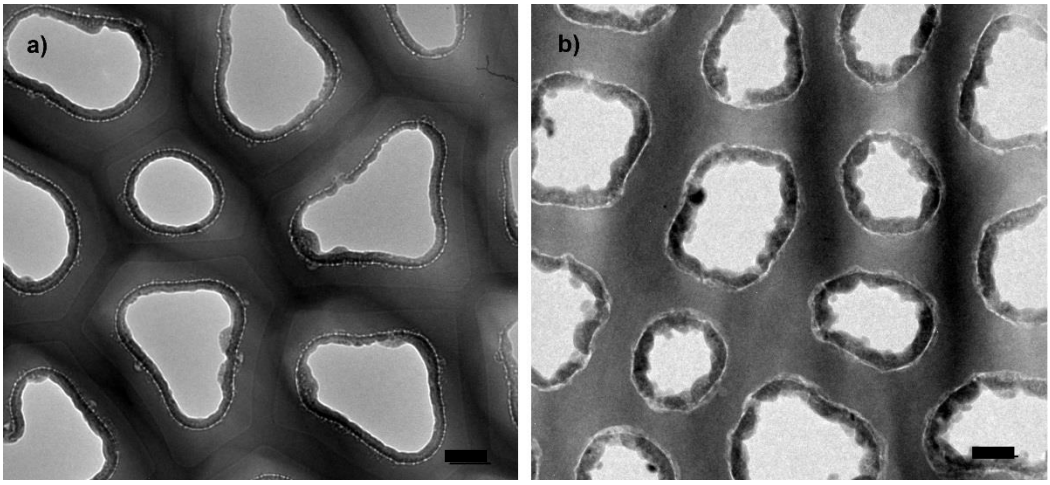

Figure 1.19. Transmission electron (TE) images near the middle of TH-PA-AAO membranes after reaction with TiF_4(g) at 335 °C for (a) 2 h and (b) 8 h. Scale bars are 100 nm.

Top-down and cross-sectional secondary electron (SE) images after TH-PA-AAO creation, after reaction with TiF_4 for 8 h at 335°C, after oxygenation of $TiOF_2$ at 400°C for 4 h and annealing of TiO_2 at 650°C for 3 h, and after etching of remaining Al-bearing species are shown in Figure 1.20 and Figure 1.21**.** Formation of a continuous TiO_2 layer can be observed after an initial reaction with TiF_4(g) for 2 h, while a shorter 0.5 h reaction time does not lead to continuity in the reaction layer (Figure 1.20).

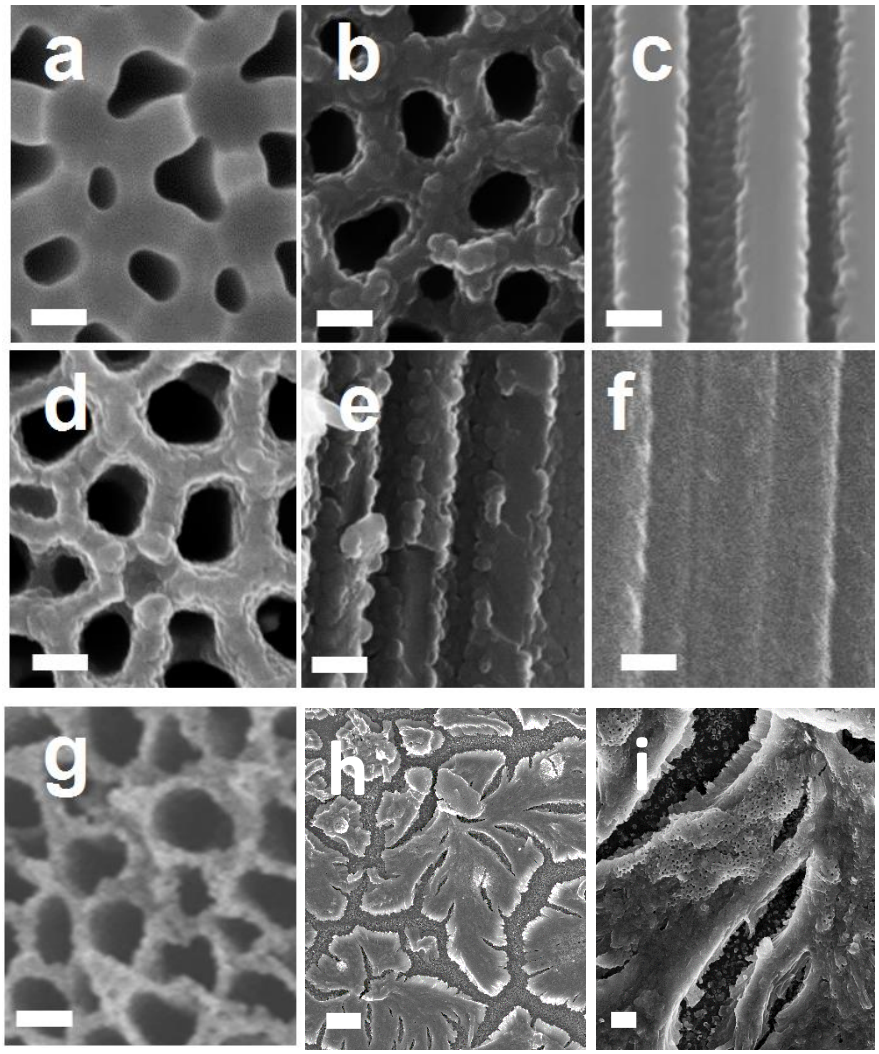

Figure 1.20. SE images of a) as-prepared AAO as viewed from the bottom side; b, c) AAO reacted with TiF_4(g) at 335 °C for 0.5 h viewed top-down and in cross-section, respectively; d, e) AAO reacted with TiF_4 at 335 °C for 8 h, oxygenated at 400 °C for 4 h, and fired at 650 °C for 3 h, viewed top-down and in cross-section, respectively; f) after etching a specimen reacted with TiF_4 at 335 ºC for 0.5 h, oxygenated at 400 °C for 4 h, and fired at 650 °C for 3 h viewed in cross-section; g)- i) after etching a specimen reacted with TiF_4 at 335 °C for 0.5 h, oxygenated at 400 °C for 4 h, and fired at 650 °C for 3 h viewed top-down showing some local pore retention (g) but overall collapse (h, i). The scale bars a) – g) correspond to 200 nm. The scale bar for h) corresponds to 10 μm and for i) corresponds to 2 μm.

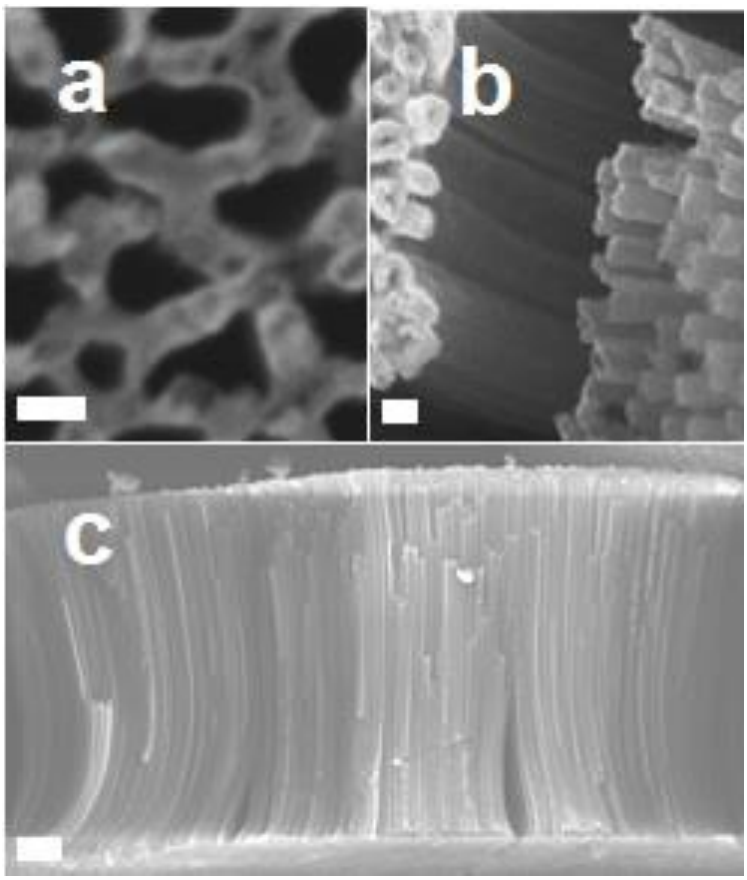

Figure 1.21. SE Images after reaction with TiF_4 at 335 ° C for 8 h, oxygenation at 400 ° C for 4 h, firing at 650 ° C for 3 h, and etching of PA-TH-AAO. Image (a) shows a top-down area, (b) shows a fractured set of tubes illustrating separation of the tubes away from the top or bottom of the channels and along the length of the channels, and (c) shows a cross section of a bundle. Scale bars are 200 nm for (a) and (b) and 1 μm in (c).

Reaction equations 7 and 8 each result in a 37% solid volume decrease upon conversion of $TiOF_2$ into TiO_2 (PDF 59-0871, 21-1272). Figure 1.20 illustrates the preservation of the $TiOF_2$ structure after oxygenation and firing to form TiO_2. After etching, the structure is still partially preserved (as seen in Figure 1.20 (g) and Figure 1.21) for all conversion times, however with only 30 minutes of reaction, etched samples often appeared collapsed (Figure 1.20(h)). X-ray diffraction and EDX confirm the presence of anatase TiO_2 and removal of F-bearing species, as shown in Figure 1.22. Figure 1.23 illustrates the presence of TiO_2 nanocrystals by high resolution transmission electron

(HRTE) microscopy and selected area electron diffraction (SAED). The nanotubes appear to be mostly dense with little porosity after etching likely due to the crystallization of γ-Al_2O_3 and subsequent difficultly etching this crystalline Al_2O_3 occurring within potential pore channels.

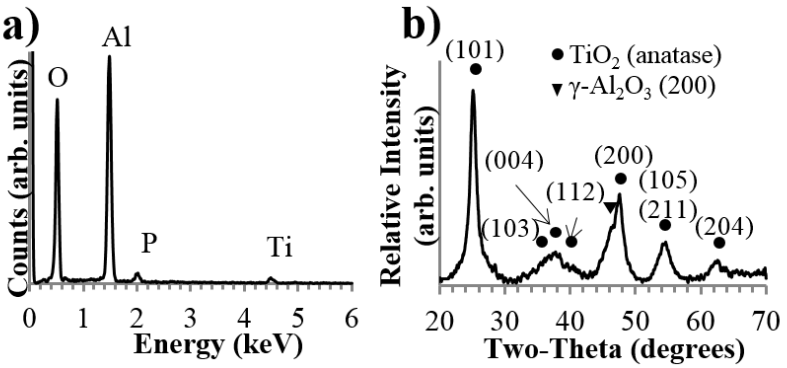

Figure 1.22. EDX (a) and XRD (b) after reaction with TiF_4 at 335°C for 8 h, oxygenation at 400°C for 4 h, firing at 650°C for 3 h, and etching of PA-TH-AAO for 1.5 h. The complete removal of fluorine is confirmed. By XRD, the primary crystalline structure observed is anatase TiO_2. Minimal amounts of γ-Al_2O_3 account for some remaining presence of aluminum, as no broad amorphous humps in the XRD spectrum were observed.

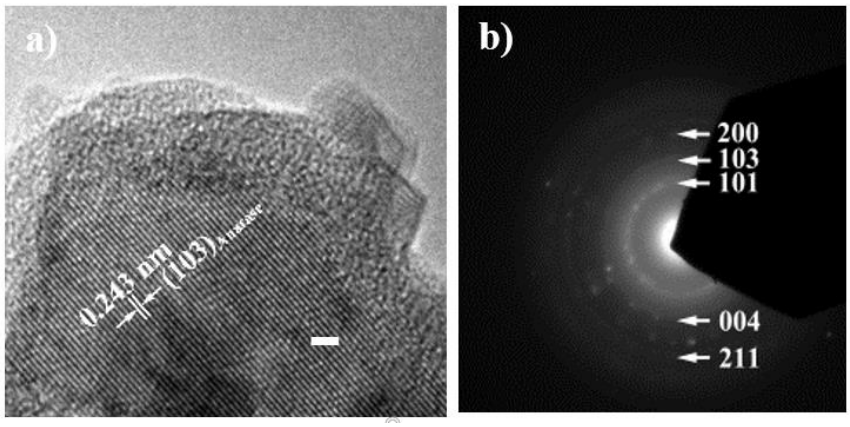

Figure 1.23. a) HRTE images of anatase nanocrystals in the reacted zone of the membrane after reaction with TiF_4 at 335°C for 8 h, oxygenation at 400°C for 4 h, firing at 650°C for 3 h. b) Corresponding SAED analysis revealing the presence of only the anatase polymorph within the reacted zone. Scale bar in a) corresponds to 2 nm.

1.4.3 Reactive Conversion of TH-OA-AAO

Attempts to convert through-hole oxalic acid anodic aluminum oxide into $TiOF_2$ and ultimately TiO_2 were successful after first firing the starting template in air at 1000°C for 2 h. This step allowed for the decomposition of aluminum oxalate (introduced during oxalic acid anodization) into Al_2O_3.[71] Conversions attempted at temperatures ranging from 180°C to 350°C without pre-firing the template resulted in no measureable formation of $TiOF_2$ within an 8 h time span (Figure 1.24). Pre-fired templates partially converted to TiO_2, as illustrated in Figure 1.25 and Figure 1.26, were then examined for solubility in 3 M NaOH. However, it was noted that such templates pre-fired at 1000°C contained crystalline Al_2O_3[72], which has poor solubility properties under most conditions (it is not acted upon by single acids and most known etchants work primarily as surface cleaning solutions. One known corundum etchant requires at molten flux at 1473°C).[73]

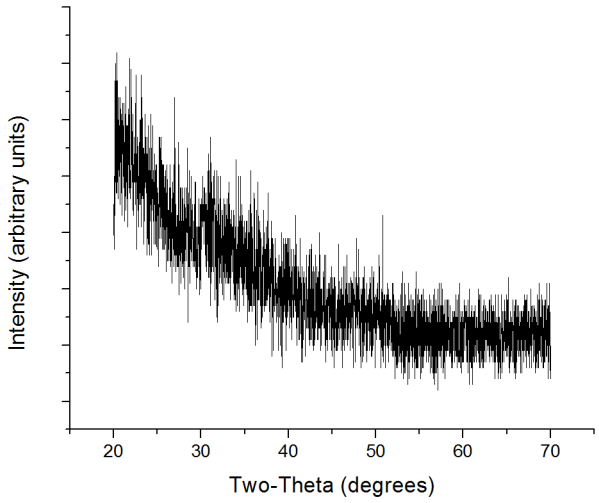

Figure 1.24. TH-OA-AAO after reaction with TiF_4 at 335 °C for 8 h shows no crystalline peaks via XRD.

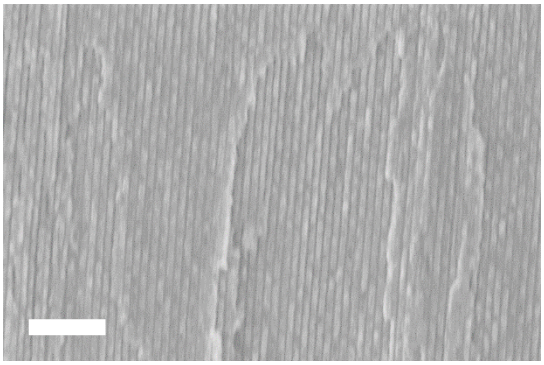

Figure 1.25. TH-OA-AAO after prefiring at 1000 °C for 2 h in air, reaction with TiF_4(g) at 335 °C for 0.5 h, oxygenation at 400 °C for 4 h, and firing in air at 650 °C for 3 h shows the channel structure maintained. Scale bar corresponds to 1 μm.

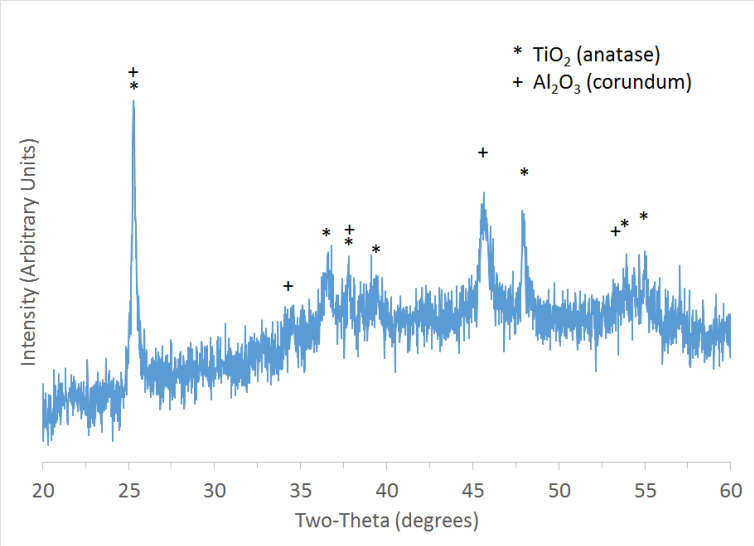

Figure 1.26. XRD of OA-TH-AAO after prefiring at 1000 °C for 2 h in air, reaction with TiF_4(g) at 335 °C for 0.5 h, oxygenation at 400 °C for 4 h, and firing in air at 650 °C for 3 h shows some crystalline Al_2O_3 among anatase peaks.

Such an inability to etch Al_2O_3 was thus expected to limit the ability to form free-standing TiO_2 nanotubes arrays derived from TH-OA-AAO templates. Nonetheless, pre-fired TH-OA-AAOs were exposed to TiF_4(g) at 335°C for 0.5 h (molar ratio of TiF_4 to

Al_2O_3 between 5.7:1 and 7.3:1) and converted to TiO_2 by oxygenation at 400°C for 4 h and firing in air at 650°C for 3 h as is shown by XRD in Figure 1.26. Thus, it is expected that the hypothesis that aluminum oxalate interfered with the intended reaction with TiF_4(g) was likely accurate although the reasoning behind oxalate interference is not fully understood. Other differences between the reaction with TH-PA-AAO and TH-OA-AAO include the larger pore channels and presence of phosphorous doping in TH-PA-AAO. Figure 1.26 illustrates the X-ray diffraction pattern of partially converted TH-OA-AAO showing anatase TiO_2 in addition to the presence of crystalline Al_2O_3 remaining from the pre-fire. Due to the inability to subsequently etch the remaining crystalline Al_2O_3 in 3 M NaOH (and thus, the poor applicability of such a structure to known applications), further optimization of the reaction with TH-OA-AAO was not explored.

1.4.4 Reactive Conversion of TH-SA-AAO

Similar to the reactive conversion of TH-PA-AAO, a two-step metathetic gas/solid reactive conversion process was used to controllably, partially convert through-hole sulfuric-acid-derived anodic aluminum oxide (TH-SA-AAO) membranes into aligned and nanotube arrays comprised of nanocrystalline TiO_2. The TH-SA-AAO was exposed to TiF_4 vapor in an otherwise inert (Ar) atmosphere and allowed to react for a set length of time. The formation of titanium oxyfluoride at ≥180°C from Al_2O_3 was apparently thermodynamically favorable, as indicated by TEM, SEM, and ED analyses of the reacted samples. Illustrated in Figure 1.27, after reactive conversion for 6 h at 180°C, pore channels appeared to remain open and $TiOF_2$ had formed. In Figure 1.27, Figure 1.28, Figure 1.29, after reactive conversion for 6 h at 180°C, oxygenation at 400°C for 4 h, and firing at 650°C for 3 h, anatase TiO_2 was formed and all fluorine was removed.

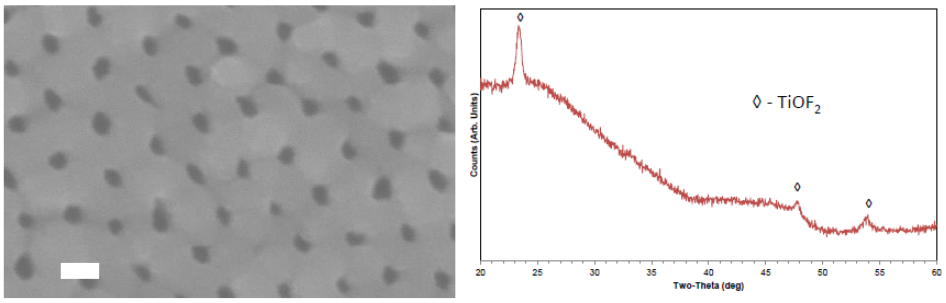

Figure 1.27. Top down SE image (left) and XRD spectrum (right) after reactive conversion at 180 ° for 6 h showing pores remaining open and formation of $TiOF_2$. Scale bar corresponds to 50 nm.

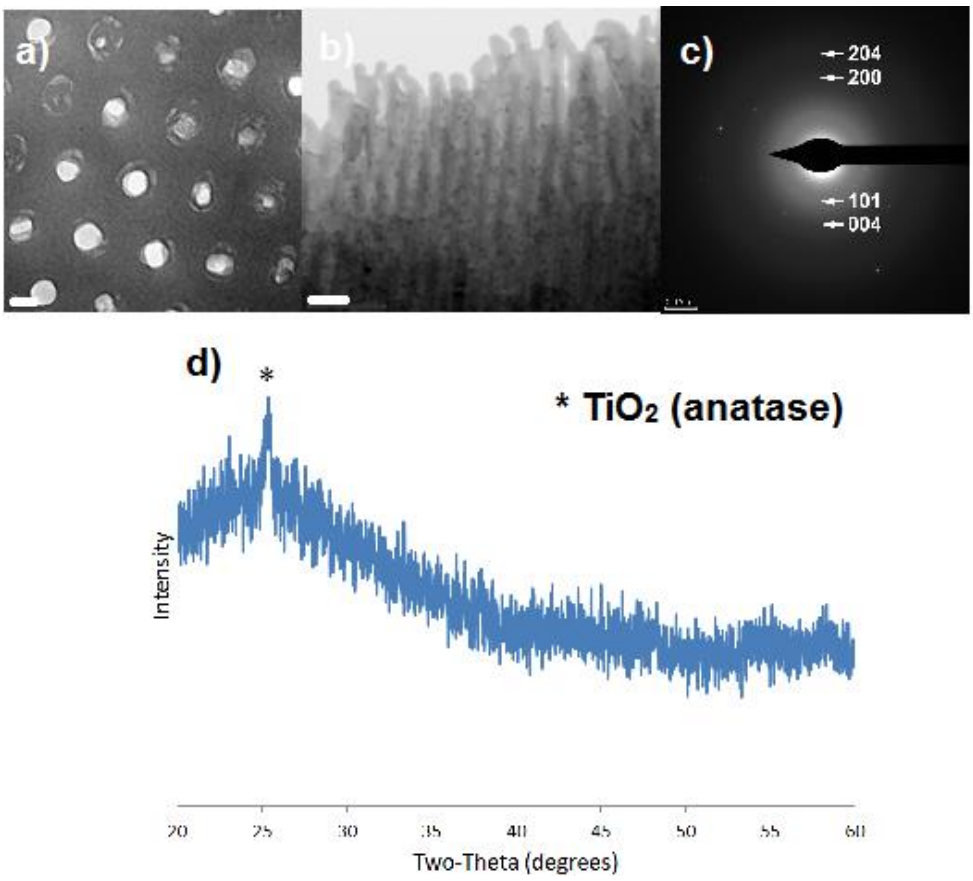

Figure 1.28. Top down (a), cross-sectional (b) TE images, ED pattern (c), and XRD pattern (d) reveal anatase amidst the amorphous anodic alumina after reactive conversion at 180 °C for 6 h, oxygenation at 400 °C for 4 h, and firing at 650 °C for 3 h. ED pattern taken from cross-sectional TE image. Scale bars are 20 nm for (a) and 100 nm for (b).

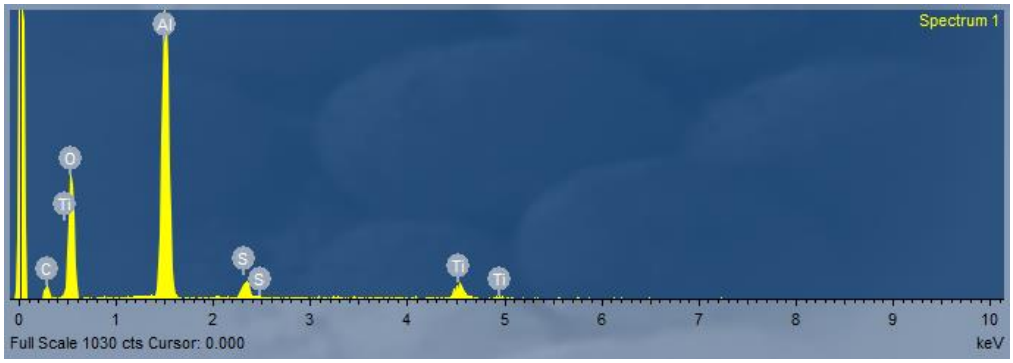

Figure 1.29. EDX spectrum at center of channels shows that TiO_2 is present in throughout the thickness of the converted, oxygenated, and fired SA-AAO sample.

In the semiconducting layer desired for electrode applications, the anatase must be interconnected throughout each channel, in order to form free standing nanotube arrays or direct pathways for electrons to travel through TiO_2 from one end of a nanotube to the other. While anatase had formed throughout the channels of the anodic alumina, crystallites appeared disperse, with little connectivity along the smooth channels of the anodic alumina, as can be seen in Figure 1.31. Subsequent mounting on a glass slide and etching in 3 M NaOH resulted in tube bundling and collapse as shown in Figure 1.30. In this figure, all images are taken top-down, and pore channels appear to be closed. Evidence of TiO_2 having taken the shape of the porous anodic alumina is seen in the lower images of this figure, where a section of TiO_2 appears on its side showing lengthwise a section of what could be nanochannels.

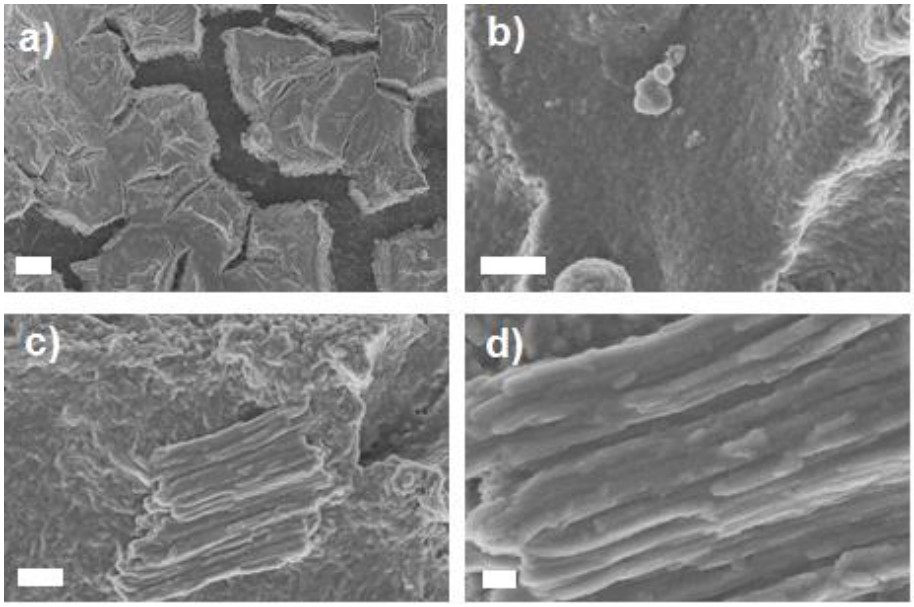

Figure 1.30. Top-down SE images of SA-AAO after reactive conversion at 180 °C for 6 h, oxygenation at 400 °C for 4 h, firing at 650 °C for 3 h, mounting on a glass slide, and etching in 3 M NaOH. Scale bars are 10 microns (a), 1 micron (b), (c), and 200 nm (d).

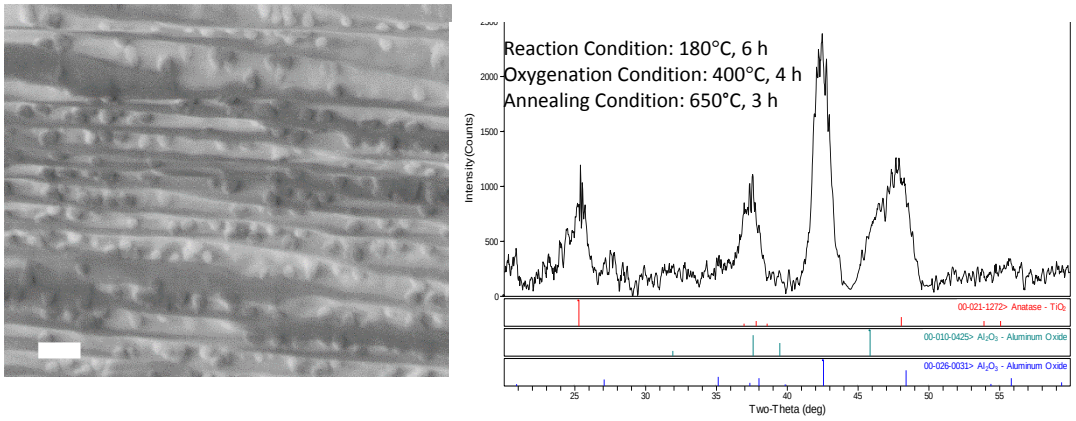

Figure 1.31. Cross-sectional SE image (right) after conversion, oxygenation, and firing shows particles present in the pore channels. XRD (right) shows anatase TiO_2 in addition to some crystalline Al_2O_3. Scale bar corresponds to 100 nm.

Increasing the reaction temperature with TiF_4 to 300°C and reacting for a 30 min appeared capable of retaining open pores, as shown in Figure 1.32. Upon oxygenation at 400°C for 4 h, firing at 650°C for 3 h, these samples were etched in 3 M NaOH for 1.5 h, and while remaining bundles were more present, the tops were overreacted and sealed

closed after etching (also shown in Figure 1.32). Going beyond this temperature and time, however, consistently resulted in excessive reaction of the surface of the starting templates which closed the pore channels.

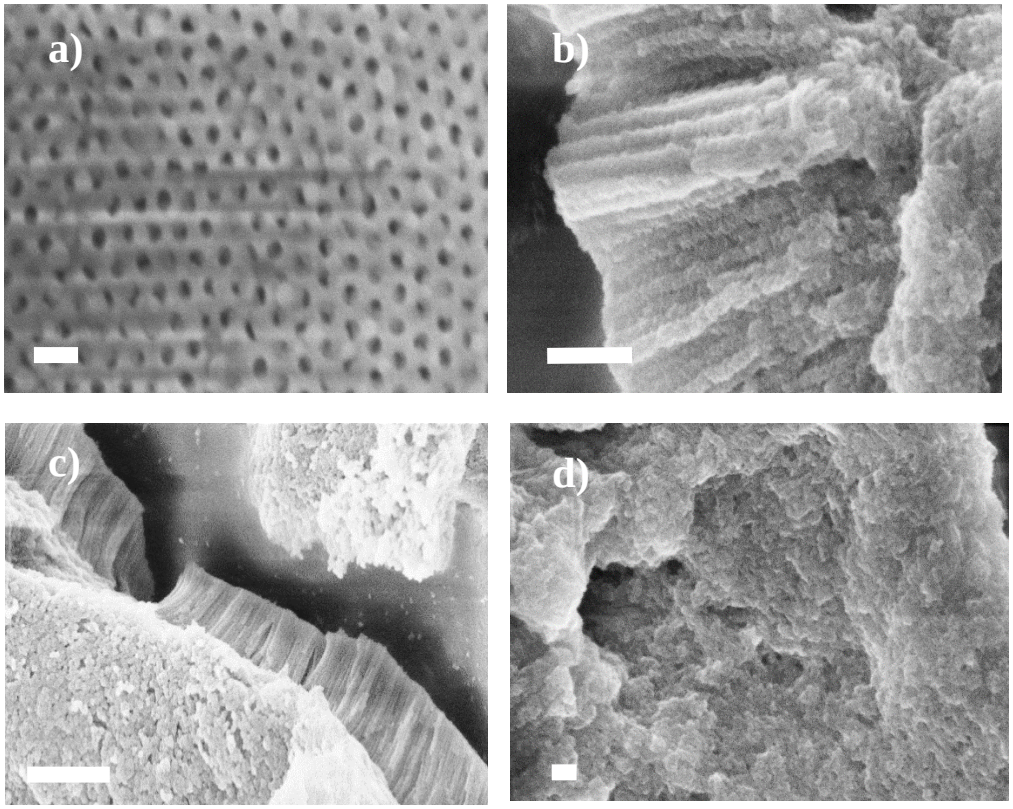

Figure 1.32. Top-down SE image of SA-AAO after reactive conversion with TiF_4(g) at 300 °C for 30 min (a) reveals most channels not fully sealed at the surface. Top-down SE images (b-d) after being oxygenated at 400 °C for 4 h, fired at 650 °C for 3 h and etched in 3 M NaOH for 1.5 h, the same sample reveal more apparent nanotube channels, however the interconnectivity near the bundle surface, as best illustrated in (d), shows minimal porosity. Scale bars correspond to 100 nm in (a) and (d), 200 nm in (b), and 1 μm in (c).

1.4.5 Dye Sensitized Solar Cell Testing

Experiments were conducted to measure the DSSC behavior of the TH-PA-AAO specimens reacted at with TiF_4(g) 335°C for 8 h, oxygenated at 400°C for 4 h, fired at 650°C for 3 h. Three working electrodes were fabricated following a procedure described

previously (see Figure 1.33). The current-voltage behavior of the best performing device resulted in 4.7 % efficiency. The three devices exhibited an average open-circuit voltage of 726 ± 82 mV, an average fill factor of 0.758 ± 0.10, and an average efficiency of 4.4 ± 0.3 %. The current-voltage behavior of the DSSCs in available in Table 1.2.

Table 1.2. Average current voltage behavior across three devices.

Device Parameter	Average Value (3 Devices)
V_{OC}	726 ± 82 mV
J_{SC}	8.0 ± 1.1 mA cm^{-2}
Fill Factor	0.758 ± 0.10
Efficiency	4.37 ± 0.33 %

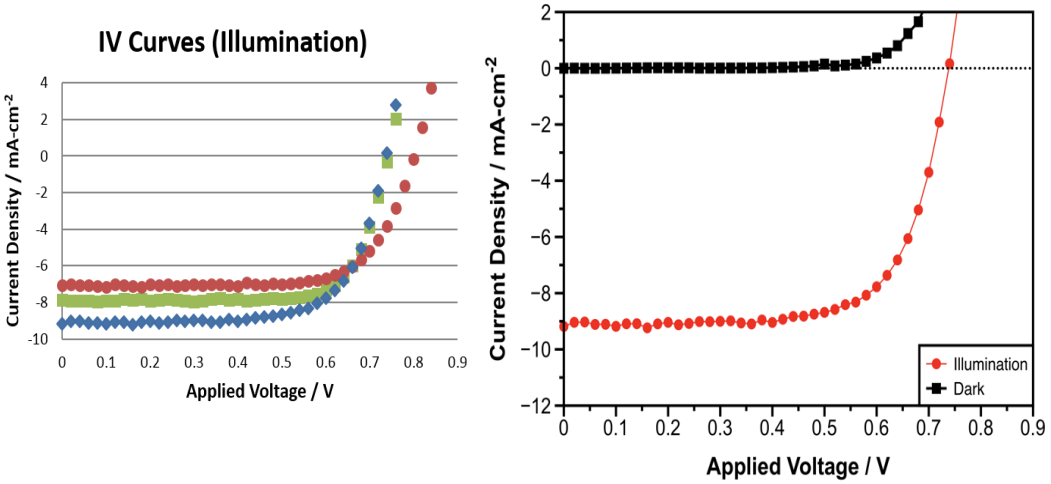

Figure 1.33. Current-voltage behavior during illumination of all devices (left) and of the best-performing device (4.7% efficiency) in the dark and under AM 1.5G illumination (right).

1.5 Conclusions

A gas/solid reaction of Al_2O_3 was used to generate anatase TiO_2 nanochanneled electrodes via a $TiOF_2$ intermediate product. Such reaction showed control over nanotube

wall thickness when a phosphoric-acid derived anodic alumina template was used. Working electrodes containing anatase nanotube arrays were constructed into DSSC devices exhibiting an average efficiency of 4.4%. Attempts to react anodic alumina with smaller pore channel diameters (i.e. sulfuric-acid derived and oxalic-acid derived anodic alumina templates) were proven capable of forming TiO_2 throughout channels that are impenetrable to liquid-based depositions under known conditions (i.e. in house tests of infiltrating these smaller pores with protamine-bearing and titania precursor-bearing Ti(IV) bis-ammonium-lacto-dihydroxide using the method reported in Berrigan, *et al.*[33] were unsuccessful). However, free-standing, small-diameter nanotube arrays with open channel tops were unable to be formed because the surrounding Al_2O_3 was insoluble (i.e. reactions that started with TH-OA-AAO templates) or possibly because the anatase crystallite size was relatively large compared to the channel diameters and the high aspect ratio of the expected nanotube arrays resulted in collapse of the tubes after etching (i.e. reactions that started with TH-SA-AAO templates).

Nonetheless, the next chapter extends the work with this reactive conversion method by combining the TH-PA-AAO reaction with a wet-chemical deposition method to form multi-wall TiO_2 nanotube arrays for solar cells with enhanced efficiencies. Such multi-wall TiO_2 nanotube arrays have not been realized via other methodologies making the usefulness of the reactive conversion method more clear. Not via direct anodization of Ti to for TiO_2 nanotube arrays nor by purely wet chemical techniques have multi-wall TiO_2 nanotube arrays been created.

CHAPTER 2 A HYBRID SOL-GEL/GAS-SOLID DISPLACEMENT METHOD FOR ALIGNED MULTI-WALLED TITANIA NANOTUBE ARRAYS

2.1 Introduction

High-aspect-ratio, single-wall TiO_2 nanotube arrays, as demonstrated in the previous chapter, be used as electrodes, such as for dye-sensitized solar cells (DSSCs). Their 1-D open channels minimize electron diffusion pathways, and their high surface areas allow for high levels of dye (or other molecule) adsorption. However, a common problem with single-wall nanotube arrays is their likelihood to agglomerate upon drying, due to capillary stresses.[32,33,74-76] Such bundling can degrade the alignment and structural uniformity of the arrays and result in increased electron diffusion pathways (and thus the likelihood of electrons recombining and being lost) through the nanotube arrays.[76]

In this chapter, we present a method for producing agglomeration-resistant, well-aligned, high-aspect-ratio titania nanochannel arrays from anodic aluminum oxide (AAO). The resulting structures, produced by a combination of conformal coating and gas/solid reaction techniques, consist of rigid multi-wall titania nanotube (MWTNT) arrays. The dye-loading capacities and power conversion efficiencies of DSSCs containing MWTNT-based electrodes are compared to single-wall titania nanotube (SWTNT) array electrodes created by conformal coating alone. Much of the material in this chapter has been published in *Berrigan, et al.*[2]

2.2 Experimental Methods

The conversion of AAO templates into MWTNT arrays (Figure 2.1a) for electrode applications was conducted by the following series of steps: deposition of a conformal TiO_2 coating onto the surface of the AAO template nanochannels via a wet chemical process (i.e., sol gel coating) (Figure 2.1b); partial etching of the AAO and the removal of the Al substrate to open the channels of the AAO template (to yield flow-through AAO membranes as opposed to one end closed membranes) (Figure 2.1c); partial reactive conversion of the remaining AAO into titanium oxyfluoride ($TiOF_2$) (Figure 2.1d); oxygenation of $TiOF_2$ into TiO_2 (Figure 2.1e); and selective dissolution of aluminum-bearing phases to yield freestanding, aligned, MWTNT arrays (Figure 2.1f).

Porous amorphous anodic alumina (AAO) templates were generated as described in the previous chapter's section 1.3.1. In short, high-purity aluminum sheets were anodized twice in a phosphoric acid-bearing solution with an anodization time (the time allotted for pore channel formation) of 2.5 h at 4°C using a current density of 6 mA cm^{-2}.[32,33] The templates were vacuum infiltrated with a titanium(IV) isopropoxide (97+% purity, Alfa Aesar, Ward Hill, MA, USA) solution (3:1 wt. ratio, in anhydrous isopropanol) and allowed to hydrolyze overnight in air (40% relative humidity).[32] Excess TiO_2 formed on the AAO external surfaces during this process was removed using adhesive tape gently and evenly pressed onto the substrate with a piece of glass before being peeled away. The adhesive tape residue was removed by 30 min incubation in dichloromethane (99.9% purity, VWR, Radnor, PA, USA) under vigorous stirring on a magnetic stir plate. The infiltration process was then repeated a second time.

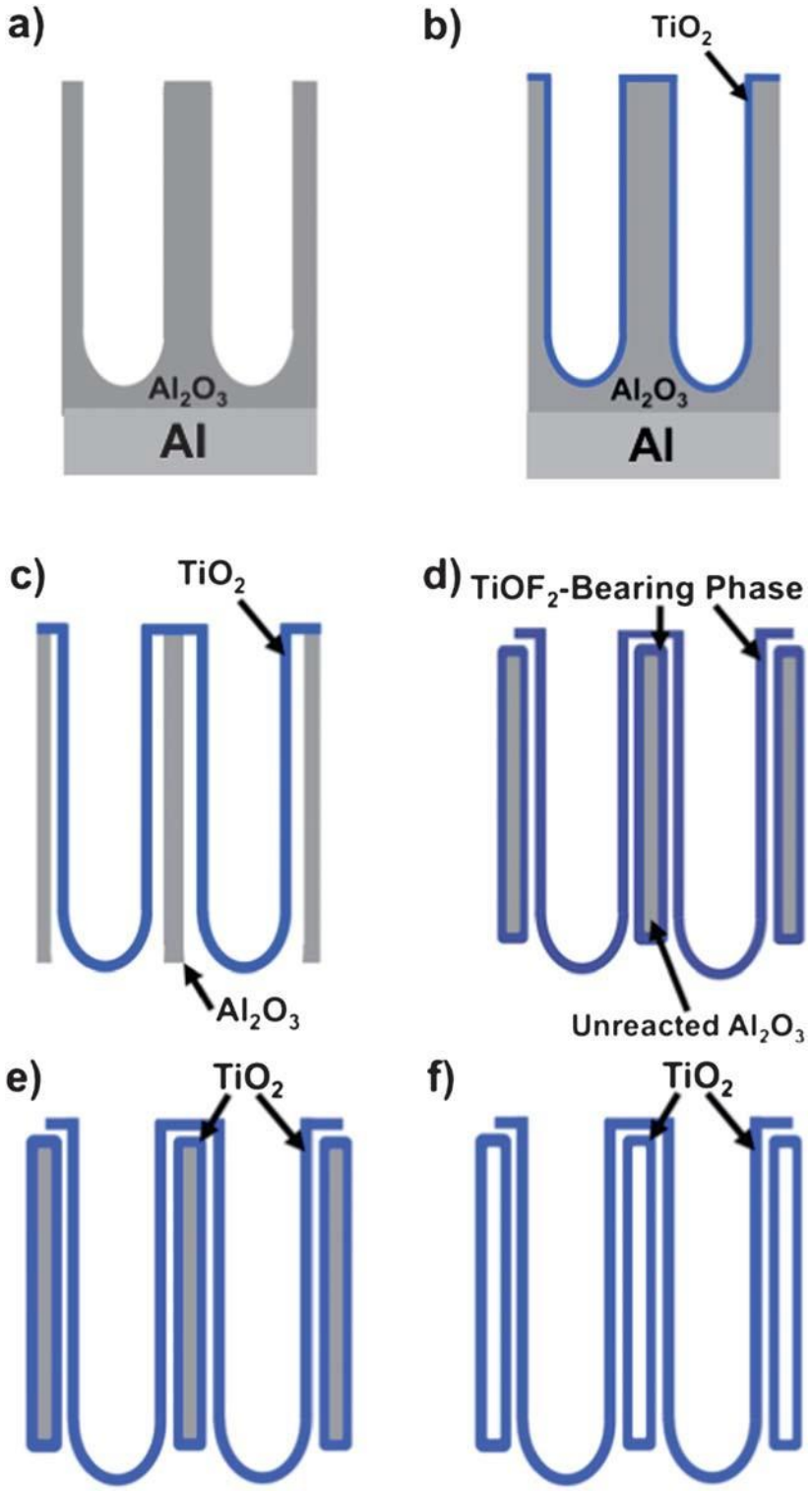

Figure 2.1. Schematic illustration of the hybrid coating and reaction process used to convert AAO templates into freestanding, aligned MWTNT arrays. Berrigan, *et al*.[2] Reproduced by permission of The Royal Society of Chemistry.

The TiO_2-infiltrated alumina was coated with a thin nitrocellulose-based film (Double Duty nail polish, Sally Hansen, Morris Plains, NJ) using a brush and allowed to dry at room temperature for at least 2 h. This film masked the alumina and allowed for selective removal of the underlying Al backing by wet chemical etching in an aqueous solution of 0.25 M copper (II) chloride dihydrate (98% purity, Alfa Aesar, Ward Hill, MA, USA) in 6.0 M HCl (VWR, Radnor, PA, USA) at room temperature for ~20 min. The removal of Al also exposed the Al_2O_3 barrier layer that capped one end of the pore channels. This exposed Al_2O_3 barrier layer was dissolved by immersion in 3 M NaOH for 30 min at room temperature.[33] This process both opened the AAO pores and widened the nanochannels. The nitrocellulose-based mask that had coated and protected the Al_2O_3 membrane was removed by dissolution in acetone. The pore-widened, TiO_2 infiltrated AAO template was then heated to 500ºC for 1 h at a 5 ºC min^{-1} ramp rate to crystallize the TiO_2 coating and pyrolyze residual organics. It was at this stage where single-wall titania nanotube (SWTNT) electrodes (that would be used as control samples in DSSC testing and other characterizations) were transferred to FTO glass and integrated into DSSC electrodes following procedures described elsewhere.

Coated AAO templates for multi-wall titania nanotube (MWTNT) conversion were then wrapped in nickel foil (25.4 µm thick, McMaster-Carr, Cleveland, OH, USA) to minimize any significant warping of the structure due to structural changes, loaded into titanium tubes (2.5 cm diameter, 20 cm length; McMaster-Carr, Cleveland, OH, USA) containing a molar TiF_4/Al_2O_3 ratio of approximately 5.7:1, and sealed in a glovebox (via welding) under a high-purity argon atmosphere. The ampoules were heated to 335 ºC at a ramp rate of 5 ºC min^{-1} and held at this temperature for 8 h to react Al_2O_3 and TiO_2 with

TiF_4(g). After cooling, the as-reacted templates were exposed to pure, flowing oxygen (that, before entering the furnace, was passed through a heated water bath (50°C) at a rate of 1 slpm resulting in 94% humidity of the furnace outflow) at 250 ºC for 8 h to convert $TiOF_2$ into TiO_2, and then heated to 500 ºC for 1.5 h in air to further crystallize the reaction product.

Residual aluminum-bearing phases were then selectively removed by immersion in an aqueous 3 M NaOH solution for 1.5 h at room temperature to yield freestanding MWTNT arrays. SWTNT arrays were prepared in a similar fashion, but without the TiF_4 gas/solid reaction process of the MWTNT arrays.

To evaluate the use of such MWTNTs for the adsorption of functional dyes, and for use as electrodes in DSSCs, the MWTNTs were sinter-bonded at 500°C for 1 h in air to titania nanoparticle films (1.8 ± 0.2 mm thick) deposited onto fluorine-doped tin oxide (FTO) bearing glass slides (2.54 x 1.27 cm x 2 mm thick, 13 Ω/□, Hartford Glass Company).[33] A light-harvesting N719 dye (cis-di(thiocyanato)-*N*-*N'*-bis(2,2'-bipyridyl-4-carboxylic acid-4'-tetrabutyl-ammonium carboxylate) ruthenium (II)) (Solaronix, Aubonne, Switzerland) was introduced by immersion of the MWTNT-bearing FTO glass slides in a 0.3 mM solution of the dye in *t*-butanol/acetonitrile (1:1 volume) for 24 h. A Pt-coated counter electrode was prepared by depositing an ethanolic solution of 2 mg mL-1 H_2PtCl_6 onto a FTO-bearing glass slide containing a 1 mm diameter hole, followed by firing at 450°C for 15 min. A 25 mm thick thermoplast spacer (Meltronix 1170-25, Surlyn, Solaronix, Aubonne, Switzerland) containing a 0.79 cm diameter hole was used to separate the MWTNT-based working electrode from the Pt counter electrode. A redox electrolyte solution, consisting of 0.6 M 1-methyl-3-propyl imidazolium iodide, 0.1 M guanidinium

thiocyanate, 0.03 M iodine and 0.5 M *tert*-butylpyridine dissolved in a mixture of 85 vol% acetonitrile and 15 vol% valeronitrile, was then vacuum infiltrated into the space between the counter and working electrodes with a roughing pump for approximately 30 seconds or until all visible air bubbles in the electrolyte had popped. The assembly was sealed using a 60 μm thick thermoplast film (Meltronix 1162-60, Solaronix SA, Aubonne, Switzerland) and a cover glass slide. DSSCs with working electrodes containing SWTNT arrays were assembled in a similar fashion.

Dye loading measurements were conducted on five MWTNT and five SWTNT electrodes. After incubating in N719 dye for 24 h, then rinsing twice in dry acetonitrile by dunking for approximately 2 minutes, the dye was desorbed from the surfaces of the electrode by incubating in 2 mL of 0.1 M NaOH in water/ethanol, 1:1 vol. ratio for 5 min. The absorbance at 513 nm of the desorbed dye in the resulting solution was measured by UV-Vis spectroscopy and compared to six solutions of known N719 concentration (5 μM, 10 μM, 15 μM, 20 μM, 30 μM, and 115 μM/159 μM). The instrument was calibrated using new solutions for each experiment. An example of typical UV-Vis spectra and the corresponding calibration curves using peak absorbance at 513 nm are shown in Figures 2.2 and 2.3.

The fitted calibration curve was used to determine the concentration of N719 dye in the 0.1 M NaOH solutions using the peak absorbance of each electrode at 513 nm (Figures 2.2 and 2.3). Given that 2 mL of solution was used to desorb the N719 dye, the number of moles of N719 desorbed from the MWTNT electrodes can be calculated. The dye loading was then normalized to the area occupied on the FTO-bearing glass substrate by the SWTNT or MWTNT electrode. Optical image analyses (Image-J) were used to

accurately measure such electrode area. More specifically, the optical micrographs taken of each electrode were passed through an image analysis macro that filtered the image based on whiteness using four grayscale thresholds. The area determined at each threshold was averaged to give the electrode area. This method compensated for the detrimental effect of void space in the electrode.

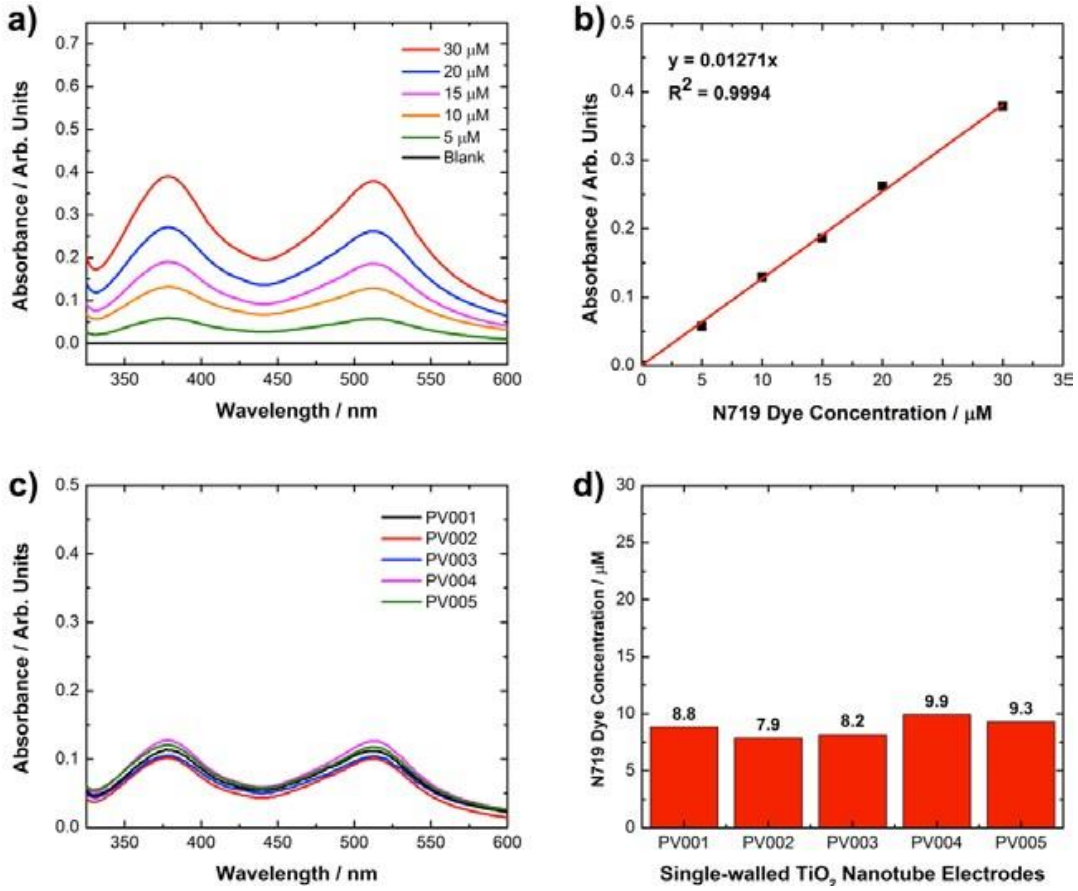

Figure 2.2. UV-Vis absorbance spectra of the N719 dye at various known concentrations (upper left). The absorbance at 513 nm was used to generate a calibration curve (upper right). UV-Vis absorbance spectra from 5 SWTNT electrodes (lower left), and the corresponding N719 dye concentration measured using the calibration curve (lower right). Berrigan, *et al*.[2] Reproduced by permission of The Royal Society of Chemistry.

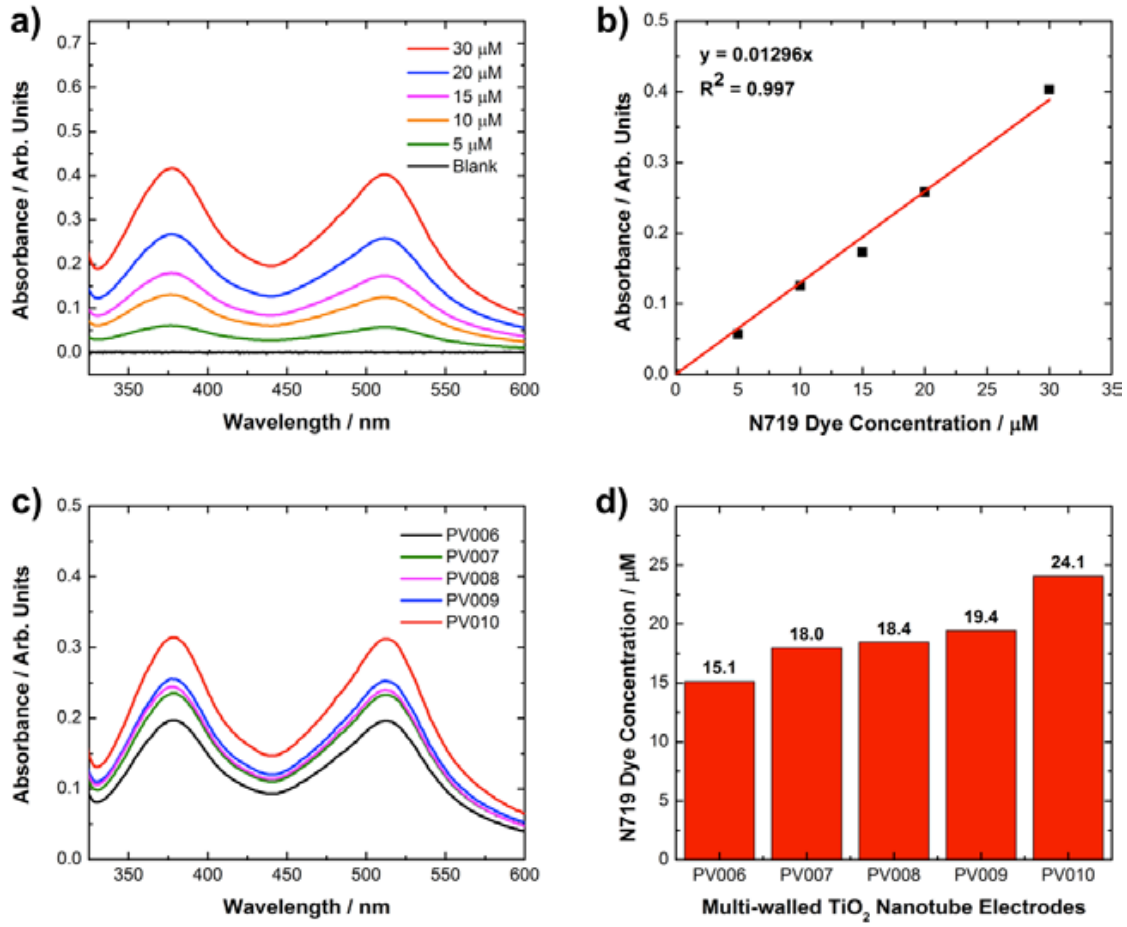

Figure 2.3. UV-Vis absorbance spectra of N719 at various known concentrations (upper left). The absorbance at 513 nm was used to generate a calibration curve (upper right). UV-Vis absorbance spectra from 5 MWTNT electrodes (lower left), and the corresponding N719 dye concentration measured using the calibration curve (lower right). Berrigan, *et al*.[2] Reproduced by permission of The Royal Society of Chemistry.

The micro/ nanoscale morphologies of the AAO templates and nanotube arrays were evaluated with scanning electron microscopy (1530 FEG SEM, LEO/Zeiss Electron Microscopy, Thornwood, NY) and transmission electron microscopy (JEOL 4000 EX TEM, Japan Electron Optics Laboratory, Tachikawa, Tokyo). The crystal structures of the nanotube arrays were evaluated at room temperature via X-ray diffraction (XRD) analyses conducted with Cu Kα radiation (Alpha-1, PANalytical Corp., Almelo, The Netherlands)

and selected area electron diffraction (SAED) analyses in the TEM. Current–voltage (I–V) measurements were conducted under AM 1.5 G conditions (Oriel 300 Watt solar simulator, 100 mW cm^{-2}) using an aperture with a measured area of 7.05 mm^2.

2.3 Results and Discussion

Secondary electron (SE) images of plan and cross-sectional views of specimens at various stages of conversion into MWTNT arrays are shown in Figures 2.4 and 2.5, respectively. The starting AAO templates possessed well-aligned vertical channels with an average diameter of 207 ± 29 nm and an average height of 13.2 ± 0.4 μm (the ranges refer to ± one standard deviation of measured values).

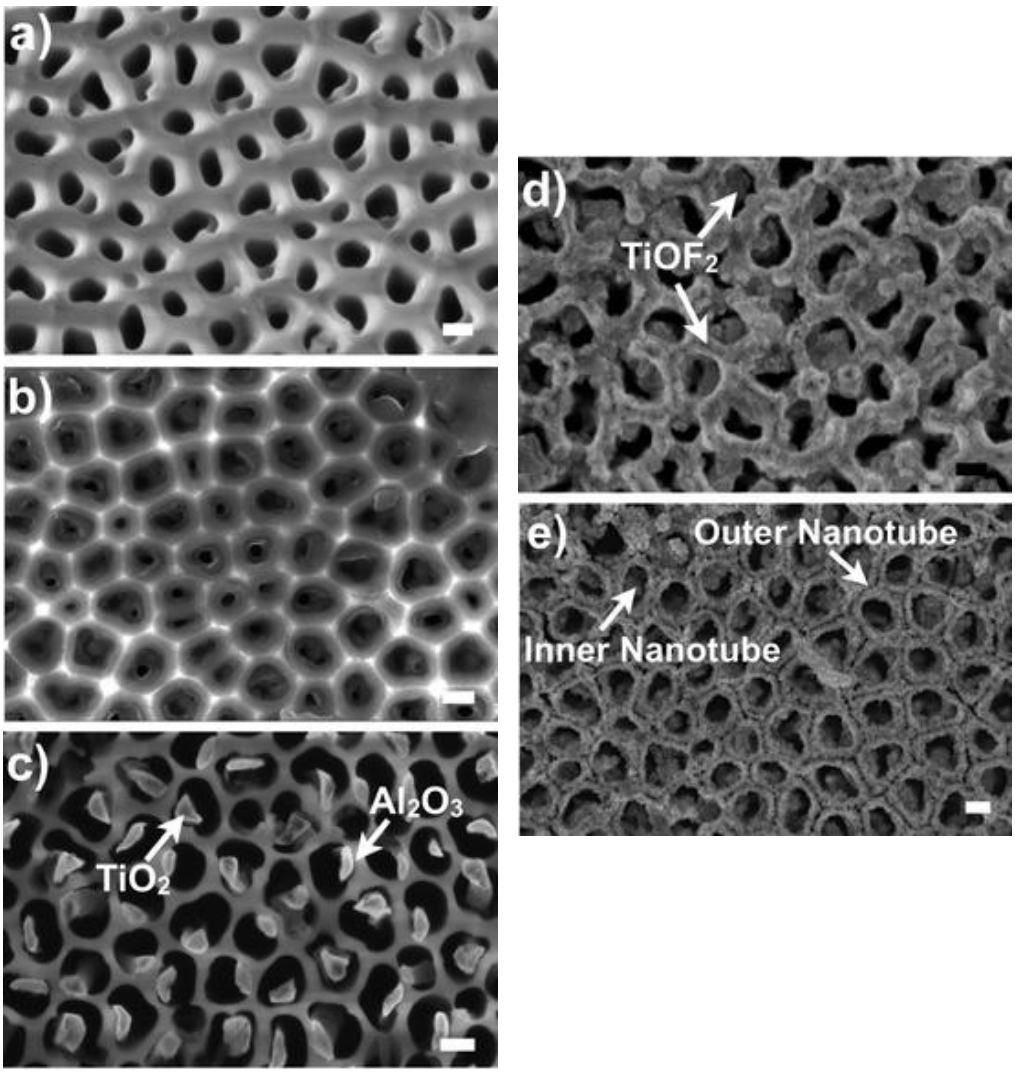

Figure 2.4. SE images of plan views of specimens obtained at various stages of conversion into MWTNT arrays: (a) a starting AAO template viewed top-down; (b) a coated template after two vacuum infiltrations with the Ti(IV) isopropoxide solution viewed top-down; (c) a coated template after dissolution of the Al backing and Al_2O_3 barrier layer viewed bottom-up; (d) a coated template after conversion of exposed Al_2O_3 into TiO_2 via reaction with TiF_4(g) viewed top-down; and (e) a freestanding MWTNT array generated after selective dissolution of non-titania phases from the coated/reacted template viewed top-down. All scale bars correspond to 200 nm. Berrigan, *et al*.[2] Reproduced by permission of The Royal Society of Chemistry.

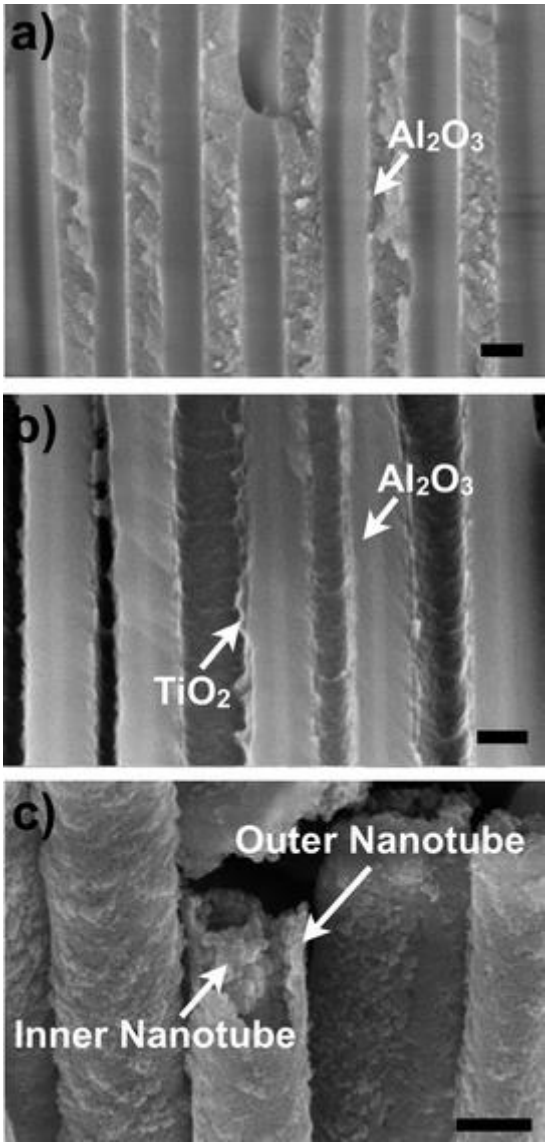

Figure 2.5. SE images of specimen cross-sections obtained at various stages of conversion into MWTNT arrays: (a) a starting AAO template; (b) a coated template after two vacuum infiltrations with the Ti(IV) isopropoxide solution; and (c) a freestanding MWTNT array after reactive conversion of the coated AAO template and selective dissolution of non-titania phases. All scale bars correspond to 200 nm. Berrigan *et al.*[2] Reproduced by permission of The Royal Society of Chemistry.

After double vacuum infiltration and hydrolysis of the alkoxide precursor, a continuous and conformal titania coating was observed to have formed on the AAO nanochannel walls (Figures 2.4b and 2.5b). Subsequent exposure to an aqueous 3 M NaOH solution (used to remove the alumina backing layer) then introduced space between the

AAO and the titania coating (Figures 2.4c) so as to expose alumina surfaces for subsequent gas/solid reaction. After thermal treatment at 500°C for 1 h in air to allow for organic pyrolysis and crystallization of the sol–gel coating, XRD analysis (Figure 2.6a) revealed distinct peaks for only anatase TiO_2. Scherrer analysis of these diffraction peaks yielded an average crystallite size of 11 ± 3 nm. The specimens were then allowed to react with $TiF_4(g)$ at 335°C for 8 h within a sealed Ti ampoule. XRD analysis (Figure 2.6b) of such a reacted specimen yielded distinct diffraction peaks for titanium oxyfluoride, $TiOF_2$, as the predominant phase.[77] Such $TiOF_2$ formation was consistent with a $TiF_4(g)$ / $Al_2O_3(s)$ reaction of the following type:

$$3TiF_4(g) + Al_2O_3(s) \rightarrow 3TiOF_2(s) + 2AlF_3(s)$$

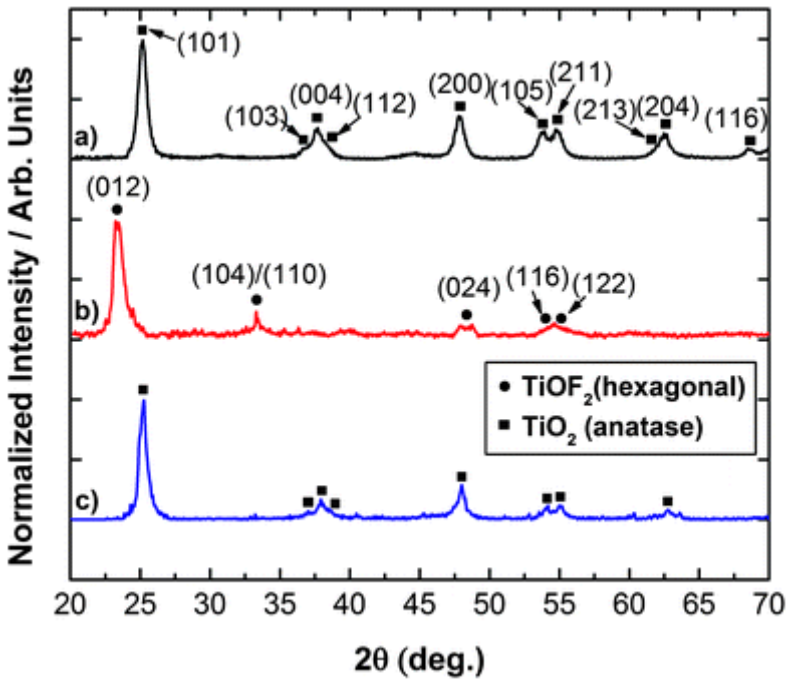

Figure 2.6 XRD analyses obtained from: (a) a TiO_2-coated AAO template after organic pyrolysis and crystallization for 1 h at 500°C in ambient air, then (b) reaction with TiF_4(g) at 335°C for 8 h, and (c) further reaction with humid, flowing oxygen (94% humidity, 1 slpm flowrate) at 250°C for 8 h, followed by thermal treatment at 500°C for 1.5 h in air. Berrigan, *et al*.[2] Reproduced by permission of The Royal Society of Chemistry.

The absence of diffraction peaks for the AlF_3(s) product of this displacement reaction was not surprising, given the glass-forming ability of this fluoride and prior reports of amorphous AlF_3(s) formation *via* low-temperature (≤ 350°C) fluorination of Al-bearing precursors.[78,79] The absence of predominant diffraction peaks for anatase TiO_2 in Figure 2.6b was consistent with the following reaction:

$$TiF_4(g) + TiO_2(s) \rightarrow 2TiOF_2(s)$$

Such reactive conversion of TiO_2 into $TiOF_2$ has been previously reported, albeit at ≥ 550°C.[80] After removal from the ampoules, the reacted specimens were exposed to

flowing, humid oxygen at 250°C to remove fluorine and convert titanium oxyfluoride into titania as per the following previously discussed reactions:[3,10]

$$TiOF_2(s) + H_2O(g) \rightarrow TiO_2(s) + 2HF(g)$$

$$TiOF_2(s) + 1/2O_2(g) \rightarrow TiO_2(s) + F_2(g)$$

After further heating at 500°C for 1.5 h in ambient air, XRD analysis (Figure 2.6c) revealed diffraction peaks for only anatase, with an average crystal size (from Scherrer analysis) of 14 ± 5 nm. High resolution transmission electron (HRTE) images of cross-sections of inner and outer titania nanotubes are shown in Figures 2.7a and b, respectively. Nanocrystals of 11 ± 3 nm dia. were observed within both inner and outer tube cross-sections, with lattice fringe spacings consistent with anatase (*e.g.*, the 0.352 nm and 0.233 nm spacings of (101) and (112) planes, respectively). SAED analyses obtained within inner and outer tubes (Figures 2.7c and d) were also consistent with the presence and absence of anatase TiO_2 and $TiOF_2$, respectively. Selective dissolution of the remaining amorphous Al-bearing phases (Al_2O_3, AlF_3) in an aqueous 3 M NaOH solution then yielded freestanding MWTNT arrays (Figures 2.4e and 2.5c).

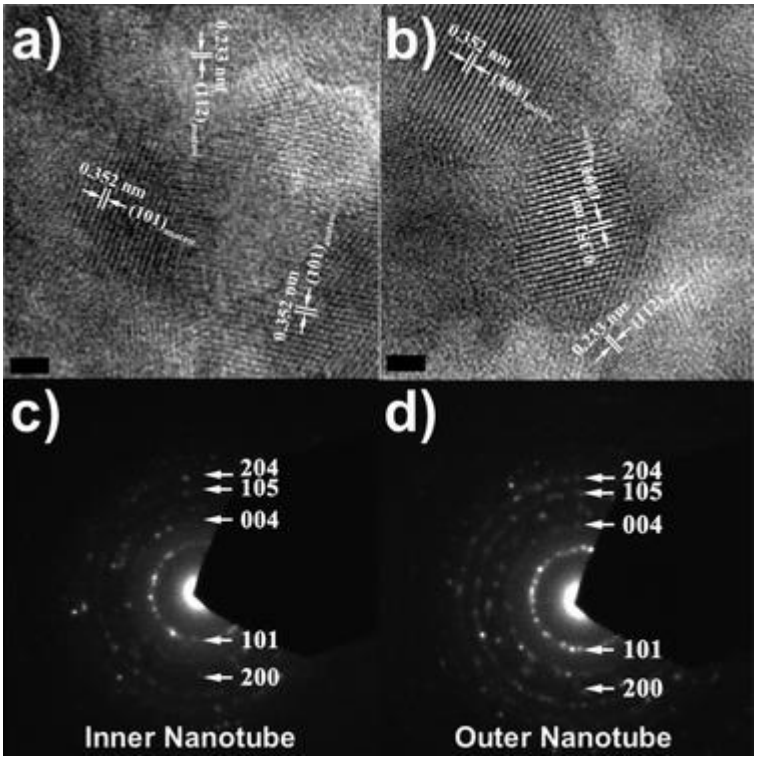

Figure 2.7. (a), and (b) HRTE images of the anatase nanocrystals in the inner (coating derived) and outer (reaction-derived) nanotubes, respectively, of a fully-converted freestanding MWTNT array. (c), and (d) Corresponding SAED analyses revealing the presence of only the anatase polymorph of TiO_2 with the inner and outer nanotubes, respectively. All scale bars correspond to 2 nm. Berrigan *et al.*[2] Reproduced by permission of The Royal Society of Chemistry.

SE and optical images of cross-sectional and plan views, respectively, of SWTNT and MWTNT arrays bound to FTO-coated glass slides are shown in Figure 2.8. Appreciable agglomeration of nanotubes into bundles of roughly 10–30 μm diameter, separated by gaps (microcracks) of up to about 20 μm, was observed within the SWTNT arrays. The MWTNT arrays, however, were much more resistant to such microscale bundling of nanotubes (*i.e.*, gaps of only a few micrometers or less were observed within these arrays), and exhibited a higher degree of vertical nanotube alignment relative to the

SWTNT arrays. The enhanced apparent rigidity of the MWTNT arrays avoided the need to use supercritical fluid drying methods to reduce capillary stresses.[76,81] Measurements of the diameters, lengths, and wall thicknesses of the SWTNT and MWTNT arrays, shown in Table 2.1, were used to calculate values of the "roughness factor" (*i.e.*, the area of the vertical sidewall surfaces of the nanotubes in the array, relative to the horizontal area of the FTO electrode on which the array was placed). The calculated roughness factors for the MWTNT and SWTNT arrays were 282 and 75, respectively. To test whether such increased sidewall area of the MWTNT arrays would result in enhanced dye loading, N719-bearing arrays were immersed in a solvent solution to extract this dye for subsequent analyses by calibrated optical absorption measurements. The average N719 dye loading of five MWTNT arrays was found to be 195 ± 31 nanomoles per cm^2, which was 2.2 times greater than the average value for five SWTNT arrays (87 ± 28 nanomoles per cm^2). (Note: while some of the dye was loaded onto the titania nanoparticle film used to sinter-bond a given nanotube array to the FTO electrode, similar nanoparticle films were used for both the MWTNT and SWTNT arrays). Hence, in addition to conferring enhanced resistance to nanotube bundling, the multi-wall, nested-tube nature of the coated/reacted arrays allowed for enhanced nanotube sidewall area and significantly higher dye loading.

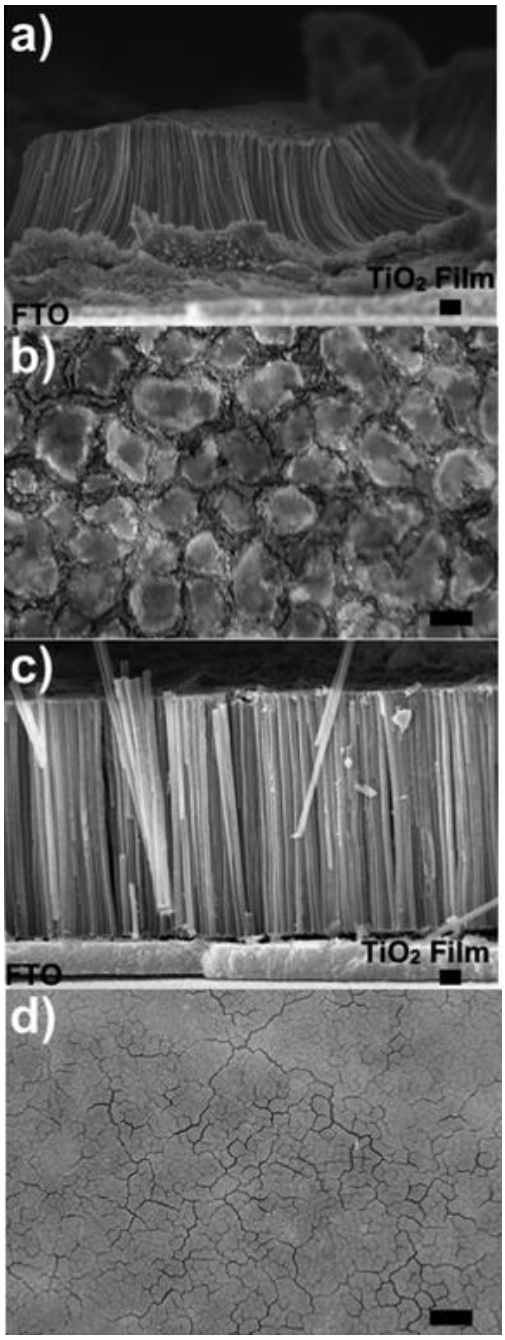

Figure 2.8. (a), and (c) SE images of cross-sectional views and (b), and (d) optical images of plan views of a SWTNT array (in (a) and (b)) and a MWTNT array (in (c) and (d)) bound to FTO-bearing substrates. Scale bars for SE and optical images correspond to 1 mm and 25 mm, respectively. Berrigan, *et al*.[2] Reproduced by permission of The Royal Society of Chemistry.

Table 2.1 Nanotube dimensions for the SWTNT and MWTNT arrays. Berrigan, *et al*.[2] Reproduced by permission of The Royal Society of Chemistry.

Specimen type	**Nanotube height (μm)**	**Inner nanotube wall thickness (nm); outer dia. (nm)**	**Outer nanotube wall thickness (nm); outer dia. (nm)**
SWTNT	13.2 ± 0.4	30 ± 10; 77 ± 20	—
MWTNT	13.2 ± 0.4	34 ± 7; 154 ± 40	80 ± 13; 426 ± 75

Average values indicated, with the error range corresponding to ± one standard deviation.

Quasi-one-dimensional structures, such as aligned TiO_2 nanotube arrays, have been reported to enhance both electron collection efficiency and light scattering when used as electrodes in DSSCs.[76,82] To demonstrate the utility of aligned MWTNT arrays as working electrodes, five DSSCs were prepared with MWTNT electrodes and five others were prepared with SWTNT electrodes. The performance data for these DSSCs are presented in Table 2.2 and current–voltage behaviors of SWTNT- and MWTNT-bearing DSSCs are shown in Figures 2.9-2.11. The best-performing MWTNT-bearing solar cell exhibited a power conversion efficiency of 6.5%, with the worst-performing MWTNT cell possessing an efficiency higher than the best-performing SWTNT cell (4.7% *vs.* 4.0%). The average values of short circuit current density and power conversion efficiency of the MWTNT-bearing DSSCs were 1.9 and 1.8 times higher, respectively, than for the SWTNT-bearing DSSCs. These values were not far from the 2.2 fold improvement in dye loading of the MWTNT arrays relative to the SWTNT arrays, which, in turn, was consistent with the non-agglomerated, nested nanotube (enhanced roughness factor) structure of the MWTNT arrays. It is worth noting that the average V_{oc} value of these MWTNT array-bearing DSSCs decreased by 18 mV relative to SWTNT-based devices. Such a modest reduction in the V_{oc} value was not surprising, given the larger surface area available for electron–hole

recombination in the MWTNT-based devices.[83]

Table 2.2. Dye-sensitized solar cell performance and dye-loading characteristics for SWTNT-bearing and MWTNT-bearing devices. Berrigan, *et al*.[2] Reproduced by permission of The Royal Society of Chemistry.

Parameter	**SWTNT devices**	**MWTNT devices**
J_{sc} (mA cm^{-2})	5.6 ± 2.0	10.4 ± 1.2
V_{oc} (mV)	728 ± 29	710 ± 30
FF	0.714 ± 0.04	0.714 ± 0.02
η (%)	3.0 ± 1.0	5.50 ± 0.8
Dye adsorption (nmol cm^{-2})	87 ± 28	195 ± 31

Average values of five devices indicated, with the error range corresponding to ± one standard deviation.

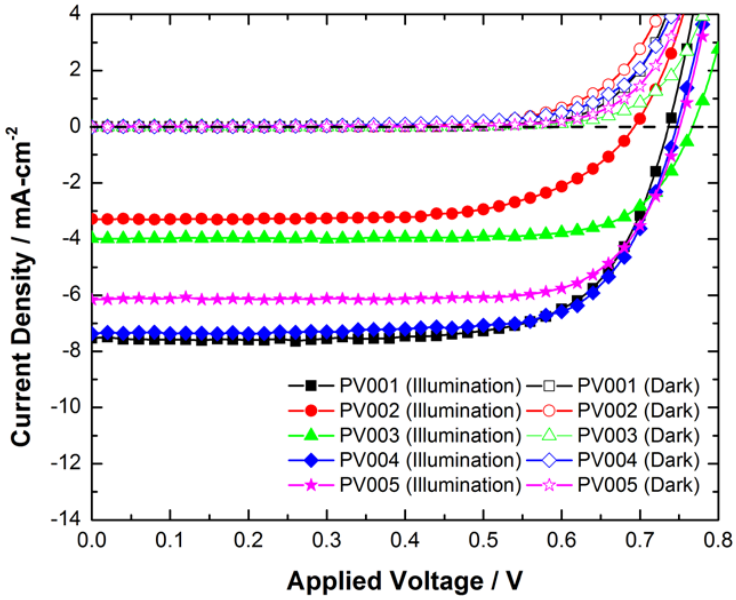

Figure 2.9. Current-voltage behavior of five dye-sensitized solar cells using SWTNT arrays as electrodes under both dark and illumination conditions. Berrigan, *et al.*[2] Reproduced by permission of The Royal Society of Chemistry.

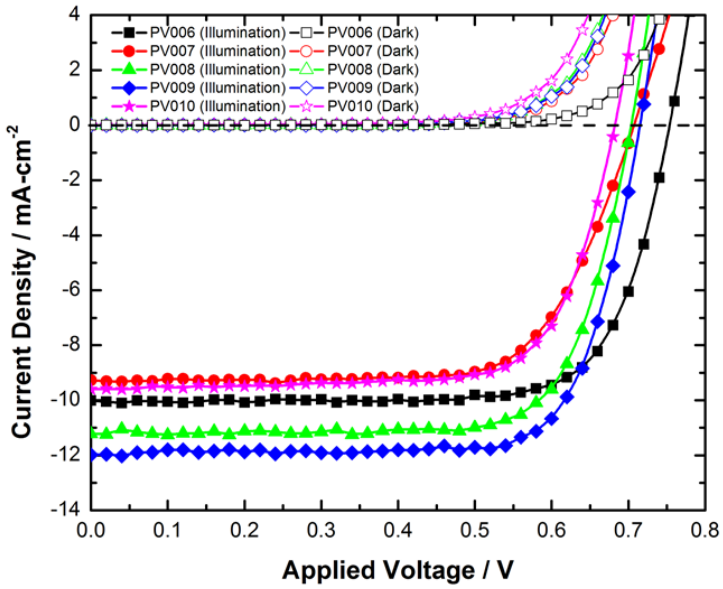

Figure 2.10 Current-voltage behavior of five dye-sensitized solar cells using MWTNT arrays as electrodes under both dark and illumination conditions. Berrigan, *et al.*[2] Reproduced by permission of The Royal Society of Chemistry.

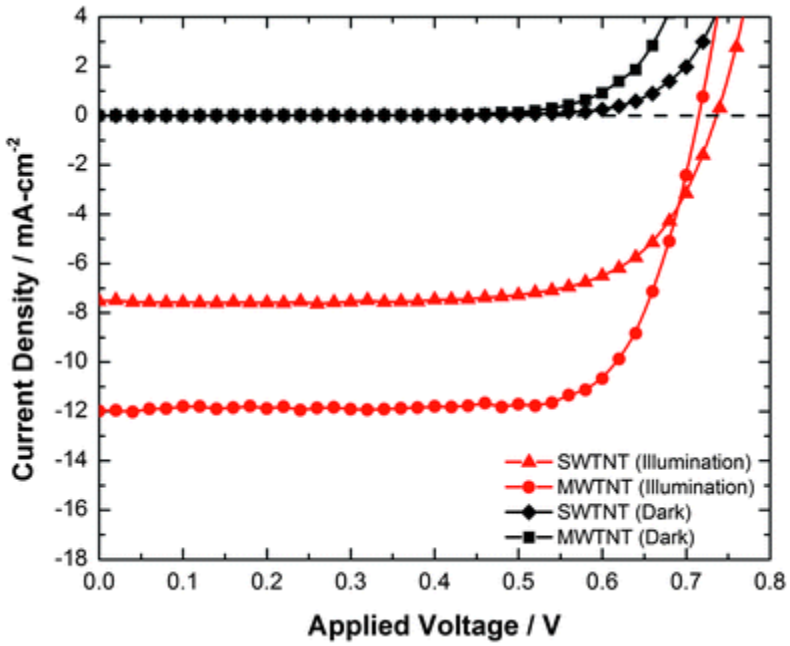

Figure 2.11. Current–voltage behavior of the best performing SWTNT- and MWTNT-bearing DSSCs in the dark and under AM 1.5G illumination. Berrigan, *et al*.[2] Reproduced by permission of The Royal Society of Chemistry.

The present process may be controllably altered to synthesize robust freestanding arrays of multiwall nanotubes with tailored dimensions and chemistries. The outer diameter, height, and wall thickness of the inner nanotubes can be tailored by adjusting the nanochannel diameter and height of the starting AAO templates (via modification of anodization conditions) and the number of sol–gel infiltration cycles. The inner diameter of the outer nanotubes can be tailored by controlling the etching process used to open up space between the coating-derived inner nanotubes and the AAO template, whereas the outer nanotube wall thickness can be tailored by controlling the extent of the $TiF_4(g)/Al_2O_3$ reaction. The inner and outer nanotubes may also possess different functional chemistries via appropriate selections of the sol–gel precursor and the halide used in the gas/alumina reaction. While the synthesis of well-aligned MWTNT arrays for

DSSCs has been demonstrated in the present chapter, this hybrid (coating and reaction) process may be used to synthesize uniform, well-aligned, multiwalled nanotube structures tailored for use as electrodes, (photo)catalysts, sensors, or filters/absorbers in a host of other applications.

2.4 Conclusions

A combined sol–gel infiltration and gas/solid displacement reaction method has been used for the first time to convert porous anodic Al_2O_3 (AAO) into robust, multi-wall nanotube arrays comprised of nanocrystalline anatase TiO_2. The nanochannel walls of the AAO template were first coated with a conformal layer of titania *via* two successive sol–gel vacuum infiltration treatments. Subsequent wet chemical etching was used to remove the aluminum backing and the alumina barrier layer at the base of the template, to generate flow-through membranes as well as to open up a gap between the AAO template and the titania coating. The exposed Al_2O_3 and TiO_2 were allowed to undergo reaction with $TiF_4(g)$ at 335°C to generate $TiOF_2(s)$. Reaction of this oxyfluoride compound with humid, flowing oxygen at 250°C and then air at 500°C resulted in fluorine removal and conversion into nanocrystalline anatase titania. The resulting multi-wall nanotube array consisted of inner TiO_2 nanotubes, derived from the sol–gel coating process, nested within outer TiO_2 nanotubes derived from the $TiF_4(g)/Al_2O_3(s)$ reaction process. The enhanced rigidity provided by the reaction-derived outer nanotubes inhibited nanotube agglomeration and microcracking upon drying of the multi-wall titania nanotube (MWTNT) arrays.

As expected from estimated values of the roughness factor, these open, uniformly aligned, multi-wall structures were able to absorb 2.2 times more of a light-harvesting N719 dye than single wall titania nanotube (SWTNT) arrays (prepared using a similar sol–

gel infiltration process but without the halide gas reaction process). Upon incorporation as electrodes within dye-sensitized solar cells (DSSCs), the MWTNT arrays exhibited average short circuit current density and power conversion efficiency values that were 1.9 and 1.8 times higher, respectively, than for DSSCs containing SWTNT array electrodes.

Although the utility of this hybrid (coating and reaction) process has been demonstrated *via* the synthesis of robust MWTNT arrays for DSSCs, this process may be used to generate well-aligned oxide nanotube arrays with dimensions and functional chemistries tailored for a variety of other chemical, photochemical, electrochemical, adsorption, and optical applications.

CHAPTER 3 FUNDAMENTAL KINETIC STUDIES OF THE GAS-SOLID METATHETIC CONVERSION REACTION OF Al_2O_3 INTO $TiOF_2$

3.1 Introduction

The conversion of complex, 3-D shaped Al_2O_3 reactant templates (e.g., porous anodic alumina) is challenging to model for quantitative kinetic analyses. To simplify such analyses, substrates with simple, uniform, regular shapes, such as flat plates or monosized spheres, are preferred. Were inexpensive monosized Al_2O_3 microspheres or nanospheres available, these could be preferable owing to a relatively high total surface area resulting in potentially enhanced reaction kinetics and the possibility of full conversion of the Al_2O_3. Due to a lack of such commercially-available, monosized, and inexpensive Al_2O_3 spheres, a flat plate Al_2O_3 substrate can be substituted for kinetic experiments. For this study, selected orientations of single crystalline Al_2O_3 (sapphire) wafers were chosen as the reactant material because of the availability of such wafers at modest cost and the relative simplicity of analytical solutions for various rate-limiting steps for this simple specimen geometry.

Literature on the TiF_4/Al_2O_3 gas-solid reaction is lacking. To the best of our knowledge, there has been no prior study of the shape-preserving conversion reaction of Al_2O_3 with TiF_4 to yield $TiOF_2$, nor prior work on the kinetic mechanism of such a reaction. This chapter will focus on the kinetic mechanism(s) responsible for the following possible metathetic conversion reactions:

$$3TiF_4(g) + Al_2O_3(s) \rightarrow 3TiOF_2(s) + 2AlF_3(s) \quad (1)$$

$$TiF_4(g) + Al_2O_3(s) \rightarrow TiOF_2(s) + 2AlOF(s) \quad (2)$$

$$2TiF_4(g) + Al_2O_3(s) \rightarrow 2TiOF_2(s) + Al_2OF_4(s) \quad (3)$$

3.2 Experimental Procedures

3.2.1 HTXRD Experiments

Shape-preserving inorganic conversions allow for the micro- and nano-fabrication of three-dimensional (3-D) structures with tailored chemistries, such as through the chemical conversion of 3-D silica-based microshells (frustules) of diatoms (microscopic algae) and porous anodic alumina (AAO).[84,85] A previously-demonstrated method has been used to transform silica-based templates into titania replicas via reaction with TiF_4(g) to yield an oxyfluoride intermediate, $TiOF_2$. High temperature X-ray diffraction (HTXRD) has been employed to evaluate the phase evolution and reaction kinetics of this conversion.[3] HTXRD analysis is an attractive in-situ method for dynamic evaluation of phase evolution and reaction kinetics for solid/solid and fluid/solid reactions.[86-90]

This technique has been often used to analyze gas/solid reactions where reactant gas species are available at high vapor pressure at room temperature (e.g., O_2, N_2, H_2, and CO_2).[91-93] Some reactions of scientific and technological interest involve reactant species that form gases with significant vapor pressures only at elevated temperatures (i.e. such reactant species are stable as solids or liquids at room temperature). In reactions involving TiF_4, such as those mentioned in Chapter 1 with Al_2O_3 or SiO_2, the TiF_4 reactant exists as a solid at room temperature, and sublimes at 285°C.[67] HTXRD analyses with gaseous TiF_4 are complicated by the need to generate and contain the hot, reactive gas near the other

reactant species (e.g., Al_2O_3 or SiO_2) in an otherwise inert atmosphere for a sufficient amount of time to enable evaluation of the reaction progress. Variation in temperature with location must be also avoided, as this could cause deposition of solid TiF_4 in cooler areas. For these reasons, refined experimental designs are necessary to allow for HTXRD analyses of these and other similar reactions.

In the present work, improvements have been made to the design and use of a sealed, heated, X-ray transparent chamber. This chamber is capable of containing a moderate pressure reactive gas generated from a solid source within the chamber (as opposed to a liquid source for loading purposes). Such a setup allows for the dynamic HTXRD analysis of a gas/solid displacement reaction. As discussed below, this design is an improvement of similar chambers made from aluminum for the study of the TiF_4-SiO_2 system and predecessors made from monolithic graphite for the evaluation of a magnesiothermic reaction.[94,95] This new chamber design has been successfully implemented to investigate the reaction between TiF_4(g) and Al_2O_3(s).

3.2.1.1 HTXRD Chamber Design

Chambers previously designed by S. Shian and K. Sandhage optimized the materials used for the evaluation of the TiF_4(g)/SiO_2(s) reaction; that is, window materials were selected that were relatively transparent to X-rays, inert with the gas reactant (TiF_4), able to maintain a gas tight seal and to exhibit adequate mechanical strength under the vapor pressure generated at the operating temperature (up to 350°C), and relatively easy to machine or form.[94] Owing to its thermal stability at modest reaction temperatures and relative inertness to TiF_4, aluminum was chosen as the chamber material. Additionally, aluminum has a relatively high thermal conductivity (2.37 W/cm K at 27°C and 2.31W/cm

K at 327°C)[96] and is relatively easy to machine. The high thermal conductivity helps ensure a uniform temperature distribution inside of the chamber and good heat transfer to the thermocouple located just outside of the chamber.

Also, aluminum is relatively X-ray transparent when in the form of a thin layer. It was possible to line the windows of the chamber with 13 μm thick aluminum foil. However, to resist the buildup in vapor pressure within the chamber, a stronger X-ray transparent material needed to be layered with the aluminum foil. Kapton has been widely used as an X-ray transparent (window) material where mechanical stability at modest temperature is required.[97,98] However, Kapton reacts with TiF_4(g) at the reaction temperature and becomes impenetrable to X-rays and optically opaque. By forming each window with an outer layer of Kapton (130 μm thick) and inner layer of aluminum foil (13 μm thick), Cu Kα X-rays can penetrate both windows of the chamber and theoretically retain more than 57% of the incident beam intensity.[99]

Figure 3.1 and Figure 3.2 show a schematic of the cross-sectional side view and optical images of the re-designed reaction chamber consisting of a main aluminum body, a layer of windows (Kapton and aluminum foil), aluminum window frames, reactant TiF_4(s), and reactant Al_2O_3 wafer. A thin strip of nickel (approximately 1 mm wide) was wrapped (tightly pressed) around the Al_2O_3 wafer (8.5 mm) parallel to the direction of the beam, and maintained this tightly wrapped position throughout reaction. Improvements to previous designs include changes to the shape of the main chamber body to allow for enhanced sealing and uniform exposure of the Al_2O_3 to the TiF_4(g). The main body had outer dimensions of 27 mm diameter x 10 mm deep and inner dimensions of 18 mm diameter x 10 mm deep. The chamber body was machined from aluminum 6061 alloy

tubing with starting dimensions of 31.75 mm outer diameter and 25.40 mm inner diameter (McMaster-Carr, Atlanta, GA). The exterior was ground on four perpendicular sides to sit flat (so that it could not easily roll over and to minimize the total height and width of the chamber). The round shape of the interior chamber wall and rounded corners of the exterior wall were left intact to allow a uniform chamber seal, which yielded a significant improvement over previous designs where squared-off chamber seals were a common cause of gas leaks. The side surfaces of the main body that came in contact with the window were machined 1 mm deep around the middle 4.5 mm on each side (leaving a 1 mm wide wall on each inner and outer diameter in contact with smooth window frame) to maximize the pressure seal before being polished flat using a 1 μm diamond suspension (Metlab Corp, Niagara Falls, NY). Six holes were drilled through the middle of the wall thickness allowing the window frames to be bolted together using 18-8 stainless steel screws and hex nuts (McMaster-Carr, Atlanta, GA) on either side of the body, allowing a gas-tight, secure compartment. The aluminum window frames were machined, from the same aluminum 6061 alloy as the body, to be 1.5 mm thick with six holes drilled through each to align with the body.

The reactant TiF_4(s) (99% purity, Advanced Research Chemicals, Catoosa, OK; XRD showing phase purity of TiF_4 powder is provided in Figure 3.3) was measured out onto the bottom surface of the main chamber interior and the Al_2O_3 substrate (~140 mg, polished single crystal with C- {001} or R- {012 plane orientation, $R_a \leq 0.3$ nm arithmetic average roughness (data provided by vendor), University Wafer, Boston, MA) and nickel standard (76 μm thick shim, 99% purity, McMaster-Carr, Atlanta, GA)) were placed approximately 2 mm above the TiF_4 and rested flat on the rounded chamber walls (Figure

3.2).

Two unique orientations of Al_2O_3 wafers were employed to test changes in reaction kinetics on different Al_2O_3 crystal planes. The two orientations chosen (C-plane and R-plane) are widely available and are unique in their respective surface chemistries. While there have been no reports of gas/solid reaction kinetics of these orientations with TiF_4 or other metal halides, other types of reactions on these sapphire surfaces have yielded significant differences in the behavior of these orientations. Some studies have attributed such variations seen to differences in the sapphire surface chemistry.[100,101] C-plane Al_2O_3 has been reported to possess doubly coordinated hydroxyl groups on the surface.[100,101] R-plane Al_2O_3 has a significant amount of singly coordinated hydroxyl groups on the surface and thus may be more pH sensitive and may be more reactive.[100,101] Other groups have examined variations in film growth on C-plane and R-plane Al_2O_3 (during adsorption or catalytic growth) and have found the primary effect to be the product crystal orientation as opposed to kinetic variations.[102-104] While these results in the literature are not for the same kinds of reactions, they do indicate that differences may be seen in these two sapphire orientations in terms of reaction behavior. Additionally, the d-spacings between diffracted planes in these two orientations are different from those d-spacings associated with $TiOF_2$ and other potential byproducts, making these orientations optimal for unambiguous XRD analysis. Thus, if there is a difference in reaction due to crystal orientation, the two orientations chosen may clearly illustrate this variation.

The Al_2O_3 substrate plate (10 mm x 8.5 mm) was cut to provide ample open space by the windows to allow the gas reactant to flow throughout the chamber and was also designed to be wide enough to allow sufficient surface area for X-ray absorption at low

incident angles (ω) and thus sufficient signal-to-noise ratio in diffracted intensity to the detector. The nickel was used as an inert standard material throughout the reaction to allow for calibration of X-ray intensity variations. 130 μm thick Kapton film (McMaster-Carr, Atlanta, GA) was cut into 22 mm diameter disks, and 13 μm thick aluminum (McMaster-Carr, Atlanta, GA) was cut into 28 mm x 28 mm squares, to fully cover the window opening (note that the aluminum, but not the Kapton, was easily penetrated by the screws attaching the windows to the body).

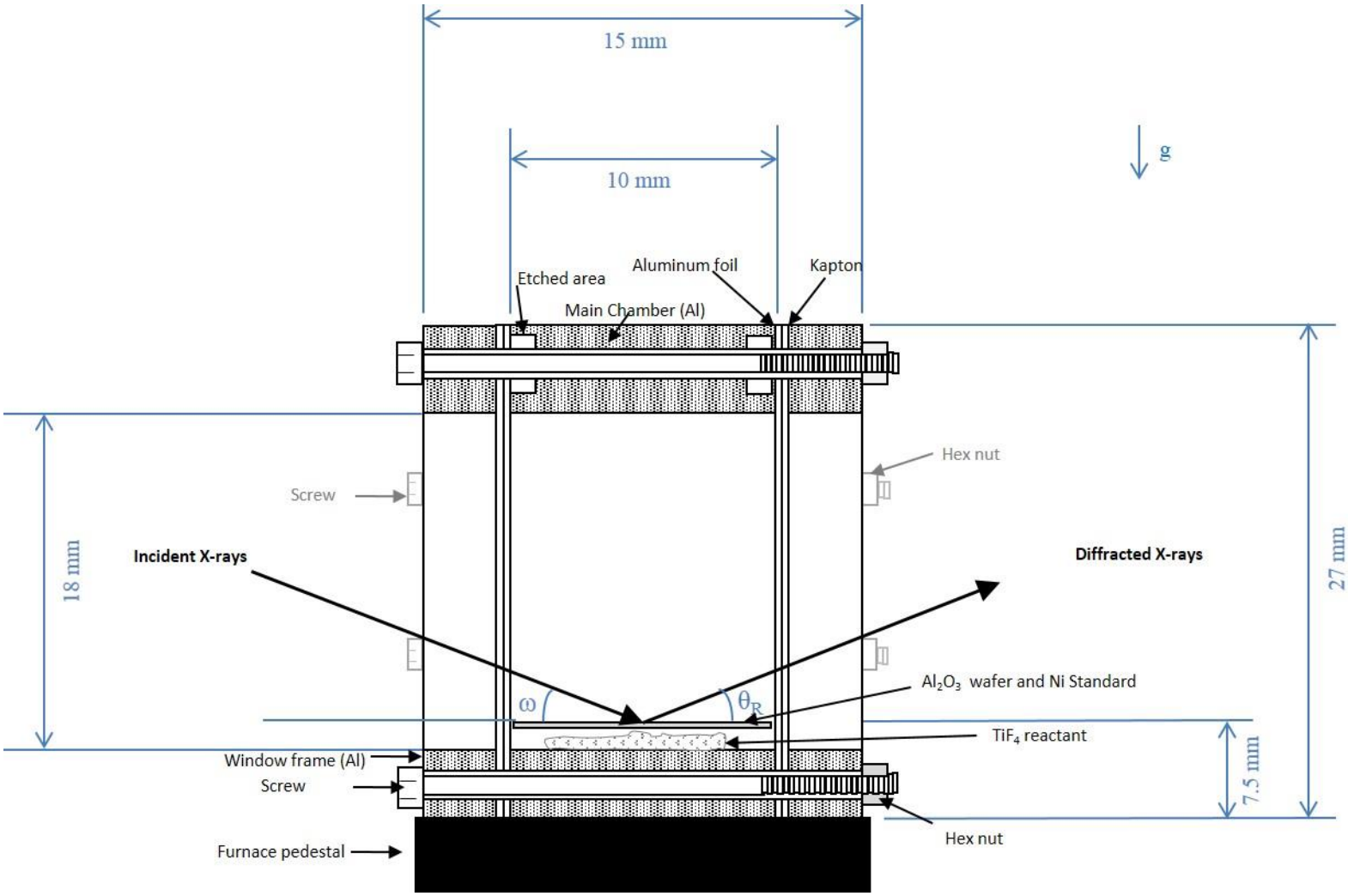

Figure 3.1. Reaction chamber schematic illustration (cross-section) with critical dimensions labelled.

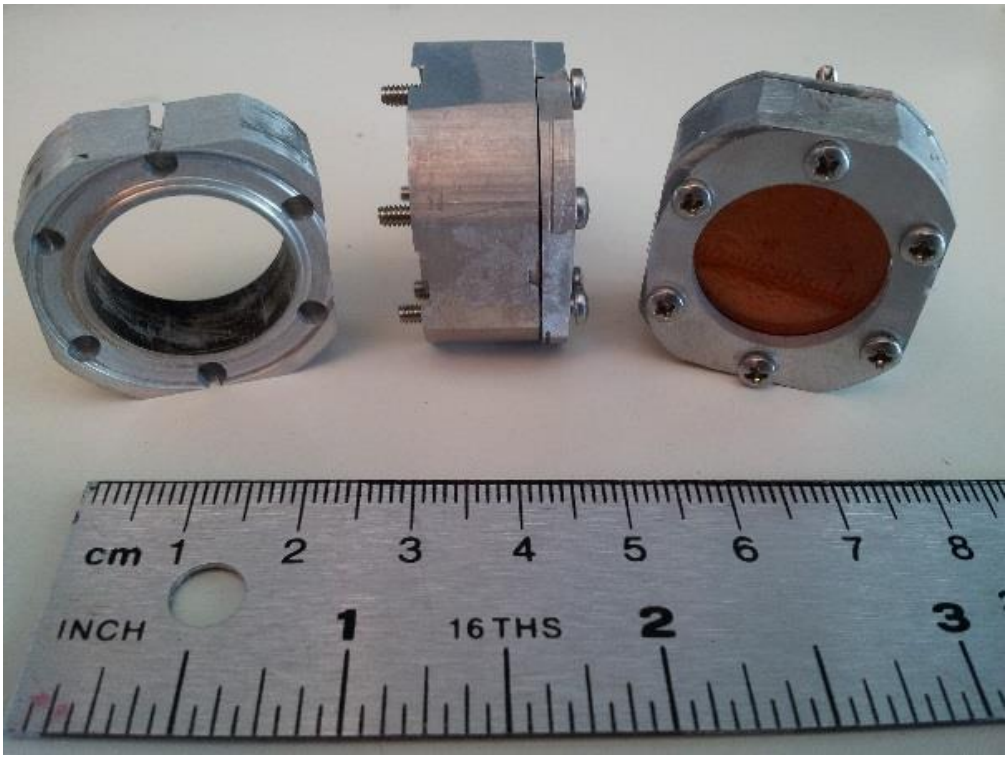

Machined indent increases pressure to improve seal of chamber

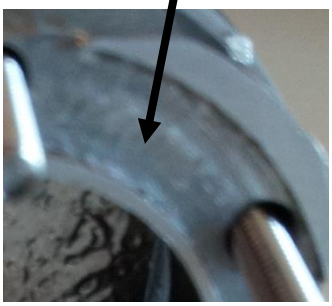

Figure 3.2. Optical images of partially assembled reaction chambers viewed from various directions. The lower left image illustrates the machined groove which allowed for a high pressure seal between the chamber and the window. The lower right image shows an Al_2O_3 wafer with Ni standard sitting in position above a powder reactant (TiF_4(s) for all reactions, but for illustration purposes here, a similarly sized amount of an inert white power (Al_2O_3) was used).

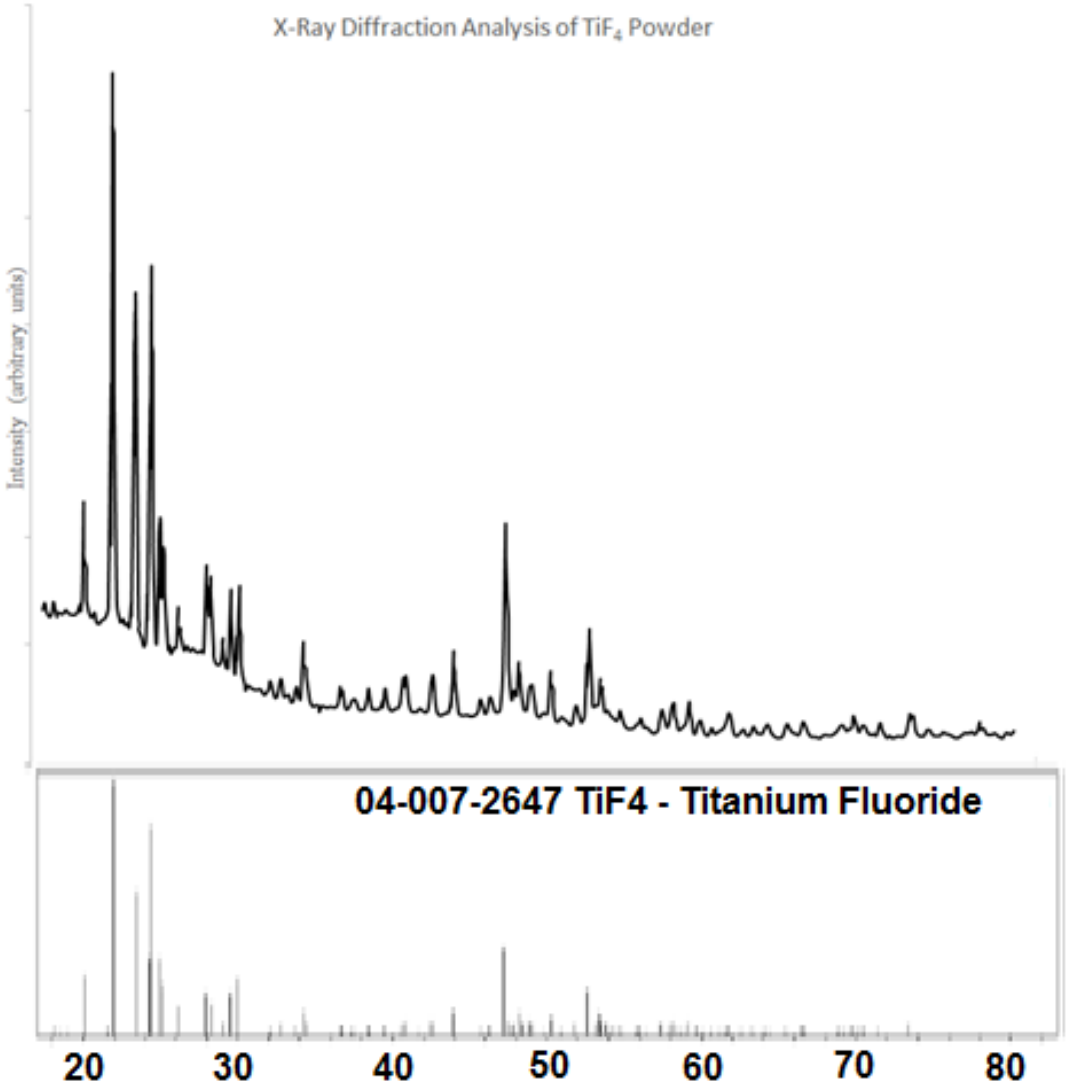

Figure 3.3. XRD analysis of TiF_4 powder used for reaction studies (99% purity, Advanced Research Chemicals, Inc., Catoosa, OK). The data matches the XRD pattern reported in the literature (PDF# 04-007-2647, ICDD).

3.2.1.2 HTXRD Experimental Setup

In a typical experiment, 75 mg of solid TiF_4 powder was loaded into the chamber. The Al_2O_3 substrate with Ni standard attached was oriented horizontally within the main chamber, above the TiF_4 (Figure 3.2). The TiF_4/Al_2O_3 molar ratio of 1:2.27 is smaller than what was used in previous chapters and would not allow for complete conversion of the

wafer. This change in ratio was necessary to work within the confined dimensions of the reaction chamber. However, significant excess TiF_4(s) (on the order of 90%) was still seen after reaction at the most extreme conditions in the reaction chamber, signifying that, even at the molar ratio used, enough TiF_4 was available to maintain a constant TiF_4 vapor pressure inside the reaction chamber during the course of the reaction.

Afterwards, the window frames were secured to the main body. Both the reactant loading and chamber sealing were performed inside an argon-filled glove box (Model Omni-Lab, Vacuum Atmosphere, Hawthorne, CA) maintained at an oxygen partial pressure below 0.1 ppm. The sealed reaction chamber was placed on top of the furnace pedestal and inserted into the high-temperature X-ray diffraction (HTXRD) system, which was purged with helium gas and heated with an Anton-Paar HTK 1200 high-temperature furnace (Graz, Austria). The HTXRD system chamber was heated at a rate of 20°C/min to the desired reaction temperature and held for up to 24 h. The temperature inside the reaction chamber at the surface of the Al_2O_3 substrate was calibrated using a differential thermal expansion method as described by Drews[105] and implemented previously on a similar system by Shian.[10]

Remaining unreacted TiF_4(s) was observed after all reaction conditions examined, which ensured that the chamber was well sealed and remained sealed throughout the reaction. The standard Ni (111) diffraction peak was checked for any increase in intensity at a constant temperature, which could happen due to changes in gaseous density. Because no gaseous byproducts are expected in this reaction, as long as there was excess TiF_4(s), the density of gas inside the reaction chamber should remain constant and, thus, the intensity of the standard peak should not vary. Were a gaseous by-product formed in a

sealed container, one might expect a decrease in Ni standard peak intensity due to increased X-ray absorption in the gas. Should a leak occur in a system with no gaseous product, one might expect to see an increase in Ni standard peak intensity due to a decrease in TiF_4(g) pressure (as it leaked from the system). In this system, no changes were detected in the Ni (111) peak indicating no gaseous by-products and no leaks.

Diffraction profiles were measured with an MPD Panalytical Diffractometer (Almelo, The Netherlands) configured with Bragg-Brentano geometry, a Cu Kα X-ray radiation source (1.5405980 Å), and helium atmosphere (for low atmospheric absorption of X-rays). The peak profile data acquisition was conducted using a solid-state position-sensitive ultrafast detector. A programmable divergence slit, a mask 10 mm wide, and a Soller slit preventing axial divergences greater than 0.02 radians were placed in the incident beam path. An anti-scattering slit of 5.0 mm and 0.02 radian Soller slit were used in the diffracted beam path. Figure 3.4 illustrates the path of the beam in the X-ray measurement circle from the X-ray generation tube, through the reaction chamber, and into the X-ray detector.

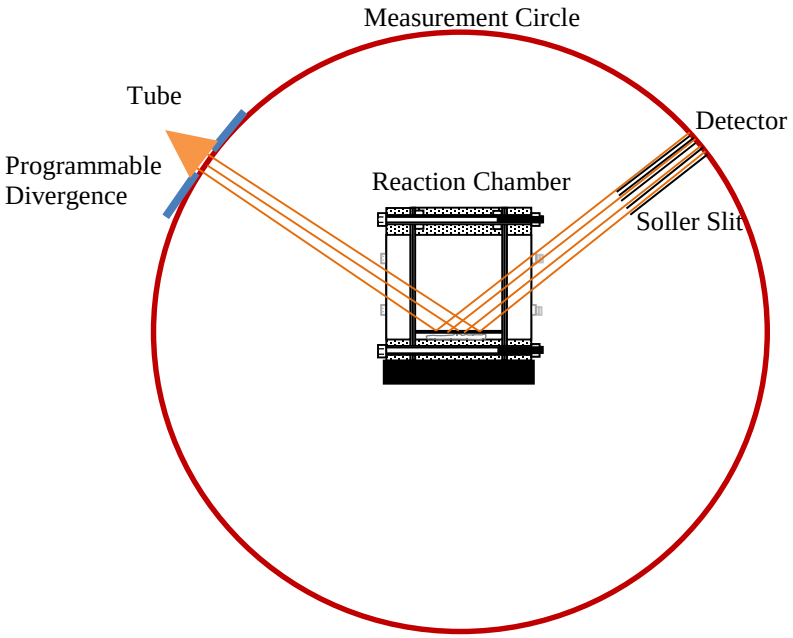

Figure 3.4. Schematic illustration showing X-ray diffraction beam path from the X-ray generator tube through the reaction chamber and to the detector.

3.2.2 Furnace Experiments

To study the microstructural evolution of the sapphire wafers most efficiently, conversion reactions were conducted inside an additional laboratory box furnace (which allowed for quick heat-up and cool-down rates) in addition to conversion reactions conducted inside the HTXRD. The furnace temperature, and heating and cooling rates, were calibrated via an external thermocouple (which was previously calibrated with an Ametek CTC1200A Compact Temperature Calibrator, Allerod, Denmark) placed next to the reaction chamber inside the furnace and were controlled to match the HTXRD parameters used. The box furnace was purged with flowing argon gas. Such rigorous control allowed for direct correlation of samples reacted at a given temperature for a given time in either setup. To verify proper calibration of the two systems, {001} sapphire wafers (inside Al reaction chambers with TiF_4/Al_2O_3 molar ratio of 1:2.27) were heated at

20°C/min to 310°C, reacted at this temperature for 0.5 h, and cooled at 20°C / min, before being removed from the reaction chambers and characterized by XRD in Bragg-Brentano geometry. Using a pseudo-Voigt fitting with a fixed cubic spline background curve, as shown in Figure 3.5, the area under the primary $TiOF_2$ peak was compared to the area under the Al_2O_3 peak to check that the ratio remained constant and thus that the amount of $TiOF_2$ formed in each system was constant. The area under the $TiOF_2$ primary peak was equal to 2.51-2.57% and 2.43-2.49% of the area of the (006) sapphire peak for the HTXRD furnace and the box furnace, respectively. By Scherrer analysis, the $TiOF_2$ crystallite size was found to be 42 ± 4 nm and 43 ± 3 nm after reaction in the box furnace and HTXRD system, respectively. Such similarities in the relative quantities of $TiOF_2$ and crystallite size confirmed the proper calibration of the box furnace to the HTXRD furnace.

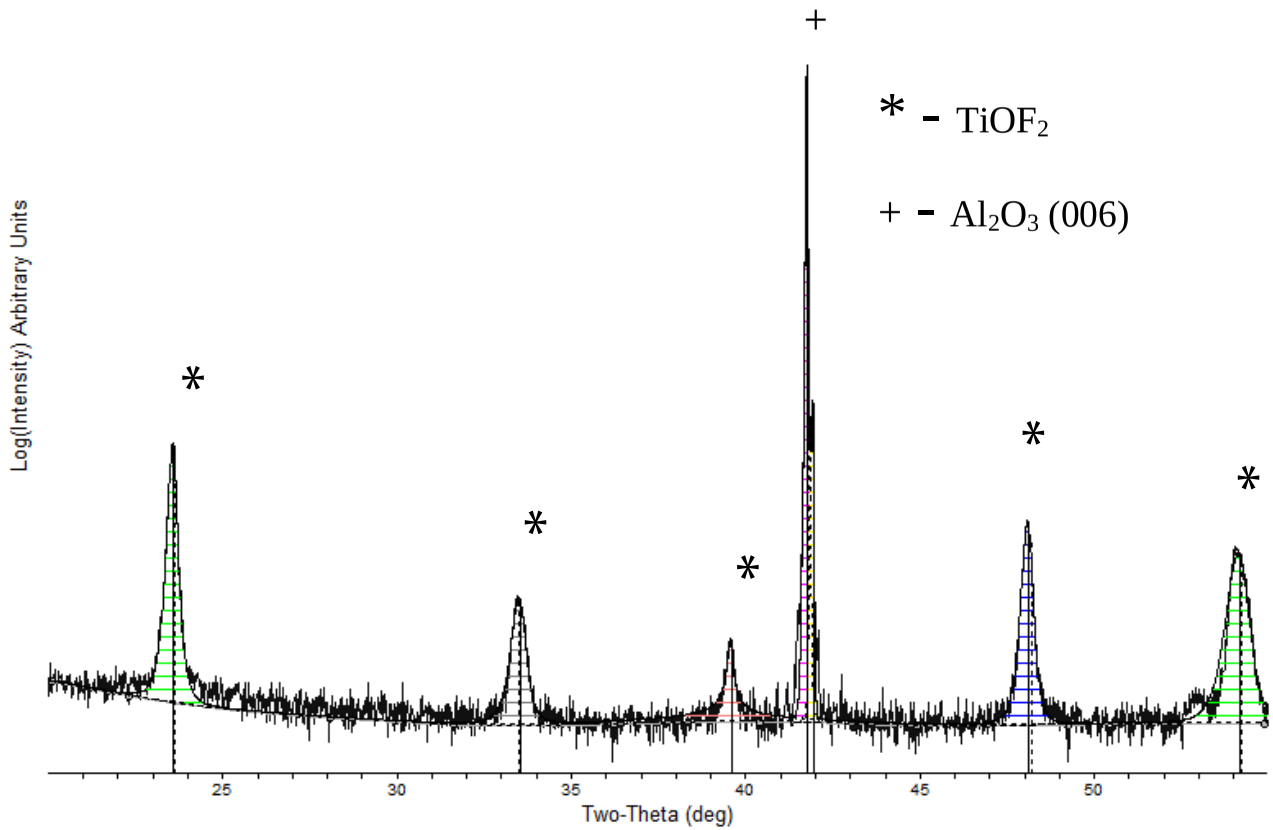

Figure 3.5. XRD analysis of a (001) Al_2O_3 wafer after reaction with TiF_4(g) at 310°C for 30 min in a box furnace. The spectrum illustrates the relative (logarithmic) intensities of the Al_2O_3 and $TiOF_2$ peaks and is fitted with a pseudo-Voigt curve. This spectrum and fitting was used to establish the relative amounts of each crystalline material and the average $TiOF_2$ crystallite size.

3.2.3 Modeling Procedure

The extent of reaction was characterized with the aid of Origin Pro software (version 9.0, OriginLab Corporation, Northhampton, MA) by measuring the area under the primary $TiOF_2$ diffraction peak (the cubic $TiOF_2$ (001) peak). The peak height, FWHM, shape, and skew values were refined during profile fitting using the Pseudo-Voigt model.[106] The peak area of $TiOF_2$ was normalized to the peak area of the inert Ni standard for a given reaction temperature and time. During the HTXRD experiment, the reaction was continued until the normalized (001) peak area of $TiOF_2$ (located near $2\theta = 23.5°$) reached a steady plateau for the highest temperature (385°C) data set (where the most product had formed). The fraction of reaction product $TiOF_2$ for all temperatures and times examined was normalized to the highest temperature (385°C) sample; that is, at a given time, the fraction of the reaction product $TiOF_2$ was defined as the ratio of the instantaneous peak area to the maximum peak area observed (at 385°C) for all $TiOF_2$ products. Simultaneously, the primary peak for the single crystalline Al_2O_3 wafer was measured to determine whether a comparable loss of area and plateauing effect was seen. However, upon examination of the Al_2O_3 peak, no noticeable loss in area was measured (i.e. any loss was within one standard deviation for a given peak area measurement). Additionally, the primary peak of Ni, used as a standard inert material, was tracked to account for any variation in peak areas due to environmental variability, such as changes in gas pressure causing an increase in X-ray absorption and no variations were found.

3.2.4 Microstructural Characterization

The microstructures formed after reactive conversion of single crystalline Al_2O_3 were characterized via SEM (1530 FEG SEM, LEO/Zeiss Electron Microscopy,

Thornwood, NY or 1550 FEG SEM, LEO/Zeiss Electron Microscopy, Thornwood, NY) and TEM (Jeol 4000X, Japan Electron Optics Laboratory, Tachikawa, Tokyo or Technai F30 TEM, FEI, Hillsboro, OR). Chemical analyses were performed using EDX mapping. Atomic Layer Deposition of ZrO_2 (used for microstructural characterization of potential pores) was performed using a Cambridge Fiji Plasma ALD system (Cambridge NanoTech, Waltham, MA). Time-of-flight secondary ion mass spectrometry (IONToF TOF-SIMS 5-300, ION-TOF GmbH, Münster, Germany) was used to analyze the molecular and elemental species present in reaction products.

3.3 Results and Discussion

3.3.1 HTXRD Results and Analysis

Samples contained in HTXRD reaction chambers were heated to temperatures ranging between 270°C and 385°C and evaluated by X-ray diffraction analyses during reaction for up to 8 hours before cooling. After cooling, but before removal from the HTXRD chamber, X-ray diffraction analyses of the reacted samples was performed at room temperature. Figures 3.6 and Figure 3.7 show XRD scans of the different Al_2O_3 wafer orientations before and after reaction for 8 h at 385°C, respectively. Wafer orientations were chosen such that the diffracting d-spacing values of Al_2O_3 would not overlap diffraction peaks from other solids (e.g. for $TiOF_2$, Ni, and Al) that would be measured during HTXRD analyses. Due to the oriented, single crystalline nature of the corundum wafers, only one family of diffracting corundum crystalline planes were detected for each wafer.

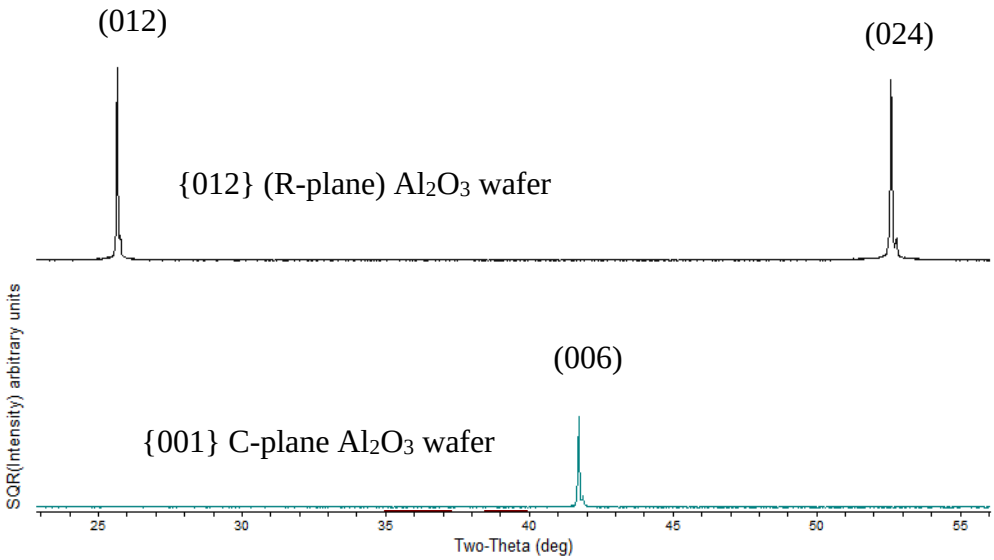

Figure 3.6. XRD analyses of Al_2O_3 wafers before reaction.

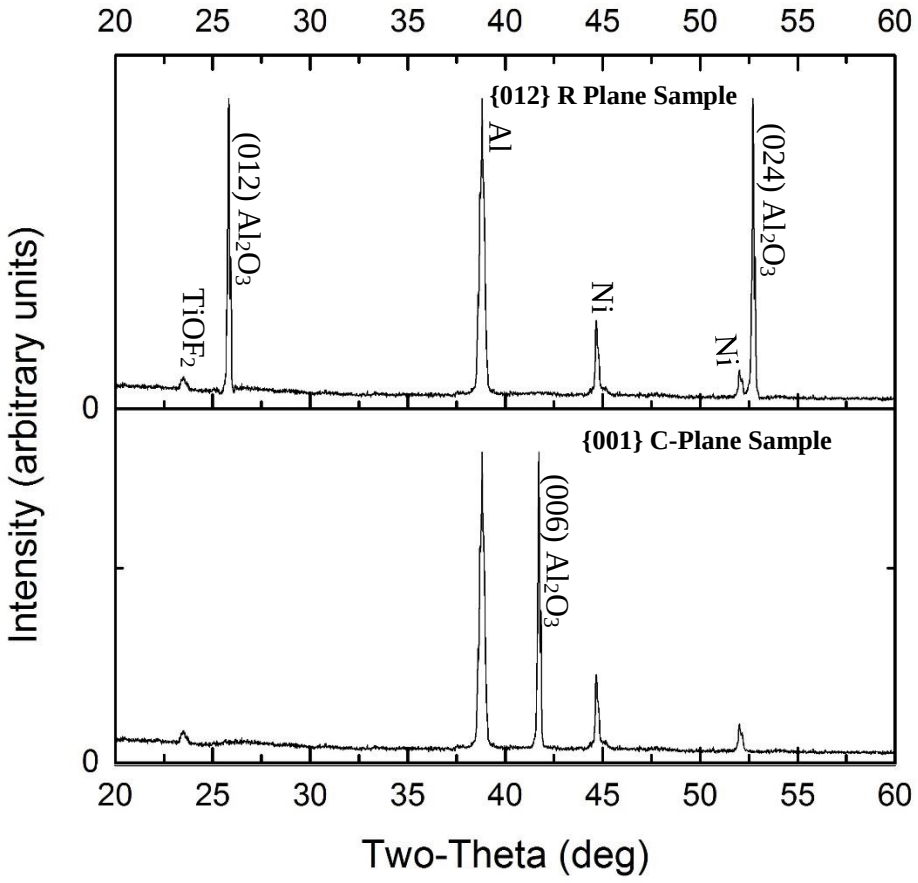

Figure 3.7. XRD analyses of Al_2O_3 wafers after reaction with TiF_4 (g) at 385°C for 8 h.

Figure 3.8 and 3.9 show representative HTXRD analyses of the primary (012) $TiOF_2$ peak, obtained during the reaction of a single crystalline Al_2O_3 with TiF_4 gas at 310ºC for C-plane and R-plane Al_2O_3, respectively. A diffraction peak for the (012) plane of $TiOF_2$ was apparent in the first scan and increased in intensity with increasing reaction time for each Al_2O_3 orientation. During such analyses, the first several scans were conducted over a limited 2θ range ($22° \leq 2\theta \leq 25°$) so that a shorter scan time (25 s) could be completed while maintaining a high signal-to-noise ratio. The initial scan time and

range were selected in order to capture rapid reaction dynamics near the beginning of the reaction which were not traceable when longer initial scan times and ranges were used. After approximately 10 minutes, longer scans (approximately 4 minutes in duration when combined) were conducted in discrete intervals from 22-27° and 40-47°. These intervals permitted each peak of interest (those associated with $TiOF_2$ (012), Ni (111), and Al_2O_3 (012) or (006)) to be scanned while minimizing the time required between consecutive scans of each peak.

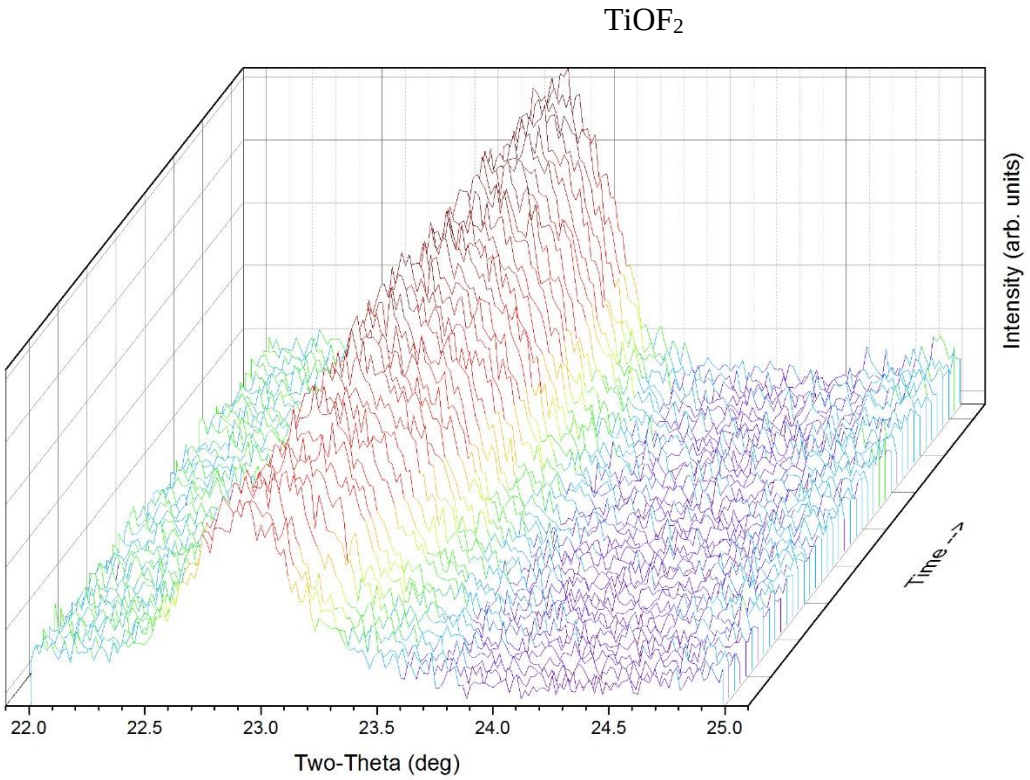

Figure 3.8. Isothermal HTXRD scans of (006) C-plane Al_2O_3 wafer planes reacted with TiF_4(g) at 310°C. In this plot, the time interval between selected scans (i.e. from the start of one scan to the start of the next scan) was 20 ± 1 seconds. In a typical run, the scans were performed over short two-theta intervals for each peak of interest to minimize the time required between two consecutive scans of each peak.

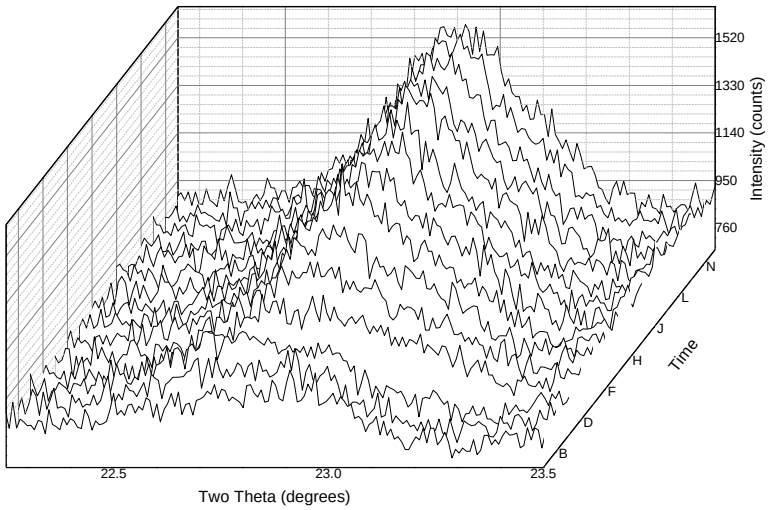

Figure 3.9. Isothermal HTXRD scans of (012) R-plane Al_2O_3 wafer planes reacted with TiF_4(g) at 310°C. In this plot, the time interval between selected scans (i.e. from the start of one scan to the start of the next scan) was 20 ± 1 seconds. In a typical run, the scans were performed over short two-theta intervals for each peak of interest to minimize the time required between two consecutive scans of each peak.

For each temperature studied, (270°C, 285°C, 310°C, 320°C, 335°C, 345°C, 360°C, and 385°C) the data corresponding to the 100% peak of $TiOF_2$ (012) was normalized to the area under the corresponding Ni reference peak fit with a Pseudo-Voigt model. A $TiOF_2$ peak area evolution plot for C-plane oriented wafers reacted between 270°C and 335°C is shown in Figure 3.10 and for R-plane oriented wafers reacted at 285°C, 310°C and 335°C is shown in Figure 3.11.

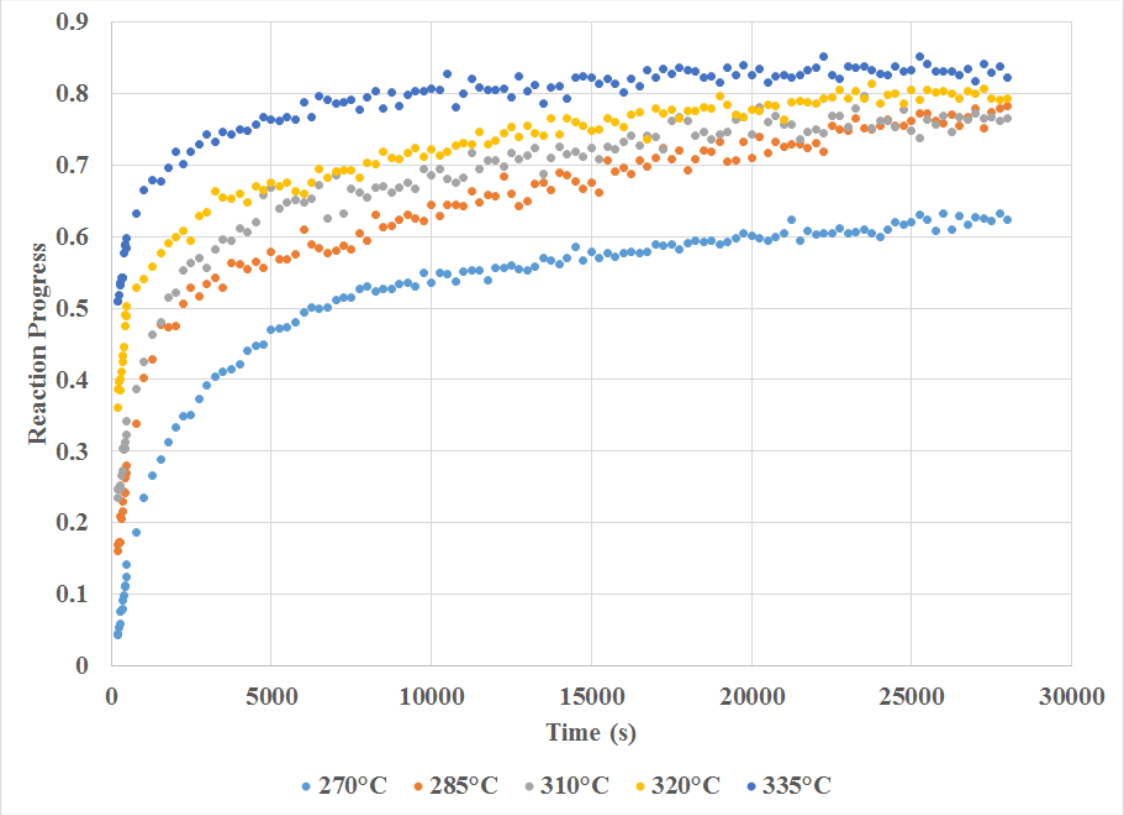

Figure 3.10. Average reaction progress of C-plane (006) Al_2O_3 wafers with TiF_4(g) at different temperatures ranging from 270°C to 335°C.

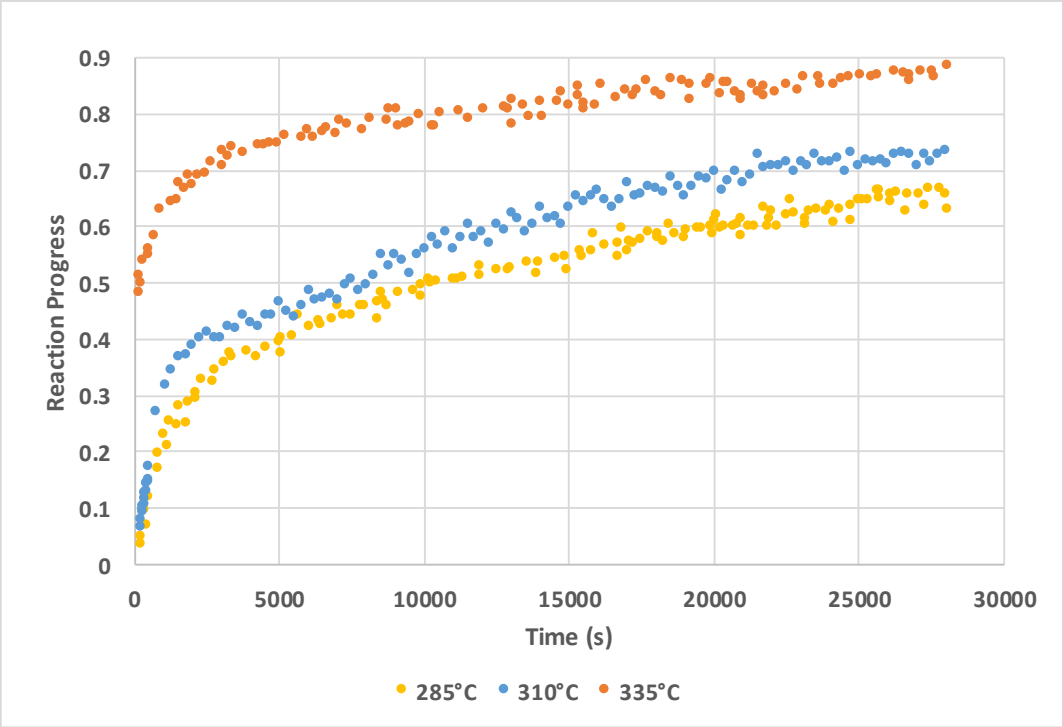

Figure 3.11. Reaction progress of R-plane (006) Al_2O_3 wafers with TiF_4(g) at different temperatures ranging including 285°C, 310°C, and 335°C.

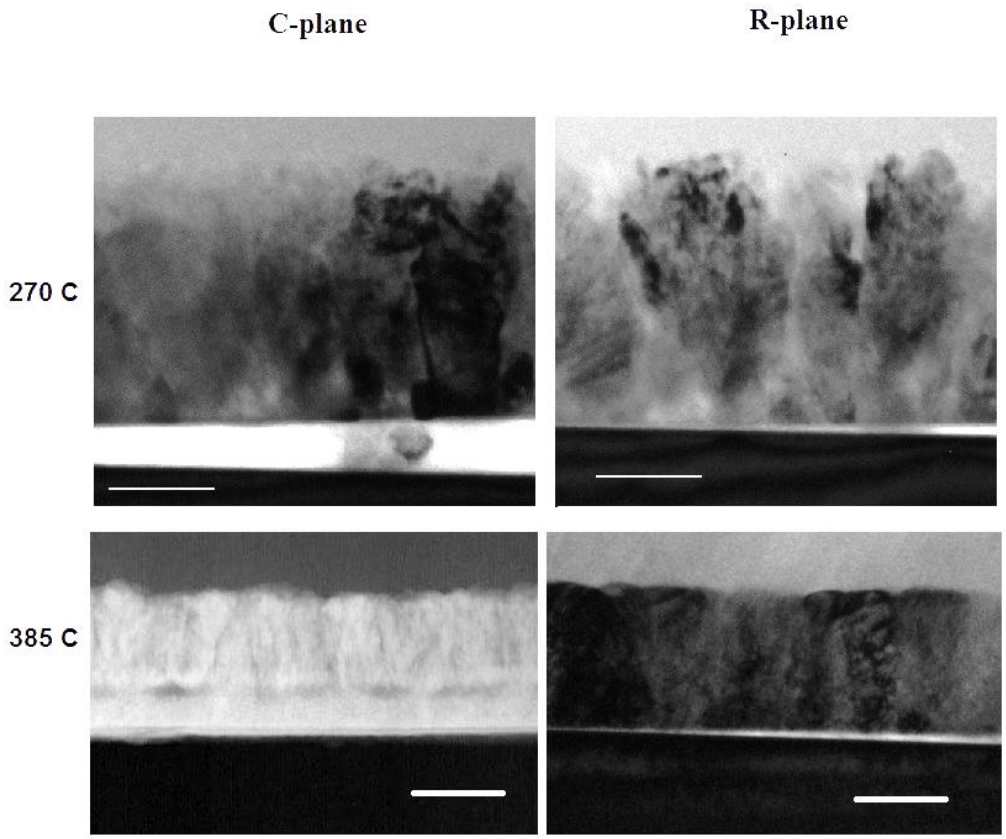

Figure 3.12. TEM images of cross-sections of substrates reacted at 270°C and 385°C for 8 h. Both C-plane and R-plane were examined. Scale bars are 100 nm for 270°C reacted samples and are 200 nm for 385°C reacted samples. The average thickness for the 270°C reacted samples were 195 nm and 202 nm for C- and R-plane specimens, respectively, and for the 385°C reacted samples were 320 and 325 nm for C- and R-plane specimens, respectively.

Each data point shown in Figures 3.10 and Figure 3.11 was the result of an individual scan. As time went by, the rate of reaction gradually decreased and became relatively constant. For example, at 270°C, the initial high rate of reaction continued until the reaction time reached about 2000 seconds, after which the slope then gradually decreased. Most of the reaction occurred during this initial kinetic regime, especially for the higher reaction temperatures.

As can be noted from the X-ray diffraction results (Figure 3.7), the aluminum byproduct of the reaction of TiF_4(g) with Al_2O_3 (i.e., AlF_3, AlOF, and/or Al_2OF_4 as per reactions (1)-(3)) was apparently amorphous. Crystallization of AlF_3 occurred in oxygen-gettered argon after 2 h at 600°C, as shown in Figure 3.13. Other analytical techniques were examined for their ability to differentiate between amorphous aluminum fluoride and amorphous aluminum oxyfluoride(s) (AlOF or Al_2OF_4) to more conclusively ensure AlF_3 was the initial by-product. For example, Time-of-Flight Secondary Ion Mass Spectroscopy (ToF-SIMS) was capable of identifying elemental and molecular species present in the product layer. A depth analysis of a C-plane sample reacted at 310ºC for 10 h revealed a distinct absence of AlO- species while there was a significant presence of TiO-, TiF-, and AlF_2- species in the product layer (see Figure 3.14). This combination of results suggested that the primary byproduct of the reaction was amorphous AlF_3, as opposed to AlOF or Al_2OF_4.

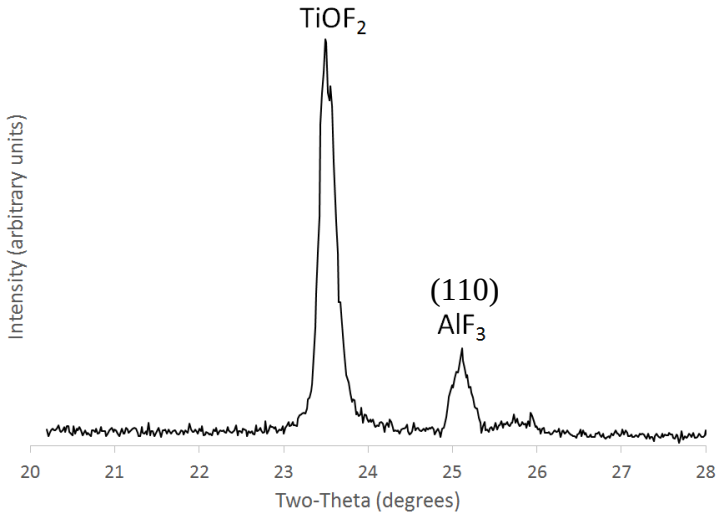

Figure 3.13. XRD of C-plane oriented wafer reacted at 310°C for 8 h and then fired in gettered argon at 600°C for 2 h. Crystalline AlF_3 ((110) peak measured is 100% AlF_3 peak) was detected along with the original $TiOF_2$ crystalline product generated at 310°C.

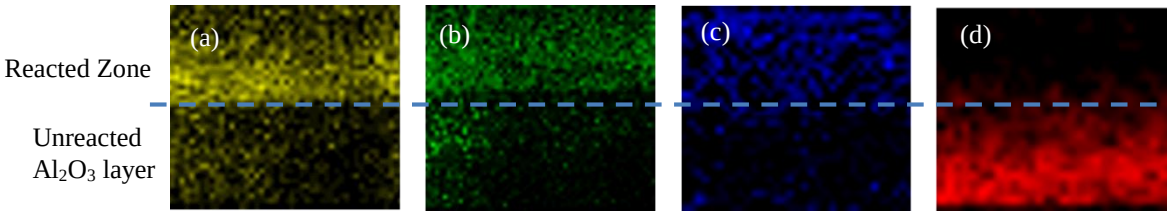

Figure 3.14. ToF-SIMS cross-sectional depth profiles reveal (a) TiF- , (b) TiO-, and (c) AlF_2- species present in the product layer while (d) AlO- existed primarily below the product layer in a C-plane wafer reacted for 10 h at 310°C.

Knowing the effective penetration depth of X-rays was critical to ensuring the accuracy of the conclusions drawn from X-ray diffraction data. This penetration depth can be calculated from the linear absorption coefficient of X-rays (a function of the mass absorption coefficient of each relevant substance) and the 2θ diffraction angle via the Beer-Lambert Law.[107] The mass absorption coefficient of a substance, μ/ρ, can be calculated

from the weight fraction, *w*, of its elements, and the mass absorption coefficients of each element in the substance.[108] For Cu Kα radiation (8.04 keV), the mass absorption coefficients of elements O, F, Al, and Ti are 11.49, 15.83, 49.75, and 200.1 cm^2/g, respectively.[109] The mass absorption coefficients of $TiOF_2$ and AlF_3 were calculated to be 98.8 cm^2/g and 19.6 cm^2/g. Using these values, the effective penetration depths of 95% of Cu Kα X-rays at $2\theta = 22°$ were calculated to be 9.3 μm and 50.7 μm through $TiOF_2$ and AlF_3, respectively. These values, which become larger at higher 2θ angles, indicated that at all times, the product layer diffraction intensities represented at least the top 9.3 μm of product. Thus, the diffracted data represents the entire product layer throughout all reaction temperatures and times, as the maximum depth of the product layer measured was always less than 0.5 μm.

3.3.2 Microstructure Evolution

Microstructural evolution was studied via TEM analyses on polished (012) R-plane and (006) C-plane Al_2O_3 wafers after reaction for various times at 310°C. The starting wafers were fully dense, single crystalline substrates (see XRD of polished surfaces in Figure 3.6). The TEM analyses (Figure 3.15) illustrated that the product layer was non-continuous in the initial stage of reaction. Within the first 10 minutes of reaction, particles ≥50 nm in size had formed on the surface of the wafers. The amount of product increased with reaction time until a continuous layer had formed across the surface of the wafer. After 30 minutes, significant growth of a continuous product layer was apparent across the entire sapphire surfaces, yet this product layer appeared to be somewhat porous. After 8 hours, the product layer appeared to be less porous. A plot of the reaction progress vs. time with markers indicating the 10 minute, 30 minute, and 8 hour time points for a C-plane wafer

reacted at 310°C is provided in Figure 3.16 for reference. The average thicknesses (over sets of 70 measurements each) of the product layer for each orientation after 30 minutes and after 8 h is available in Table 3.1. The SAED analyses confirmed the formation of crystalline $TiOF_2$ (Figure 3.17).

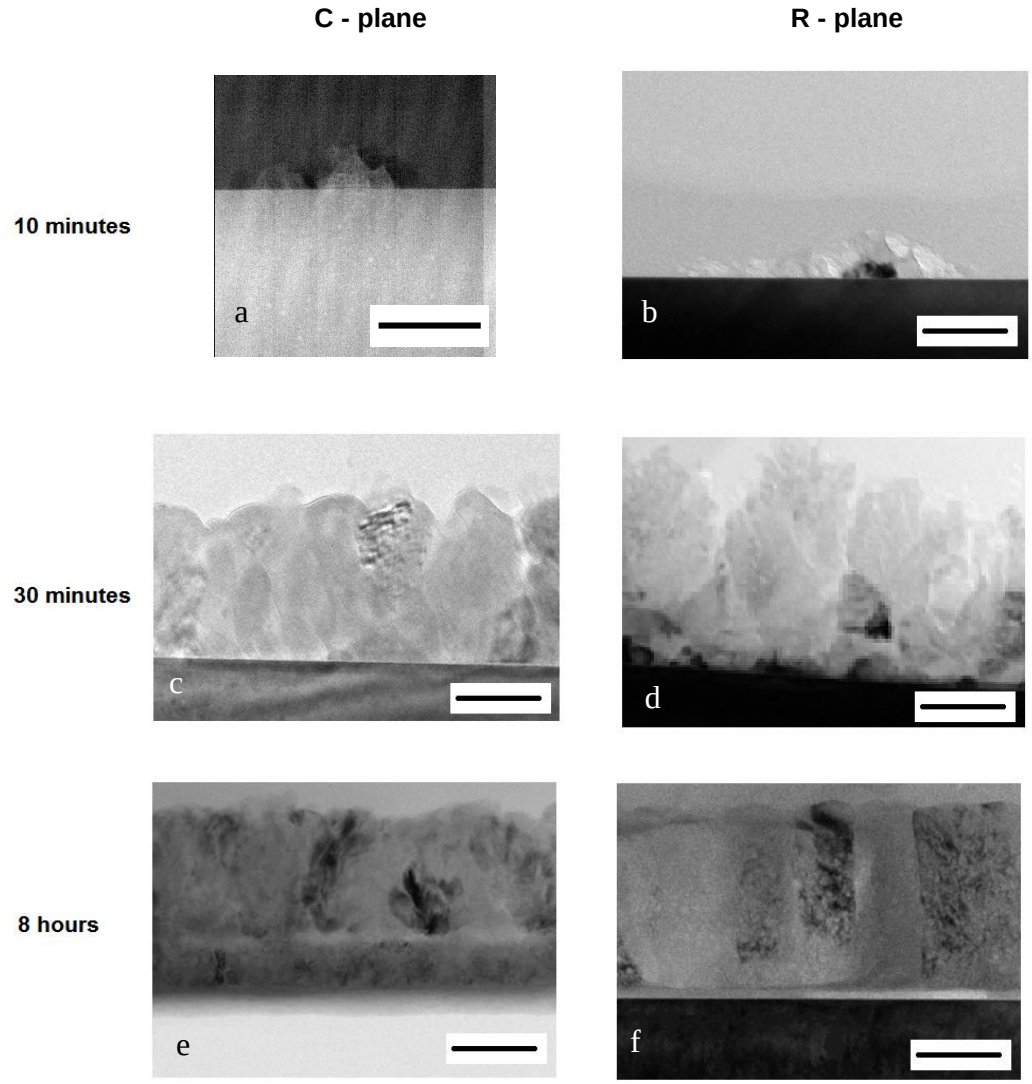

Figure 3.15. (a) STEM and (b-f) TEM images of cross-sections of reacted substrates exposed to TiF_4(g) for 10 minutes, 30 minutes, or 8 hours at 310ºC. Both C-plane and R-plane specimens were examined. All scale bars are 100 nm.

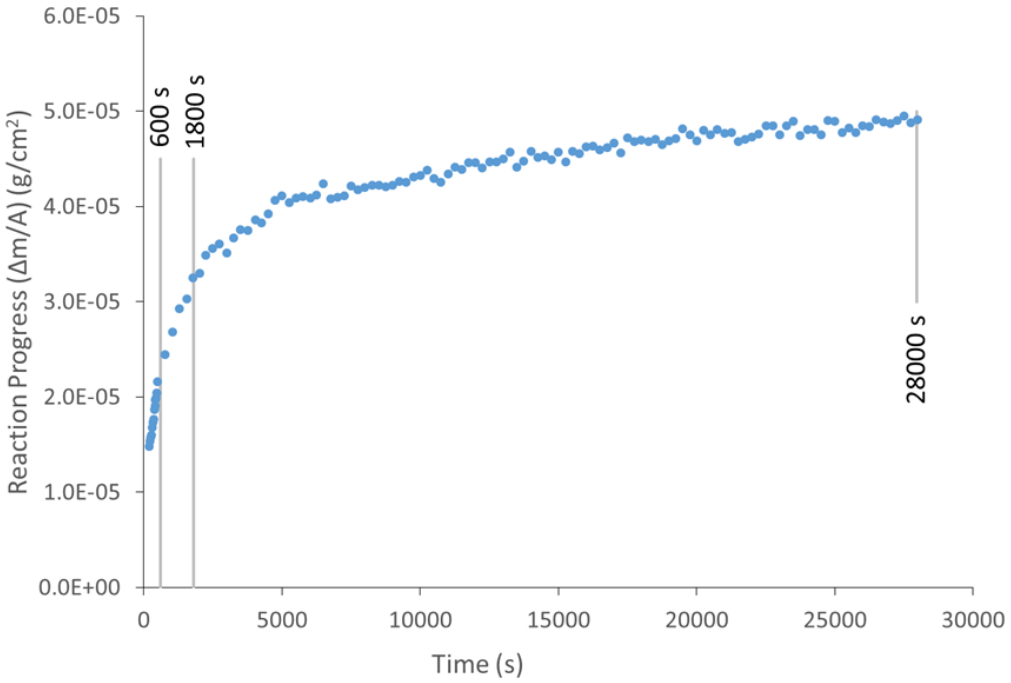

Figure 3.16. Reaction progress vs. time at 310°C for C-plane specimen with markers indicating the 10 min, 30 min, and 8 h time points.

Table 3.1. Average thickness of reacted zones after 30 minute and 8 hour reactions at 310°C for C-plane and R-plane oriented specimens.

Wafer Orientation	30 Minute Reaction		8 Hour Reaction	
	Thickness (nm)	Standard Deviation (nm)	Thickness (nm)	Standard Deviation (nm)
C-plane	197	16	249	5
R-plane	215	39	251	8

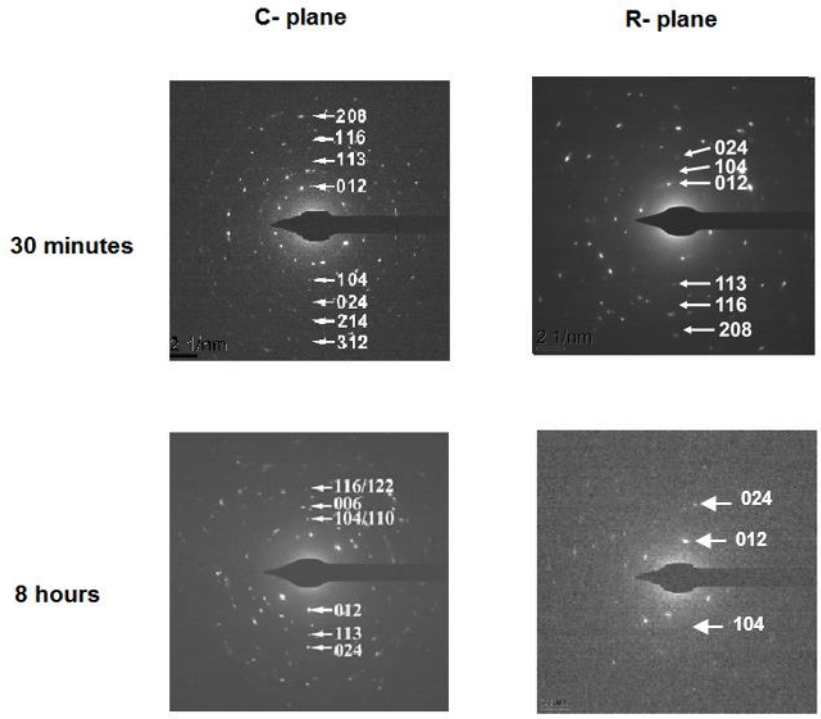

Figure 3.17. SAED analyses of reacted substrate product layers exposed to TiF_4(g) for 30 minutes or 8 hours at 310 ºC confirmed $TiOF_2$ formation. Both C-plane and R-plane specimens were examined and found to contain $TiOF_2$.

To understand the likely diffusion pathways for sustained reaction (i.e., whether pores remained for gas phase diffusion) after 6 hours of reaction at 310ºC (near the end of the reactions studied), additional microstructural characterization was performed after deposition of a 30 nm ZrO_2 layer via Atomic Layer Deposition (ALD). Because ALD techniques are capable of high-aspect-ratio deposition, it was expected that zirconium would be observed inside the product layer via EDX if significant interconnected porosity was present in the product layer during ZrO_2-precursor diffusion. As illustrated in Figure 3.18 (STEM cross-section prepared by traditional ion-milling techniques), Zr was only seen on the surface of the product layer, signifying the absence of substantial interconnected porosity in the product layer after 6 h of reaction at 310°C.

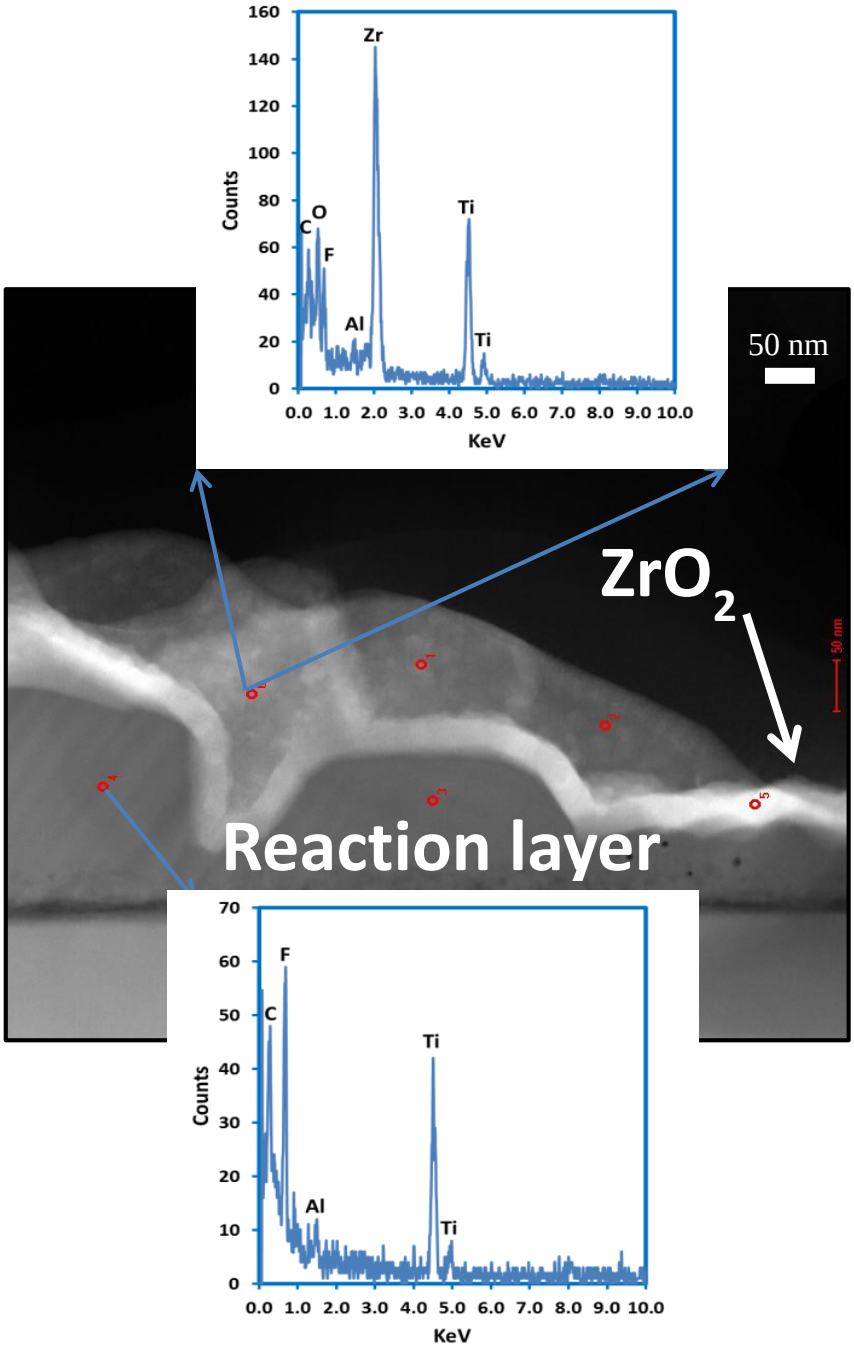

Figure 3.18. Scanning transmission electron micrograph with representative EDX patterns from different locations illustrating the absence of Zr within the product layer, and the appearance of Zr on the surface of the product layer. The sample was a C-plane sapphire oriented wafer reacted with TiF_4(g) for 6 h at 310°C before deposition of ZrO_2 via ALD.

3.3.3 Kinetic Models

Kinetic analyses and modeling can be used to understand the metathetic conversion reaction mechanism, including the rate-limiting step(s) of the TiF_4-Al_2O_3 reaction process, and to quantitatively assess of the effects of various reaction conditions. Since the mechanism and dynamics of the reaction system are interconnected, it may be possible to optimize the reaction conditions (e.g., for an enhanced rate of reaction) based on comprehension of the rate-limiting step.

Several possible kinetic models have been discussed in the literature describing non-catalytic, solid-gas reaction mechanisms. Among these are the sharp interface (shrinking core) model (SCM), the particle-pellet model, the single pore model, the distributed pore size model, and the random pore model.[8,110-113] Previous works[111,114,115] have shown the importance of using microstructural observations to evaluate the validity of a particular model. The evolution of the solid reactant and product microstructures during reaction as visualized by SEM and TEM analyses can also help discern the possible reaction mechanism(s). Due to its versatility, applicability to several reacting gas-solid systems, and simplicity, the SCM has been used by many authors.[8,114,116-118]

In the SCM, a distinct interface must exist between a solid reactant and solid product, which is consistent with the TEM images shown in Figure 3.15 of the TiF_4/Al_2O_3 reaction studied here. At this interface, a thinning solid reactant exposed to a gas becomes covered by a thickening product layer. Accordingly, the overall rate at which the product layer develops can be limited by one or more of the following processes: gas phase mass transfer, diffusion through solid layers, or chemical reaction at an interface.

3.3.3.1 Modeling of HTXRD Kinetic Data

Based on the microstructural evolution previously discussed, the kinetic mechanism controlling the reaction seems to change with time. The kinetic rate was fast during early $TiOF_2$ product layer formation on the surface of the substrate but slowed when a different apparent kinetic mechanism became rate-limiting. This mechanistic shift was made apparent by the inability to fit the HTXRD data (for 310°C reacted samples) over the entire reaction time with a single shrinking core model equation as illustrated in Figure 3.19(a) for a C-plane wafer. The reaction progress has been scaled to indicate the change in mass per unit area for the sample based on the resulting thickness of the product and density of $TiOF_2$. To accomplish this, the reaction progress was scaled to the approximate reacted layer thickness associated with the given time and temperature (e.g. If full reaction is considered to be a reacted layer that is 320 nm thick, then a reaction progress of 0.78 is equivalent to a reacted layer that is approximately 250 nm thick.). Given the densities of $TiOF_2$ and AlF_3 (crystalline) are 3.12 g/cm^3 and 2.88 g/cm^3 respectively (powder diffraction files (PDF) 59-0871, 47-1659), the approximate thickness of $TiOF_2$ in the reacted layer is 63% of the total thickness based on 2 mol of AlF_3 forming for every 3 mol of $TiOF_2$. Converting the approximate thickness of $TiOF_2$ into centimeters and multiplying by the density of $TiOF_2$ yields reaction progress in terms of mass per unit area (g/cm^2) where the area term is the surface area of reaction upon which the thickness, or mass, grows.

The correlation coefficients in both single mechanistic cases are poor (R^2 = 0.669 and 0.699 for a linear fit and a parabolic (square root function) fit, respectively). A plot of these fits (**Error! Reference source not found.**(b), the yellow dashed curve and green

dashed curve represent the linear and parabolic best fit functions, respectively) and the original data (black dots) on a log-log scale reveals that they do not adequately match the data.

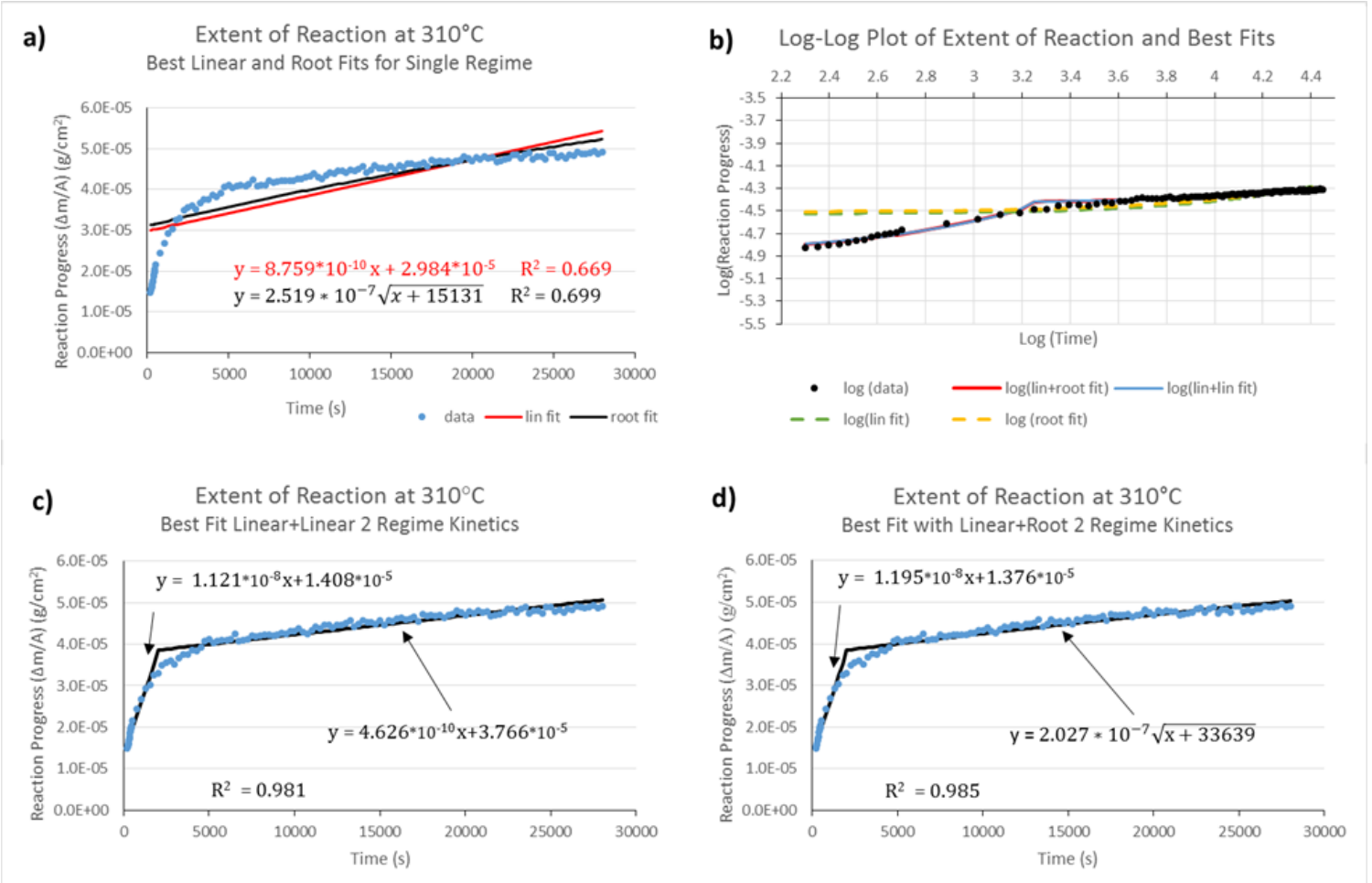

Figure 3.19. Reaction progress vs. time at 310°C on C-plane wafer plotted and shown as a single regime (a) with the best fit linear (red) and parabolic (square root) (black) functions. The data is then plotted with two distinct linear regimes (c) and two distinct (first linear then parabolic) regimes (d). The logarithms of each of these best fits is also plotted with the logarithm of the original data in (b).

As discussed in the following sections, dividing the data into two distinct kinetic regimes (as shown in Figure 3.19(c) and (d) and Figure 3.20) results in significantly higher correlation coefficients on linear axes (C-plane wafer: R^2 = 0.981 and 0.985 for two linear regimes and a linear followed by a parabolic regime, respectively; R-plane wafer: R^2 = 0.977 and 0.988 for two linear regimes and a linear followed by a parabolic regime, respectively) and better correlation with the best fit functions when plotted on logarithmic scale axes.

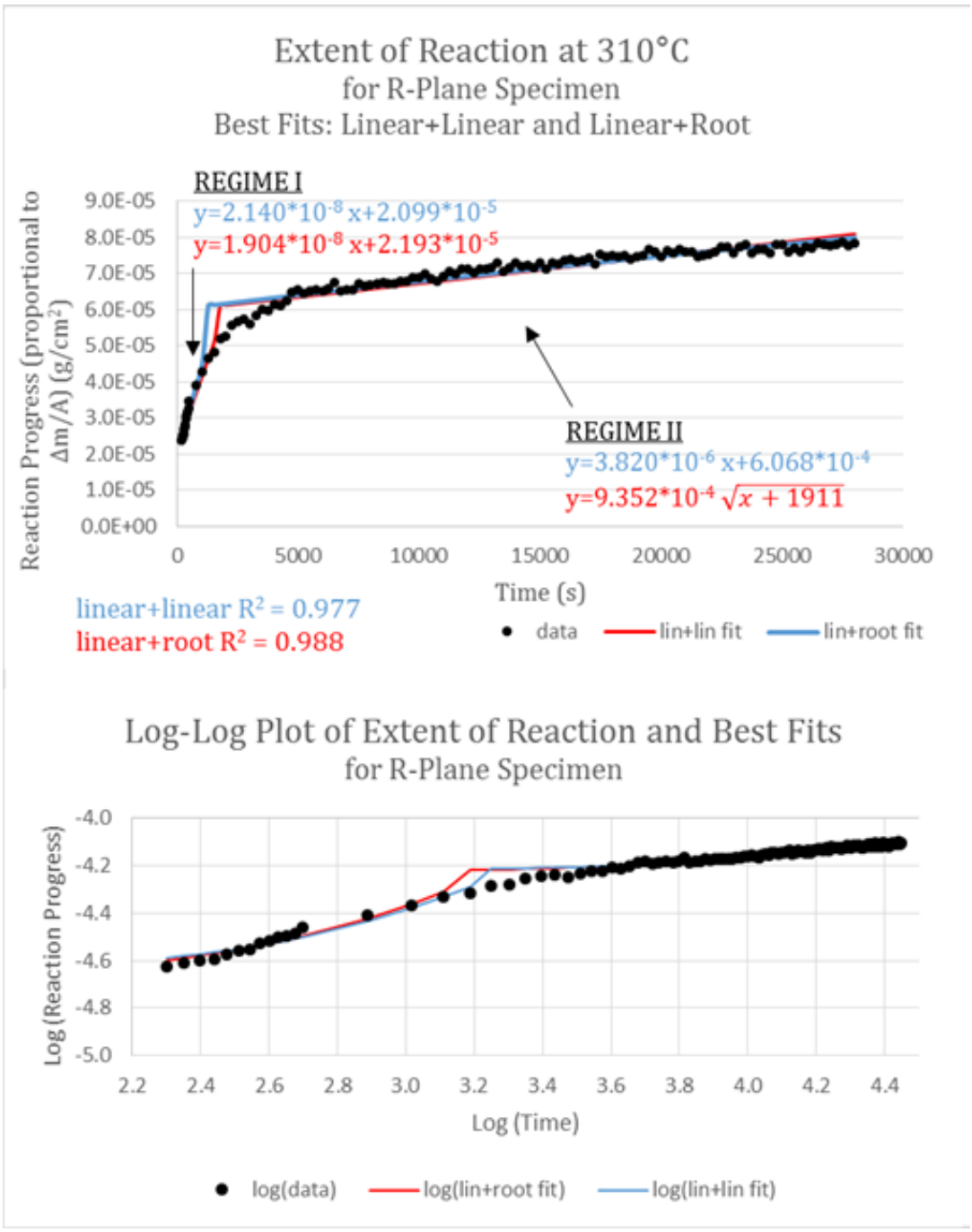

Figure 3.20. Reaction progress vs. time at 310°C on R-plane wafer plotted and shown with two dual regime fits (top image): the two linear regime best fit (blue) and a linear followed by parabolic function best fit (red). The best fit functions and the combined correlation coefficient for each pair of fits is provided. The logarithms of each of these best fits is also plotted with the logarithm of the original data (bottom image).

Deciding on a point in time during reaction when the kinetic mechanism shifted from an initial regime to a unique second regime was not obvious or arbitrary as there is likely a transitional time between the two kinetic regimes. Because the product layer was non-continuous in the first 10 minutes of reaction, it was unlikely that the kinetic mechanism would change during this time. Therefore, the second regime is unlikely to start before 10 minutes of reaction. Because no continuous layer was noticed in the first 10 minutes of reaction but may have formed at any point before 30 minutes of reaction were completed (as determined by the microstructural evolution in Figure 3.15), Kinetic Regime I was expected to end between these two times.

As a first-order attempt to establish the likely kinetic mechanisms, the transitional period between kinetic mechanisms was ignored. For each potential pair of kinetic mechanisms, a brute force search was performed for a single transition point in time that maximized the overall R^2 of the combined model. These optimized regimes were compared to the expected regime limits. As will be discussed, the initial regime had to be linear as the product layer was non-continuous in at least the first 10 minutes of reaction (see Figure 3.15), and the second regime may have been linear (Figure 3.19(c)) or follow a parabolic function (Figure 3.19(d)).

3.3.3.2 Kinetic Regime I

Data in the initial kinetic regime, Kinetic Regime I, was fit with two possible kinetic models representing the three different rate controlling mechanisms according to the shrinking core model for a flat plate geometry. While the lower bound for data in this regime was the first data point collected, the upper bound was selected based on the microstructural evolution plot in Figure 3.15, independent of the starting point for Kinetic

Regime II (the data in Figure 3.19 contains bounds determined by optimization of fitting of two regimes). Because no continuous layer was noticed in the first 10 minutes of reaction but may have formed at any point before 30 minutes of reaction were completed, Kinetic Regime I was evaluated using all scans up to the 10 minute mark (note: after 500 seconds, scan time was increased resulting in no scans between 500-600 seconds).

The three possible mechanisms that could control the first kinetic regime, per the SCM, are: chemical reaction control and gaseous phase mass transfer (with linear growth over time), and solid state diffusion (with parabolic (square root) growth over time). Figure 3.21 shows fits of the extent of reaction data at 310°C on both C-plane and R-plane samples. While both the linear and parabolic models fit the C-plane wafer reasonably well ($R^2 = 0.990$ and $R^2 = 0.983$), the linear model was a much better fit for the R-plane wafer ($R^2 = 0.977$ vs. $R^2 = 0.950$ for the parabolic model), suggesting that the first kinetic regime was controlled by either chemical reaction or gas diffusion control.

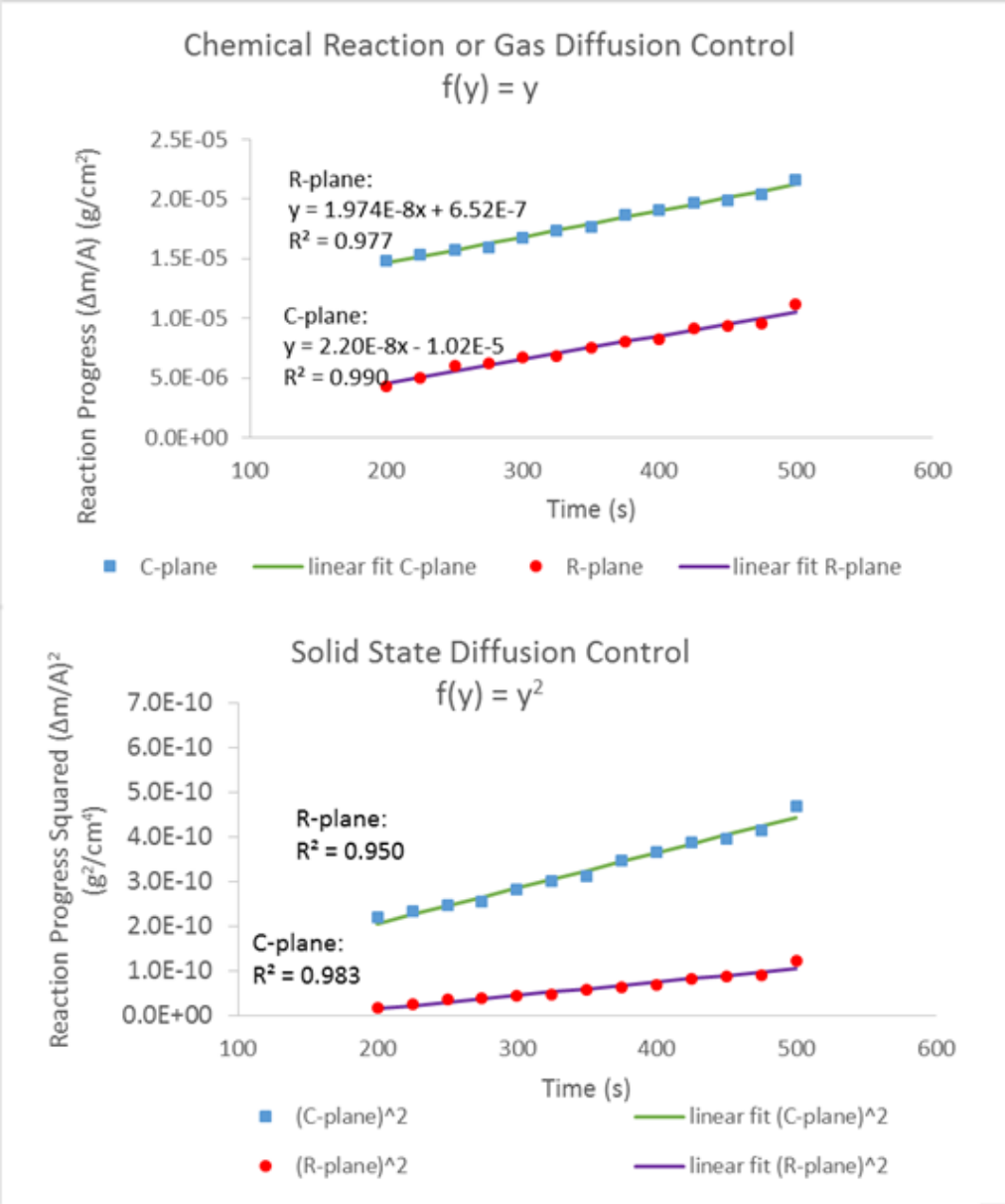

Figure 3.21. Fits of the extent of reaction data in Kinetic Regime I at 310°C comparing R-plane and C-plane orientations to two possible models for different rate controlling mechanisms.

Solid state diffusion control was also deprecated by the microstructural evidence shown in Figure 3.15. As previously shown by the microstructural evolution, there was no indication of a dense, continuous product layer on the surface of the substrate during the

first 10 minutes, thus a relatively slow solid state diffusion path would have been bypassed by a much faster gas phase diffusion path.

If bulk gas phase diffusion was rate limiting, depletion of the gaseous reactant at the specimen surface during the reaction would have been relatively fast, resulting in a gradient of the reacting gas species concentration around the reacting substrate. In order to test the potential for gas phase diffusion control to kinetic rate, the gas phase diffusion distance during HTXRD analyses was varied from approximately 2 mm to 14 mm (thus creating a variation in the gas concentration gradient and thus a variation in the gas flux). Figure 3.22 illustrates that no apparent variation in kinetics was seen as a function of bulk gaseous diffusion distance.

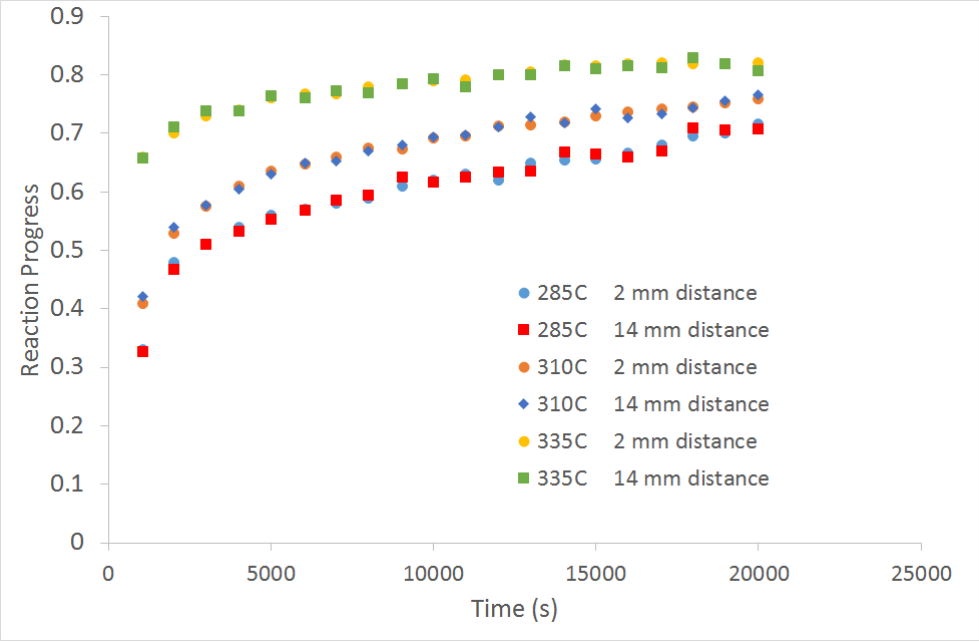

Figure 3.22. Reaction progress vs. gaseous diffusion distance for C-plane specimens at different temperatures.

Additionally, following the method described by Welty[119] and implemented for TiF_4(g) in Ar(g) by Shian,[10] the diffusion coefficient for TiF_4(g) in Ar(g) was calculated to be 3.3×10^{-5} m^2/s at 310°C (See Appendix A for calculation). In the case of a regular shape such as a plate, the mass transfer coefficient, k_g, is related to the gas diffusion coefficient, D_g, by the expression[120]:

$$Sh = \frac{k_g L}{D_g}$$

Where *Sh* is the Sherwood number and is equal to 2 for a system with no forced convention[119], and *L* is the characteristic length. For this system, if the characteristic length is defined as 2 mm, the resulting mass transfer coefficient would be equivalent to:

$$k_g = \frac{Sh\, D_g}{L} = \frac{2 \times 3.3 \times 10^{-5}}{0.002} = 0.033 \frac{\text{m}}{\text{s}}$$

If this were the rate limiting step, we could expect to fully react a 1 mm thick sample in under 40 ms or create a 250 nm product zone in 7600 ns:

$$0.033 \frac{\text{m}}{\text{s}} \times 0.040 \text{ s} = \ 0.0013 \text{ m} = 1.3 \text{ mm}$$

$$0.033 \frac{\text{m}}{\text{s}} \times 7600 \times 10^{-9} \text{ s} = \ 2.5 \ \times 10^{-7} \text{m} = 250 \text{ nm}$$

Considering that a product layer of 250 nm took approximately 30 minutes to form, one can conclude that the gas phase diffusion between the Al_2O_3 reactant wafer and the TiF_4 gas source was not the rate limiting step for the conditions used in this experiment.

As both solid state diffusion and bulk gas diffusion were ruled out, chemical reaction control was ruled to be most likely mechanism controlling the initial reaction kinetics seen

in Kinetic Regime I. However, chemical reaction may be controlled by several different factors including adsorption of the reactants to the interface, surface diffusion of the reactants, the surface reaction, or desorption of the products. The exact method of chemical reaction control in the first kinetic regime has not been established here. Had significant variations in reaction with the varying Al_2O_3 crystalline planes been observed, a more noteworthy correlation between the chemical reaction control and kinetics might be possible. As visible in the microstructural evolution graphics, the differences between product thicknesses between different orientations was negligible. This suggests that reaction at the product/gas interface could be controlling the rate. As can be seen in Figure 3.10, an increase in reaction temperature resulted in a decrease in the time required to complete reaction in Kinetic Regime I. This temperature trend was consistent across different orientations of reactant Al_2O_3 wafers.

3.3.3.3 Kinetic Regime II

Using SCM, the boundaries of Kinetic Regime II were found via brute force optimization of a two function fit to the data. Due to the results of the previous section, a linear function for Kinetic Regime I was assumed, while Kinetic Regime II was modeled using both a linear and parabolic fit. The best fit pairs of functions (linear + linear or linear + parabolic) for C-plane samples reacted at 310°C can be seen in Figure 3.19(c) and (d), and the results (correlation coefficients) of the brute force optimization for all points between 10 minutes and 30 minutes of reaction are shown in Table 3.2. If both regimes were linear, the overall best fit for the second regime (assuming no transitional period) occurred when Kinetic Regime II began between 10 and 30 minutes into reaction, with the correlation to this combined mechanistic fit resulting in $R^2 = 0.981$ at approximately 25

minutes. If the second regime was assumed to be a parabolic function, the optimized best fit for the pair of fit functions found the second regime to begin at approximately 25 minutes, also, and resulted in a thermogravimetric rate constant on the order of 4×10^{-14} g^2/cm^4s as derived from the data. The resulting correlation coefficient of this pair of functions was slightly higher. $R^2 = 0.985$, suggesting that a process with parabolic growth was slightly more likely to be the rate limiting mechanism.

Table 3.2 Correlation coefficients resulting from a brute force optimization of a two function fit to the C-plane data at 310°C at times between 10 and 30 minutes.

Starting time for first scan time contributed to Kinetic Regime II	Correlation Coefficient (R^2) assuming Kinetic Regimes I and II are linear and parabolic, respectively	Correlation Coefficient (R^2) assuming Kinetic Regimes I and II are both linear
756 s	0.950	0.925
1012 s	0.967	0.944
1268 s	0.977	0.946
1524 s	**0.985**	**0.981**
1780 s	0.980	0.978

During Kinetic Regime II, the reaction rate was significantly slowed compared to the first regime. Because a difference in reaction progress as a function of bulk gas-phase diffusion distance was not found, as shown in Figure 3.22, and the expected reaction coefficient for gas-phase diffusion significantly exceeded the rate of reaction in the first regime, bulk gas phase diffusion could not be rate-limiting in the second regime.

The slower reaction rate did not rule out a slow chemical reaction (limited by at

least one of the adsorption, surface diffusion, surface reaction, or desorption steps) as the rate limiting mechanism. This could have been a reaction at the interface between the Al_2O_3 and the product layer (which could have a different rate than the chemical reaction control at the gas/Al_2O_3 interface seen in Kinetic Regime I) or at the product layer interface with the gas. Little difference was found in Kinetic Regime II for the C-plane and R-plane wafers, as illustrated by their similar linear fits in Figure 3.19 and Figure 3.20, suggesting chemical reaction control at the Al_2O_3/product interface was unlikely to be rate-limiting.

Although the exact porosity or density of the product layer was unknown, either solid state diffusion, or slowed gaseous diffusion through small but interconnected pores, in the product layer could control the second regime kinetics, as the growing product could slow mass transport to the reaction site. Based on microstructural observation during Kinetic Regime II (see Figure 3.15), there was a continuous solid product layer on the surface of the substrate. This layer may have acted as a diffusion barrier, slowing reactant transport. This mass transport barrier may have acted as a rate controlling mechanism (via slow solid-state diffusion or slowed gaseous diffusion through interconnected pores). While calculations of molecular diffusion through the lattice can be complicated by grain boundaries and dislocations, porous diffusion can be equally complex to calculate. However, as illustrated in Figure 3.18, significant porous pathways for diffusion were not apparent in the product layer after 6 h at 310°C. This strongly suggests that should diffusion be controlling Kinetic Regime II, the diffusion was likely through the solid-state.

The expected parabolic rate constant k_p can be approximated using the Wagner theory for simultaneous scale formation and gas diffusion through an oxide scale (credited to Wagner[121] by Jost[122]). This method was originally employed to determine the rate at

which a binary alloy was penetrated by dissolved oxygen as it internally reacted with the more reactive alloy component to form a precipitate, but is generally applicable to other simultaneous scale formation and diffusion processes. The figure below illustrates the expected parabolic behavior through the growing oxide scale.

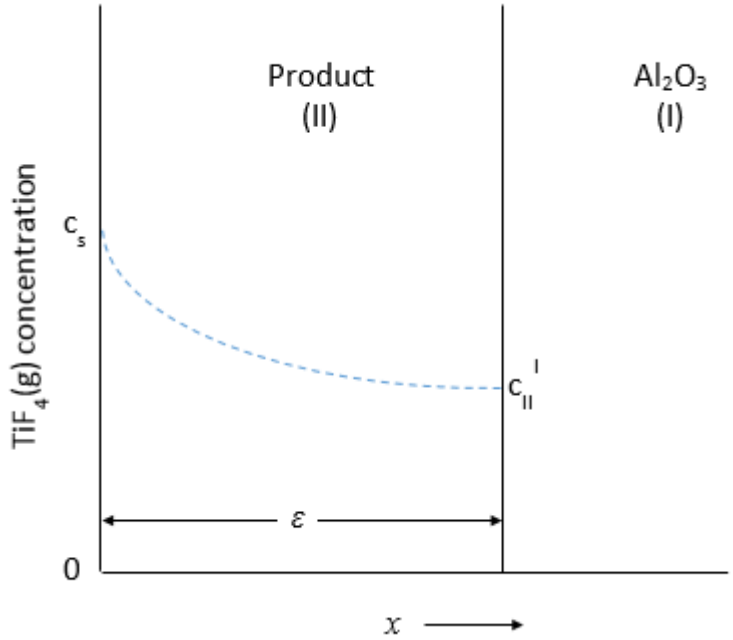

Figure 3.23. Schematic illustrating the concentration gradient of TiF_4(g) through a growing product layer.

To use this model, we must first make a few assumptions including:

1) The product scale is of uniform thickness, ε, at any given time and completely adherent to the underlying Al_2O_3 surface
2) Growth of oxide is controlled by inward diffusion of TiF_4(g) through the oxide lattice so that new oxide only forms at the oxide/Al_2O_3 interface.
3) The underlying phase (Al_2O_3) is planar, semi-infinite, and impenetrable to the diffusing gas.

Fick's Second law predicts how diffusion causes the concentration of a species to change with position and time, that is:

$$\frac{\partial c_{TiF4}}{\partial t} = D^{II}_{TiF4} \frac{\partial^2 c_{TiF4}}{\partial x^2} \; for \; 0 < x < \varepsilon \qquad (1)$$

Where c_{TiF4} is the concentration of diffusing gas TiF_4, t is time, D^{II}_{TiF4} is the diffusion coefficient of TiF_4 in the oxide layer (*II*), and ε is the position of the oxide/ Al_2O_3 interface. D^{II}_{TiF4} is assumed to be independent of the concentration in the above equation.

To solve Fick's Second law, initial and boundary conditions were chosen as follows:

$$c_{TiF4} = 0 \text{ at } x > 0, t = 0 \qquad (2a)$$

$$c_{TiF4} = c_s \text{ at } x = 0, t > 0 \qquad (2b)$$

$$c_{TiF4} = c_{II}{}^{I} \text{ at } x = \varepsilon_-, t > 0 \qquad (2c)$$

$$c_{TiF4} = 0 \text{ at } x = \varepsilon_+, t > 0 \qquad (2d)$$

where $x = 0$ refers to the position of the oxide/gas interface (relative to the surface of the oxide) and $x = \varepsilon_-$ and $x = \varepsilon_+$ refer to positions just within the oxide scale and just within Al_2O_3 at the oxide/Al_2O_3 interface, respectively.

We consider an infinitesimal inward displacement, $d\varepsilon$, of the oxide/Al_2O_3 interface in time dt due to the formation of new oxide, where:

1) Prior to this displacement, the TiF_4 concentration at the position ε_+ is zero.
2) If the oxide/Al_2O_3 interface is considered to infinitesimally thin, then after the

interface moves inward a distance of $d\varepsilon$, the TiF_4 concentration at this position changes to $c_{II}{}^{I}$

This increase in concentration of TiF_4 has to be accommodated by the flux of TiF_4 toward the oxide/Al_2O_3 interface. That is:

$$c_{II}^{I}\frac{d\varepsilon}{dt} = -D_{TiF4}^{II}\frac{\partial c_{TiF4}}{\partial x}\Big|_{\varepsilon_-} \qquad (3)$$

A solution to Fick's second law within the oxide scale that satisfies the boundary condition in (2b) is:

$$c_{TiF4} = c_s - B_{II}\left\{erf\left[\frac{x}{2\sqrt{D_{TiF4}^{II}t}}\right]\right\} \qquad (4a)$$

$$\text{or} \quad \frac{\partial c_{TiF4}}{\partial x}\Big|_{\varepsilon_-} = \left.\frac{-B_{II}exp\left[\frac{-x^2}{4D_{TiF4}^{II}t}\right]}{\sqrt{\pi D_{TiF4}^{II}t}}\right|_{\varepsilon_-} \qquad (4b)$$

Application of boundary condition (2c) to equation (4a) yields:

$$c_{II}^{I} = c_s - B_{II}\left\{erf\left[\frac{\varepsilon}{2\sqrt{D_{TiF4}^{II}t}}\right]\right\} \qquad (4c)$$

Substituting (4b) into (3) yields:

$$c_{II}^{I}\frac{d\varepsilon}{dt} = -D_{TiF4}^{II}\left.\frac{-B_{II}exp\left[\frac{-x^2}{4D_{TiF4}^{II}t}\right]}{\sqrt{\pi D_{TiF4}^{II}t}}\right|_{\varepsilon_-} \qquad (5a)$$

or more simply:

$$c_{II}^{I}\frac{d\varepsilon}{dt} = B_{II}\sqrt{\frac{D_{TiF4}^{II}}{\pi t}}exp\left[-\frac{\varepsilon^2}{4D_{TiF4}^{II}t}\right] \qquad (5b)$$

Since the formation of new oxide scale is determined by the flux of TiF_4(g) molecules through the thickening scale, then the scale is expected to grow at a parabolic rate:

$$\varepsilon = \sqrt{2k_p t} \qquad (6a)$$

Here we introduce a constant, γ, such that:

$$\varepsilon = 2\gamma\sqrt{D_{TiF4}^{II}t} \qquad (6b)$$

or:

$$\frac{d\varepsilon}{dt} = \gamma\sqrt{\frac{D_{TiF4}^{II}}{t}} \qquad (6c)$$

where:

$$\gamma = \sqrt{\frac{k_p}{2D_{TiF4}^{II}}} \qquad (6d)$$

Substituting equations (6b) and (6c) into equation (5b) yields:

$$c_{II}^{I} = \frac{B_{II}}{\gamma\sqrt{\pi}}\ exp[-\gamma^2] \qquad (7a)$$

Combining (4c) and (6b) and solving for B_{II} we get:

$$B_{II} = \frac{c_s - c_{II}^{I}}{erf(\gamma)} \qquad (7b)$$

Substituting (7b) into (7a) yields:

$$c_{II}^{I} = \frac{(c_s - c_{II}^{I})exp(-\gamma^2)}{\gamma\sqrt{\pi}[erf(\gamma)]} \qquad (8)$$

If c_{II}^{I}, c_s, and D_{TiF4}^{II} are known, we can iteratively solve (8) for the constant γ and the rate constant k_p. D_{TiF4}^{II}, as a first approximation is taken as equal to the bulk diffusion coefficient of TiF_4(g) in Ar. Others have previously calculated this to be 2.6 x 10^{-5} m^2/s at 230°C.[10] c_s can be approximated for any given temperature assuming TiF_4(g) behaves ideally, and the pressure of TiF_4(g) is equal to its vapor pressure. At 310°C, c_s =49.0 mol/m^3 (found using $c_s = P/RT$ where P_{TiF_4} (310°C) = 238 kPa).[67] c_θ is calculated from the reaction equation:

$$3TiF_4(g) + Al_2O_3(s) \rightarrow 3TiOF_2(s) + 2AlF_3(s)$$

Knowing the molar ratios of reactants and products, and the molar masses and densities of the products, we calculated that for every 3 moles of TiF_4 reacted, approximately 152 cm^3 of product is formed (powder diffraction files 47-1659 and 07-5087). That is, there are 19737 mol TiF_4 consumed per cubic meter of product produced. Theoretical calculation of c_{II}^{I} (a concentration in mol/vol) is slightly more complex but is calculated as follows:

Assuming TiF_4(g) is ideal, we can say:

$$P = c_{II}^{I}\mathrm{RT} \qquad (9)$$

For the chemical reaction above,

$$\Delta G_{rxn}^{\circ} = -RT\ln K \quad \text{where } K = \frac{1}{P_{TiF4(g)}^{3}} \qquad (10)$$

Plugging (9) into (10) we get:

$$\Delta G^{\circ}_{rxn} = -RT \ln\left[\frac{1}{(c_{II}^{I}\mathrm{RT})^{3}}\right] \quad (11)$$

Rearranging to solve for c_{II}^{I}:

$$c_{II}^{I} = \frac{1}{RT}\exp\left[\frac{\Delta G^{\circ}}{RT}\right]^{1/3} \quad (12)$$

From Hess's Law:

$$\Delta G^{\circ}_{rxn} = 3\Delta_f G^{\circ}_{TiOF2} + 2\Delta_f G^{\circ}_{AlF3} - 3\Delta_f G^{\circ}_{TiF4(g)} - \Delta_f G^{\circ}_{Al2O3} \quad (13)$$

Combining (12) and (13) and solving for c_{II}^{I}, we get:

$$c_{II}^{I} = \frac{1}{RT}\left[exp\left(-\frac{3\Delta_f G^{\circ}_{TiOF_2} + 2\Delta_f G^{\circ}_{AlF3} - 3\Delta_f G^{\circ}_{TiF4(g)} - \Delta_f G^{\circ}_{Al2O3}}{RT}\right)\right]^{-1/3} \quad (14)$$

Interpolating data from the NIST-JANAF Thermochemical Tables[123] for Gibbs Free Energy of the formation of reactants and products, we obtained the following information:

$$\Delta_f G^{\circ}_{TiF4(g)} @\ 310°C = -1480.54 * 10^3 J/mol$$

$$\Delta_f G^{\circ}_{Al2O3}\ (alpha\ phase) @\ 310°C = -1492.61 * 10^3 J/mol$$

$$\Delta_f G^{\circ}_{AlF3}(crystalline) @\ 310°C = -1356.34 * 10^3 J/mol$$

No information is available in the literature on experimental values for Gibbs Free Energy of Formation of $TiOF_2$(s). Reports have shown $TiOF_2$ decomposes directly into TiO_2 and TiF_4 in a dry atmosphere with the decomposition beginning near 150-200°C and completing by 500°C.[124] A report on related materials including $ZrOF_2$ and $HfOF_2$

suggested that approximations of thermodynamic data may be estimated from linear interpolation of enthalpy plotted versus the number of ligands.[125] Drawing from this, a rough first approximation of the free energy of formation of $TiOF_2$ might be linearly interpolated between that of TiO_2 and TiF_4 at a given temperature. Via interpolation of values in the NIST JANAF data tables[123], the Gibbs Free Energy of Formation of TiO_2 (anatase) at 310°C is -830.8 kJ/mol. A linear interpolation between this data point and the Gibbs Free Energy of Formation for TiF_4 (listed above as -1480.54 kJ/mol) yields an approximate value for the Gibbs Free Energy of Formation of $TiOF_2$ of -1156 kJ/mol. Another estimation of the Gibbs Free Energy of Formation of $TiOF_2$ can be made through linear extrapolation of the Gibbs Free Energy of Formation of other known Group 4 metal oxyfluorides including $ZrOF_2$ and $HfOF_2$. From enthalpy and entropy data on $ZrOF_2$ and $HfOF_2$,[125] their respective Gibbs Free Energy of Formation at 310°C were found to be -2614 kJ/mol and -2590 kJ/mol. Extrapolating across the three different periods (the periods for Ti, Zr, and Hf are 4, 5, and 6 respectively), results in an approximate value for $\Delta_f G^\circ_{TiOF2}$ of -2638 kJ/mol. These values fit within the known upper bound of $\Delta_f G^\circ_{TiOF2}$ for this system: given the $\Delta_f G^\circ$ above, we can calculate a maximum value of $\Delta_f G^\circ_{TiOF2}$ because we know that c_{II}^I must not be greater than c_s. If $c_{II}^I = c_s$, then $\Delta_f G^\circ_{TiOF2}$ would be at its maximum value of approximately -1097 kJ/mol. Were this the case, k_p would reach its minimum limit of zero. If $\Delta_f G^\circ_{TiOF2}$ is approximately -1156 kJ/mol or -2638 kJ/mol, then k_p would approach a value of 6.5×10^{-8} m^2/s or 4.4×10^{-9} m^2/s, respectively, its maximum possible values.

The parabolic rate constant, k_p, can be correlated with the thermogravimetric rate constant, k_g, via the equation:

$$k_g = 2k_p \left(\frac{MW_2}{|Z_2|V_{eq}}\right)^2,$$

where MW_2 is the atomic or molecular weight of the diffusing species, $|Z_2|$ is the number of electrons involved in the reaction (here, we've assumed 6 electrons involved in the reaction of 1 equivalent of Al_2O_3), and V_{eq} is the equivalent volume of product formed from 1 equivalent of Al_2O_3. As a first approximation, we assumed $TiOF_2$ and AlF_3 products are fully crystalline, and thus 1.56×10^{-4} m^3 of product forms per mole of Al_2O_3 reacted. Hence, for TiF_4 (molecular weight = 123.861 g/mol) diffusion through the product layer, the upper limits on the parabolic rate maximum of 6.5×10^{-8} m^2/s or 4.4×10^{-9} m^2/s would be equivalent to a maximum thermogravimetric rate constant of 2.3×10^{-5} $g^2/(cm^4 s)$ or 1.5×10^{-6} $g^2/(cm^4 s)$, respectively:

$$k_g = 2(6.5 \times 10^{-8}\, m^2/s)\left(\frac{123.681\, g/mol}{6 \times 1.56 \times 10^{-4} m^3/mol}\right)^2 \times (0.01\, m/cm)^4 = 2.3 \times 10^{-5} g^2/(cm^4 s)$$

or,

$$k_g = 2(4.4 \times 10^{-9}\, m^2/s)\left(\frac{123.681\, g/mol}{6 \times 1.56 \times 10^{-4} m^3/mol}\right)^2 \times (0.01\, m/cm)^4 = 1.5 \times 10^{-6} g^2/(cm^4 s)$$

We would expect this derived thermogravimetric rate constant value to be higher than the experimental value found using the shrinking core model (4×10^{-14} $g^2/cm^4 s$) as it is a maximum rate constant value, which is what we saw.

3.4 Conclusions

HTXRD, SEM, TEM, and ToF-SIMS analyses were used to examine the rate of conversion of Al_2O_3 wafers into $TiOF_2$ via reaction with TiF_4(g) at 270-335°C. ToF-SIMS

analyses suggested that a second product of reaction was likely AlF_3. HTXRD and TEM microstructural analyses suggested that the reaction kinetics could be modeled using two kinetic regimes, much like the previously studied reaction kinetics of TiF_4(g) with SiO_2.[10] Results from microstructural calculations, x-ray diffraction measurements, variations in the path length for gaseous diffusion, and calculation of a mass transfer coefficient were consistent with the initial regime following a chemical reaction control model at the product/gas interface. The second kinetic regime (based on microstructural evolution, shrinking core model fitting, an experiment to determine the porosity of the product layer, and usage of the Wagner model) was consistent with diffusion through a solid-state product layer.

CHAPTER 4 SHAPE PRESERVING CONVERSION OF POROUS ANODIC ALUMINA INTO ALTERNATIVE METAL OXIDES

4.1 Introduction

In this chapter, we describe the ability of reactive conversion processes involving metal fluoride reactants to transform porous anodic aluminum oxide (AAO) into nanostructures comprised of other functional oxides. The objective is to leverage the use of easily-produced Al_2O_3 nanostructures to devices and applications where metal oxides other than Al_2O_3 are optimal materials. This study is limited to semiconducting metal oxides generated by reaction with corresponding, readily-available metal fluorides that are stable as solids at room temperature (but can be heated to yield metal fluoride vapor) for ease of reaction setup and control.

4.2 Thermodynamic Considerations

Multiple considerations must be taken into account before undergoing experimental trials to convert one material into another while maintaining the same aligned pore structure. A primary concern is the thermodynamic favorability of potential reactions. First of all, a significant vapor pressure of the metal fluoride of interest must be able to form at a reasonable temperature (i.e., within the range of temperatures at which the vapor can favorably react with the template without appreciable shape distortions (e.g., due to sintering, grain growth, creep, etc.)). Some materials have too high a boiling or sublimation temperature and may not form a significant vapor pressure in the desired temperature range

(determined by reaction thermodynamics and microstructural evolution). In the present work, a vapor-based reaction is desired to maximize the likelihood of reaction with relatively difficult to reach surfaces (i.e., deep nanopores and high-aspect-ratio nanochannels) before excessive reaction and pore channel plugging (due to an increase in solid volume upon reaction) occurs on other, easier-to-reach surfaces. Additionally, the vapor must be contained within an otherwise inert chamber.

4.2.1 Thermodynamically-favored metal fluoride reactions with Al_2O_3

The following reactions are all thermodynamically favored between 0°C and 600°C (see Table 4.1 for thermodynamic favorability and Table 4.2 for halide species melting, boiling, and sublimation temperatures) and are discussed below.[67]

$$6\ NbF_5(g) + 5\ Al_2O_3 \rightarrow 10\ AlF_3 + 3\ Nb_2O_5 \quad (1)$$

$$2\ SbF_3(g) + Al_2O_3 \rightarrow 2\ AlF_3 + Sb_2O_3 \quad (2)$$

$$3\ SnF_2(g) + Al_2O_3 \rightarrow 2\ AlF_3 + 3\ SnO \quad (3)$$

$$3\ ZrF_4(g) + 2\ Al_2O_3 \rightarrow 4\ AlF_3 + 3\ ZrO_2 \quad (4)$$

$$2\ BiF_3(g) + Al_2O_3 \rightarrow 2\ AlF_3 + Bi_2O_3 \quad (5)$$

Table 4.1. Gibbs Free Energy of Reaction ($\Delta G°_{RXN}$, given in kilojoules) for Formation of the Metal Oxides via Reactions Above at Select Temperatures[67,123,126,127]

		Temperature (°C)			
		0	200	400	600
Reaction (1)	Nb_2O_5	-1790	-1554	-1330	-1116
Reaction (2)	Sb_2O_3	-285	-208	-136	-66
Reaction (3)	SnO	-492	-377	-267	-162
Reaction (4)	ZrO_2	-804	-676	-553	-435
Reaction (5)	Bi_2O_3	-394	-315	-240	-168

Table 4.2. Melting, Boiling, and Sublimation Temperatures of Halide Species

	Melting Point (°C)	Boiling Point (°C)	Sublimation Point (°C)
AlF_3	-	-	1276 [123]
NbF_5	78 [126]	233 [126]	-
SbF_3	292 [127]	345 [127]	-
SnF_2	213 [127]	850 [127]	-
ZrF_4	-	-	912 [67]
BiF_3	725 [67]	900 [67]	-

The exact products of each of the reactions above are only assumed, such products could contain a number of oxyfluorides in addition to, or instead of, the above products. Converting directly and completely from one solid oxide to other solid oxides and fluorides is a good starting point for predicting the likelihood of desirable reactions.

Nb_2O_5 nanostructures are of technological interest in catalysis,[128,129]

photocatalysis,[130] lithium batteries,[131,132] and electrochromic devices.[133] Nb_2O_5 nanotube arrays can be formed by anodization of niobium in NH_4F-glycerol solutions with tube lengths of up to 4 μm (the reaction is self-limiting).[134] Such short tube lengths limits the utility of anodized Nb_2O_5. Also of interest in photocatalytic applications is NbO_2F, which is a potential intermediate product of the reaction with NbF_5.[135] Reactive conversion of Al_2O_3 to form either or both Nb_2O_5 and NbO_2F is not only a favorable reaction (as will be shown later), but also one with potential to impact applications optimized with such structures. NbF_5, the starting fluoride, is a liquid between 78°C and 233°C.[126] One unique constraint in this system is the need to keep liquid NbF_5 out of direct contact with Al_2O_3, as the liquid is also expected to be reactive and could result in poor uniformity of reaction between the alumina channel ends and centers (i.e., the liquid may react more extensively with external surfaces than with internal surfaces). Also, the likelihood of unreacted NbF_5 liquid solidifying upon cooling inside or near the surfaces of the channels could limit the ability to maintain open porous channels.

Sb_2O_3 can be used in catalysis or photodetection.[136-138] It is also known as a flame retardant and could be used in catalytic devices where flammability is a problem.[138,139] It could also be used for humidity sensing.[138] Via anodization, Sb_2O_3 can be formed as a thin porous oxide.[140] While Sb_2O_3 is a relatively low melting oxide (570°C), the fluoride of interest for forming Sb_2O_3, SbF_3, melts at 292°C and boils at 345°C.[127] Thus, because the thermodynamics suggest a favorable conversion of Al_2O_3 into Sb_2O_3 at temperatures between 200°C (where the vapor pressure over SbF_3 is 541 mPa) and 550°C (below the melting temperature of Sb_2O_3), the conversion of Al_2O_3 into solid Sb_2O_3 could be possible.

A third possible new AAO reactive conversion product, SnO_2, is a wide band gap

n-type semiconductor used in applications including sensors, electrocatalysts, and lithium-ion battery anodes.[141-143] Upon anodization, tin forms a porous oxide layer.[144] SnF_2 has a higher vapor pressure at relatively low temperatures than SnF_4.[127] Reaction with SnF_2 is expected to form SnO instead of SnO_2 (a more desirable oxide of tin). If SnO is formed, it could be oxidized to yield SnO_2. SnF_2 melts at 213°C and boils at 850°C.[127] The vapor pressure of SnF_2 reaches 250 mPa at 700°C[127], suggesting temperatures well over the melting point may be necessary to form a critical partial pressure of the fluoride to induce reaction with Al_2O_3.

ZrO_2 nanochannel arrays have many potential applications including anti-corrosion, catalysis, catalysis supports, optoelectronics, and solid-oxide fuel cells.[145,146] Aligned porous zirconia nanochannels have been formed via anodization with channel lengths limited to 4.3 μm (reaction is self-limited).[147] Via the reactive conversion method, longer ZrO_2 nanochannel arrays may be possible, starting with AAO and ZrF_4. This metal fluoride sublimes at a relatively high temperature (i.e., the sublimation temperature of ZrF_4 is 912°C[67]) but forms a vapor pressure over the solid of 0.350 mPa and 944 mPa at 600°C and 900°C, respectively.[67]

A final metal oxide of interest, Bi_2O_3, could be applicable in photocatalysis, solid-oxide fuels cells, or ionic conduction.[148-150] Thin, porous Bi oxides and $BiPO_4$ nanorod arrays have been formed by anodization of Bi.[151,152,153] To date, no known Bi_2O_3 nanochannel arrays have been reported. BiF_3 is a relatively high melting metal fluoride (i.e., the melting point is 725°C[67]) but will form a vapor pressure over the solid of 9.56 mPa at 625°C.[67] This temperature is also below the crystallization temperature of anodic alumina (approximately 900°C).[154]

While AAO conversion reactions to other metal oxides may also be possible, for the sake of space and time, the material in this chapter has been limited to the reactions discussed above.

4.2.2 Containment material and fluoride phase considerations

While the reactions of metal fluorides with Al_2O_3 described in the previous section are thermodynamically possible, other considerations should be taken into account before experiments can be performed. Primarily, the reaction container must be inert and sealable inside an inert atmosphere (e.g., an argon glovebox). Commonly-used materials for creation of inert reaction containers include crimped and welded titanium or steel tubes. However, for each reaction, the chamber material chosen must be checked for inertness with the materials involved in the reaction. Ideally, one can choose titanium, steel, or nickel chambers for each reaction due to their being readily available and easy to weld. The following table lists chamber materials that are compatible with different metal fluorides.

Table 4.3. List of chamber materials compatible with assorted metal fluorides.[67,123,126,127]

ΔG°_{RXN} (kJ) (600°C)	**ΔG°_{RXN} (kJ) (400°C)**	**ΔG°_{RXN} (kJ) (200°C)**	**ΔG°_{RXN} (kJ) (0°C)**	**Potential Reaction**	**Compatible chamber material**	**Metal Fluoride**
479	404	329	253	$2\ NbF_5(g) + 5Ni \rightarrow 5\ NiF_2 + 2Nb$	nickel	NbF_5
751	699	647	595	$4\ SbF_3(g) + 3C \rightarrow 3\ CF_4(g) + 4Sb$	carbon	SbF_3
253	221	186	145	$2\ SnF_2(g) + C \rightarrow\ CF_4(g) + 2Sn$	carbon	SnF_2
256	216	169	113	$4\ BiF_3(g) + 3C \rightarrow 3\ CF_4(g) + 4Bi$	carbon	BiF_3
522	485	447	408	$ZrF_4(g) + 2Ni \rightarrow 2\ NiF_2 + Zr$	nickel	ZrF_4
118	118	104	69	$ZrF_4(g) + Ti \rightarrow TiF_4(g) + Zr$ (TiF_4(s) used below 285°C (TiF_4 sublimation temperature))	titanium	ZrF_4

Other factors to consider are the phases of each fluoride reactant that can form under the reaction conditions. For those fluorides that sublime or will be maintained as a solid with some vapor pressure during reaction, simple physical separation of the fluoride and Al_2O_3 template within the reaction chamber can be made with or without boats containing these reactant materials. For fluorides that melt, more significant containment of the starting fluoride may be conducted to prevent direct Al_2O_3 contact with the melt. Liquid contact may affect the rates of reaction in different areas of the Al_2O_3 material readily accessible or inaccessible to the fluoride, and may result in solidification of unreacted fluoride around the product oxide upon cooling the reaction chamber. This separation can be accomplished by crimping the reaction chamber in the middle with each reactant on a different end, and maintaining the chamber in a '^' (inverted v) shape to prevent reaction with liquids and to promote gas-solid interactions.

Of the fluoride reactants discussed above, several melt and then boil, unlike TiF_4 (studied in the previous chapters) which sublimes. Reactions below the melting or sublimation point of the fluoride were attempted with BiF_3 ($T<725°C$) and ZrF_4 ($T<912°C$), whereas chambers containing NbF_5 were heated above the NbF_5 boiling point (forcing the need for liquid containment). SbF_3 reactions were attempted at temperatures just above and below the boiling point of this fluoride (345°C). Reactions with SnF_2 were performed well above the melting point (213°C) but well below the boiling point (850°C) of this fluoride.

4.3 Experimental Methods

Through-hole anodic aluminum oxide (AAO) was prepared using phosphoric acid as described in Chapter 1. Particular experimental techniques and conditions used for each

reaction are described in the following sections.

4.3.1 Reaction with NbF_5

AAO membranes were placed in nickel shim boats (76 μm thick shim, McMaster-Carr, Atlanta, GA) and introduced into an inert argon atmosphere with an oxygen partial pressure <1 ppm. A nickel ampoule (diameter 15.9 mm, length 20 cm; McMaster-Carr, Cleveland, OH, USA) that contained an excess of NbF_5 (98% purity, Sigma-Aldrich, St. Louis, MO) (at approximately a 4:1 molar ratio of NbF_5 to AAO) near the already welded end was slightly bent near the center to separate the NbF_5 from the end where the AAO membrane would be loaded (to prevent interaction between the AAO and liquid NbF_5 upon heating and cooling of the reaction chamber). The AAO was introduced into the other end of the ampoule which was subsequently crimped and sealed via welding within the inert argon atmosphere. This setup was analogous to the set up described in Figure 1.8 with a crimp in the center of the ampoule.

The ampoule was heated in a horizontal tube furnace to the desired temperature (500°C) at a rate of 5°C/min and held at this temperature for the desired length of time (2 h) to selectively react Al_2O_3 with NbF_5. After cooling ($\leq$5°C/min), the ampoule was removed from the furnace, cut open, and the specimens were extracted for characterization and oxygenation. The specimens were then oxygenated for 4 h to form orthorhombic Nb_2O_5 via a second heat treatment at 600°C in pure, flowing oxygen that, before entering the furnace, was passed through a heated water bath (50°C) at a rate of 1 slpm. The measured humidity (using Model HMP234, Vaisala, Woburn, MA) at the gas outflow of the furnace was found to be at least 94% relative humidity.

Afterwards, the specimens were mounted on glass slides using a thin nitrocellulose-based film (Double Duty nail polish, Sally Hansen) and etched in 3M NaOH for 1.5 h to selectively dissolve all remaining Al-bearing species, including any unreacted AAO and any Al-bearing byproducts. After rinsing, the glass-mounted specimens were then heated in air to 500°C for 0.5 h to pyrolyze the nitrocellulose-based film, resulting in free-standing, aligned Nb_2O_5 nanotube membranes on glass.

4.3.2 Reaction with SnF_2

For reaction with SnF_2, AAO templates were placed in grafoil (thickness 0.76 mm, GrafTech International, Lakewood, OH) boats and introduced into an inert argon atmosphere with an oxygen partial pressure <1 ppm. Nickel ampoules (diameter 15.9 mm, length 20 cm; McMaster-Carr, Cleveland, OH, USA), lined with three layers of grafoil, that contained an excess of SnF_2 (99% purity, Sigma-Aldrich, St. Louis, MO) (approximately 5:1 molar ratio of SnF_2 to AAO) at one end was slightly bent to separate the SnF_2 from the end where the AAO would be loaded (to prevent interaction between the AAO and liquid SnF_2 upon heating and cooling of the reaction chamber). The AAO was introduced into the other end of the grafoil-lined nickel ampoule. Grafoil on either end of the ampoule was crimped with the nickel ampoule, which was subsequently sealed via welding within the inert argon atmosphere.

The ampoule was heated in a horizontal tube furnace to the desired temperature (400°C or 600°C) at a rate of 5°C/min and held at this temperature for the desired length of time (2 h or 6 h) to selectively react Al_2O_3 with SnF_2. After cooling at $\leq$5°C/min, the ampoule was removed from the furnace, cut open, and the specimens were extracted for characterization.

4.3.3 Reaction with BiF_3

AAO templates were placed in grafoil boats and introduced into an inert argon atmosphere with an oxygen partial pressure <1 ppm. The AAO was introduced into the open end of the grafoil-lined nickel ampoule that contained an excess of BiF_3 ($\geq$99.99% purity, Sigma-Aldrich, St. Louis, MO) (approximately 5:1 molar ratio of BiF_3 to AAO). Grafoil was crimped with the nickel ampoule which was subsequently sealed via welding within the inert argon atmosphere.

The ampoule was heated in a horizontal tube furnace to the desired temperature (625°C) at a rate of 5°C/min and held there for the desired length of time (2 h – 8 h) to selectively react Al_2O_3 with BiF_3. After cooling at $\leq$5°C/min, the ampoule was removed from the furnace, cut open, and the specimens were extracted for characterization.

4.3.4 Reaction with SbF_3

AAO templates were placed in grafoil boats and introduced into an inert argon atmosphere with an oxygen partial pressure <1 ppm. A nickel ampoule, lined with three layers of grafoil, that contained an excess of SbF_3 (99.8% purity, Sigma-Aldrich, St. Louis, MO) (approximately 5:1 molar ratio of SbF_3 to AAO), was slightly bent to separate the SbF_3 from the end where the AAO would be loaded (to prevent interaction between the AAO membrane and liquid SbF_3 upon heating and cooling of the reaction chamber. The AAO membrane was introduced into the other end of the grafoil-lined nickel ampoule. Grafoil on either end of the ampoule was crimped with the nickel ampoule which was subsequently sealed via welding within the inert argon atmosphere.

The ampoule was heated in a horizontal tube furnace to the desired temperature

(275°C or 375°C) at a rate of 5°C/min and held at this temperature for the desired length of time (2 h or 8 h) to selectively react Al_2O_3 with SbF_3. After cooling at $\leq$5°C/min, the ampoule was removed from the furnace, cut open, and the specimens were extracted for characterization.

4.3.5 Reactions with ZrF_4

For reaction with ZrF_4, AAO templates were placed in nickel boats and introduced into an inert argon atmosphere with an oxygen partial pressure <1 ppm. The AAO membranes were introduced into the open end of a grafoil-lined titanium ampoule that contained an excess of ZrF_4 (99.9% purity, Sigma-Aldrich, St. Louis, MO) (approximately 4:1 molar ratio of ZrF_4 to AAO) which was subsequently sealed via welding within the inert argon atmosphere.

The ampoule was heated in a horizontal tube furnace to the desired temperature (600°C or 800°C) at a rate of 5°C/min and held at this temperature for the desired length of time (2 h) to selectively react Al_2O_3 with ZrF_4. After cooling at $\leq$5°C/min, the ampoule was removed from the furnace, cut open, and the specimens were extracted for characterization.

4.4 Results and Discussion

4.4.1 Reactive Conversion with NbF_5

TH-PA-AAO templates were partially converted into Nb_2O_5 via a two step-metathetic gas/solid reactive conversion process. The TH-PA-AAO was exposed to NbF_5 vapor in an otherwise inert (Ar) atmosphere and allowed to react for a set length of time, likely following the chemical reaction:

$$3NbF_5(g) + 2Al_2O_3(s) \rightarrow 3NbO_2F(s) + 4AlF_3(s) \quad (6)$$

NbF_5 exists as a solid at room temperature and melts at 78°C.[126] The following analyses confirm the formation of the expected products.

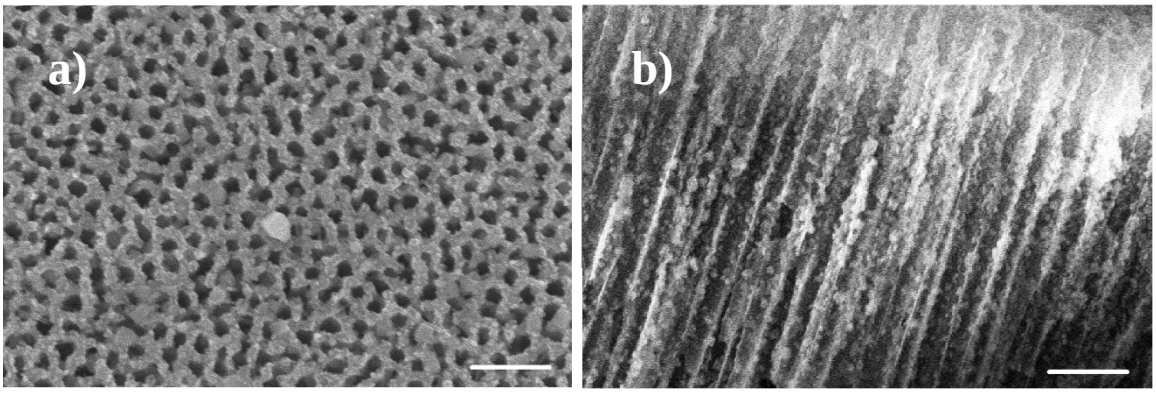

Figure 4.1. SE images of TH-PA-AAO template, after reaction with NbF_5(g) for 2 h at 500°C, viewed top-down (a) and via cross-section (b). Scale bars are 1 μm.

The formation of the NbO_2F/AlF_3 product layer was observed to occur with retention of the nanochanneled template structure after conversion at 500°C for 2 h. The previously smooth TH-PA-AAO surfaces were transformed into more granular, rough surfaces of interconnected crystals upon conversion. Figure 4.1 shows SE images of the top (a) and cross-section (b) of the TH-PA-AAO after reaction with NbF_5 vapor at 500°C for 2 h.

Reaction was apparent by SEM at 500°C. Similar to the reaction of TH-AAO with TiF_4(g) seen in Chapter 1, the reacted layer appears to coarsen and shrink the open diameter of the channels. Completion of the reaction would result in a volume expansion of approximately 230% (powder diffraction files 47-1659 and 07-5087 and density of porous anodic alumina as measured by Nielsch, *et al.*,[70] of 3.2 g/cm^2). Energy dispersive X-ray (EDX) spectroscopy revealed significant amounts of Nb, Al, O, and F in the product (see

Figure 4.2). Also present were phosphorous (due to anodization of aluminum in phosphoric acid) and carbon (from the sample-mounting tape). Upon examination by X-ray diffraction (XRD) analysis, both expected products, NbO_2F and AlF_3 were detected, as shown in Figure 4.3.

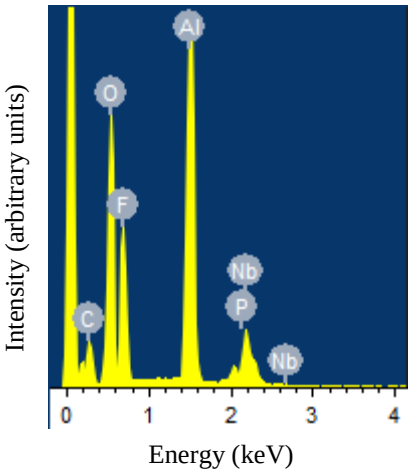

Figure 4.2. EDX spectrum of TH-PA-AAO after 2 h of reaction with NbF_5(g) at 500°C reveals elemental composition of reaction specimens.

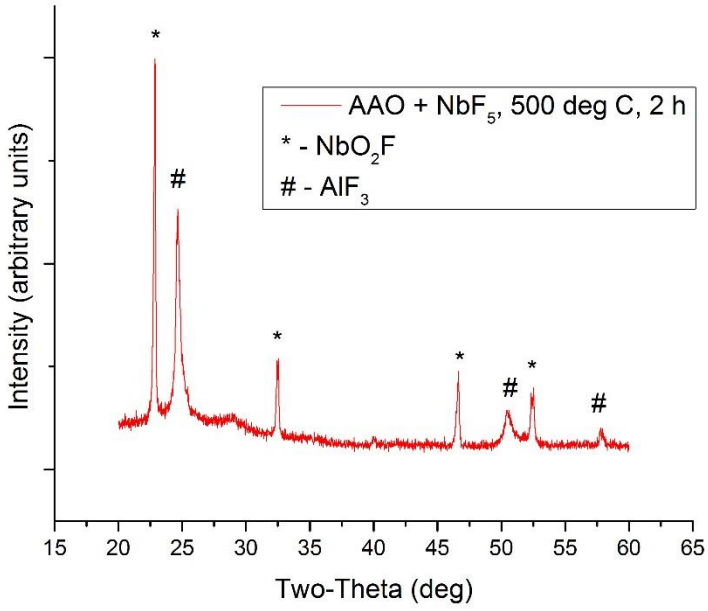

Figure 4.3. XRD showing formation of NbO_2F and AlF_3 after reaction of AAO with NbF_5 at 500°C for 2 h.

To form Nb_2O_5 from the intermediary NbO_2F/AlF_3 products, samples were immersed in deionized water at room temperature for 24 h, oxygenated in humid, flowing oxygen at 600°C for 4 h, and etched in 3 M NaOH for 1.5 h to selectively dissolve remaining Al-bearing species. Figure 4.4 shows the resulting structure by top-down (a) and cross-sectional (b) SEM and confirms the presence of orthorhombic Nb_2O_5 by XRD (c).

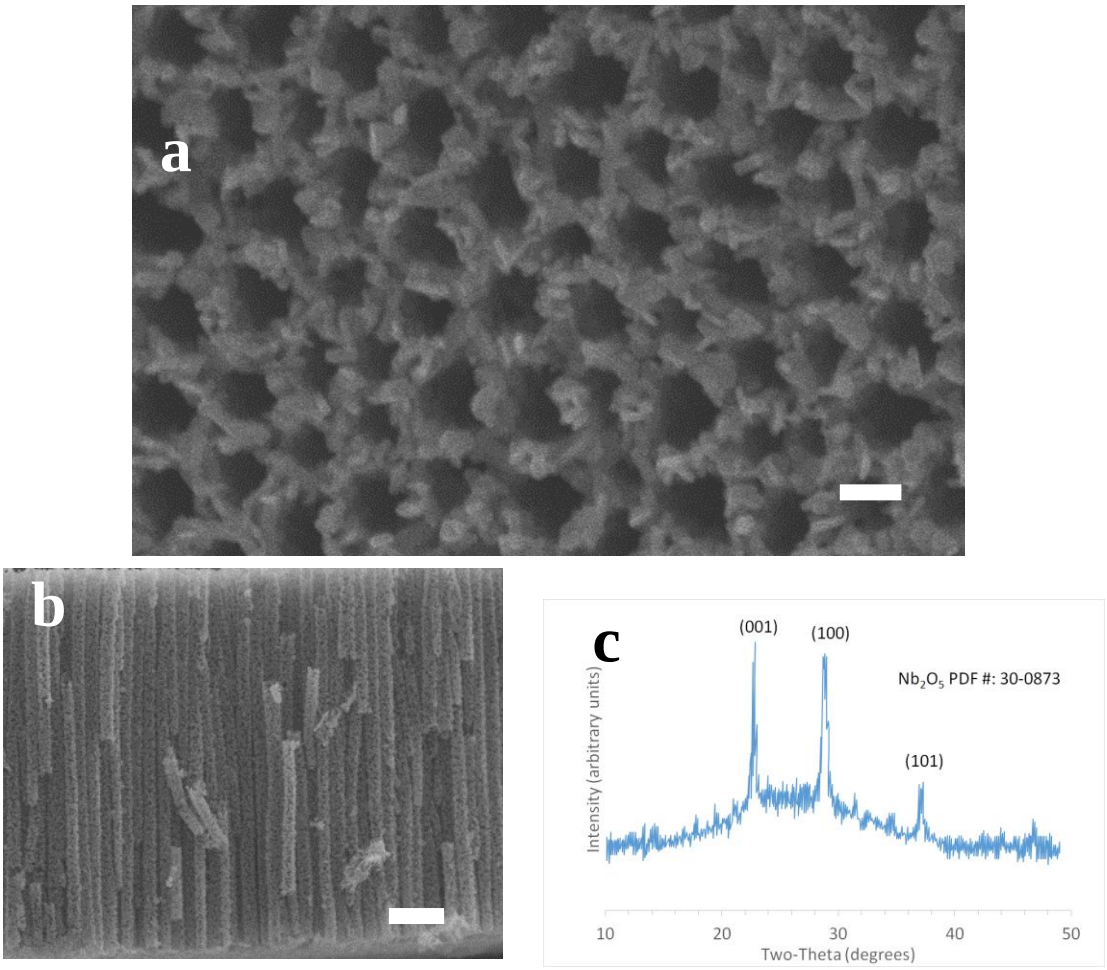

Figure 4.4. (a), (b): SE images after reaction with NbF_5 at 500°C for 2 h, 24 h water soak, oxygenation at 600°C for 4 h, and etching in 3 M NaOH for 1.5 h as view top-down and in cross-section, respectively. (c) X-ray diffraction analysis showing orthorhombic Nb_2O_5 after this reaction, soak, oxygenation, and etch procedure. Scale bars correspond to (a) 200 nm and (b) 1 μm.

4.4.2 Reactive Conversion with SnF_2

Reaction of AAO membranes with SnF_2 was attempted at 600°C for 2 h. Under this condition, reaction was apparent as shown in Figure 4.5. However, a crystalline tin oxide or tin oxyfluoride product did not form. The XRD analyses shown in Figure 4.6 revealed the formation of AlF_3 instead. Energy dispersive X-ray spectroscopy detected approximately 0.5-1% tin near the surface of the anodic alumina, suggesting the tin-

containing product may be amorphous. Thus, due to the likelihood of excessive AlF_3 growth covering the surface of the AAO and preventing further handling of an inner core of tin-bearing product (i.e., liquid-based dissolution of AlF_3 would prevent maintenance of a tin-bearing replica on a substrate), it became apparent that the formation of free standing tin oxide nanotube arrays formed by reactive conversion of AAO was unlikely without significant modifications to the experimental design. Further modifications were not explored.

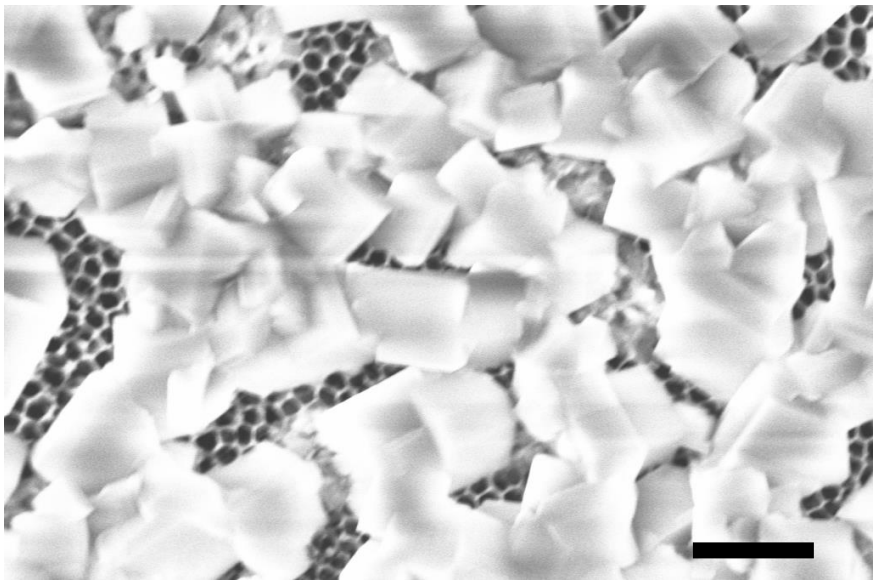

Figure 4.5. SE image after reaction of an AAO membrane with SnF_2(g) at 600°C for 2 h. Scale bar corresponds to 2 μm.

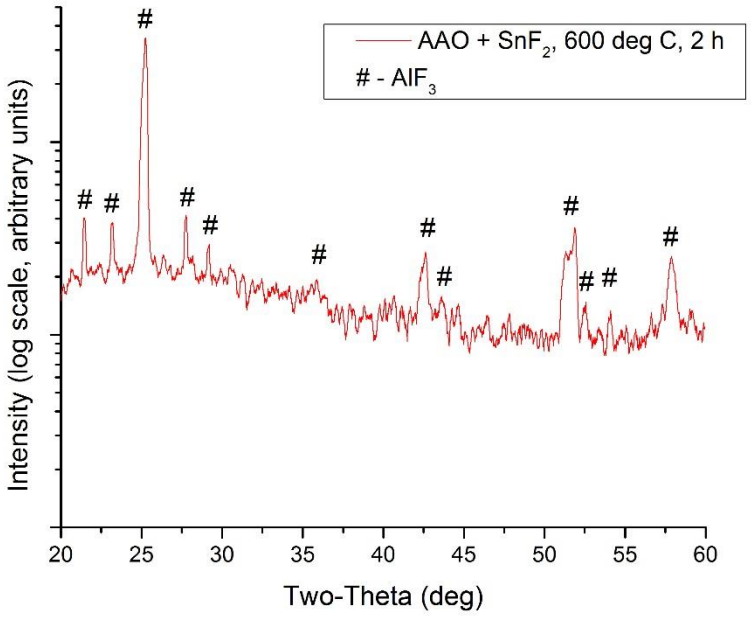

Figure 4.6. XRD analysis showing crystalline AlF_3 following reaction with SnF_2 at 600°C for 2 h.

4.4.3 Reactive Conversion with BiF_3

Reaction of an AAO template with BiF_3 was attempted at 625°C for 2 h. Reaction was visually apparent on the surface of the template (Figure 4.7). SE images revealed large crystals on the surface of the AAO similar to those seen on templates reacted with SnF_2 (see Figure 4.5). XRD analysis proved that AlF_3 had formed and that even though Bi was present in the resulting structure, it had been reduced to pure Bi (Figure 4.8). The most likely cause of the reduction of BiF_3 to Bi was reaction with the outer Ni ampoule, a thermodynamically favorable reaction (see Equation 7 below). Although several layers of graphite (i.e. grafoil) were introduced to separate the BiF_3 from the Ni, the inability to perfectly seal the BiF_3 in grafoil is likely the cause of the reduction to Bi metal. The production of AlF_3 may then be due to the reaction of nickel fluoride (i.e., NiF_2, vapor pressure = $3x10^{-9}$ atm at 625°C, see Equation 8 below) with the AAO, but the relatively

small peaks that could be attributed to NiO but overlap other known products in the XRD analysis and the relatively low NiF_2 vapor pressure at 625°C suggest unidentified reactions may be occurring in this system.

$$2BiF_3(g) + 3Ni \rightarrow 2Bi + 3NiF_2 \qquad \Delta G°_{RXN} = -225 \text{ kJ} \qquad (7)$$

$$3NiF_2(g) + Al_2O_3 \rightarrow 2AlF_3 + 3NiO \qquad \Delta G°_{RXN} = -519 \text{ kJ} \qquad (8)$$

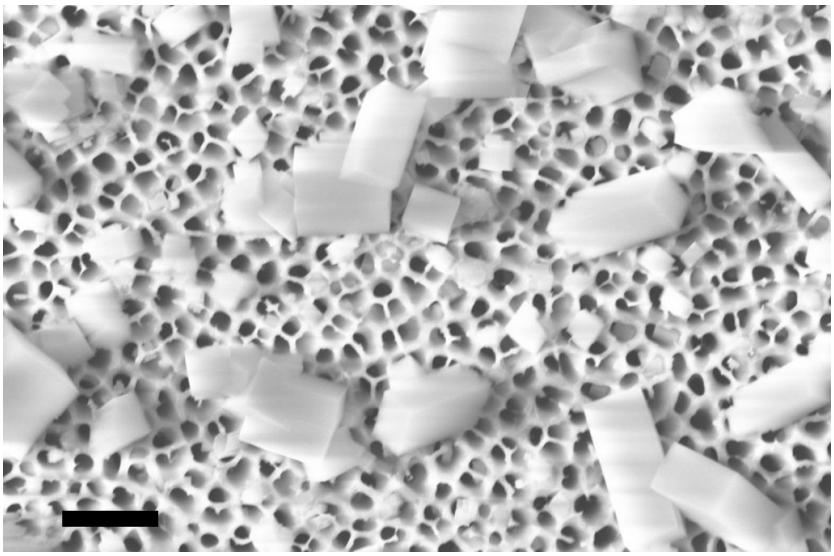

Figure 4.7. SE image of AAO membrane after reaction with BiF_3 at 625°C for 2 h. Scale bar corresponds to 1 μm.

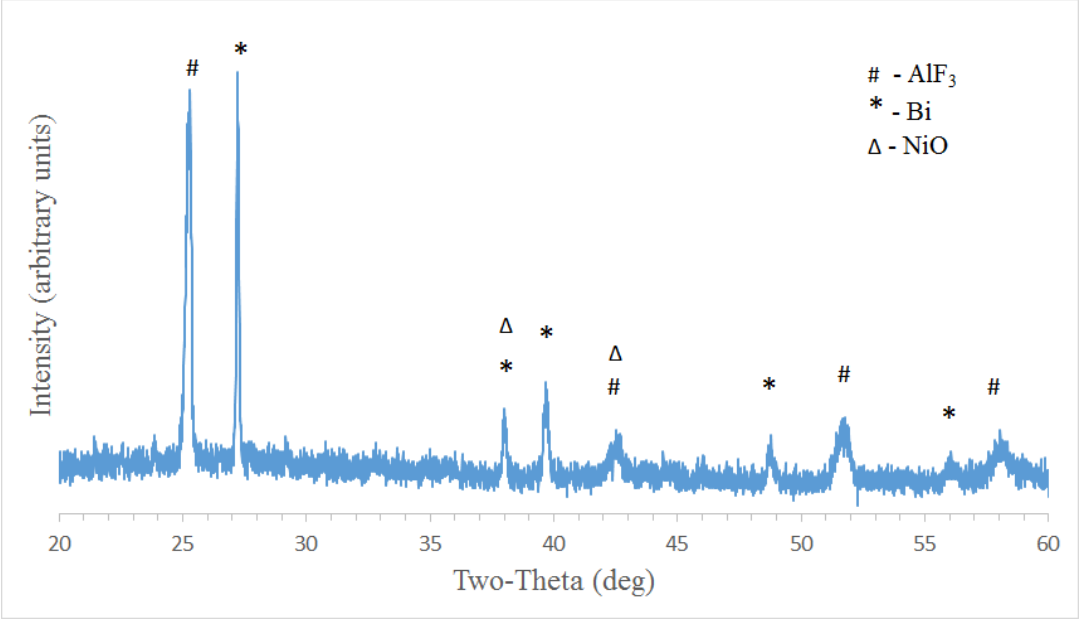

Figure 4.8. XRD pattern of AAO after reaction with BiF_3 at 625°C for 2 h.

4.4.4 Reactive Conversion with SbF_3

AAO was reacted with SbF_3 at 375°C for 8 h. Undesirable reaction was apparent by SEM analysis. A representative SE image after reaction is shown below (Figure 4.9). The channel edges appeared more rough than the starting AAO template (as illustrated previously in Chapter 1), and wire-like growths appear on the surface of the template. EDX revealed a significant accumulation of antimony was present both on the surface of the template and within the pore channels (via EDX analysis on the surface and on a cross-section, Figure 4.10). X-ray diffraction showed that the product included amorphous or nano-crystalline material after reaction. Figure 4.11 illustrates that the X-ray diffraction pattern includes the primary diffraction peak for AlF_3, the assumed by-product. This preliminary result suggested that the antimony-bearing product was amorphous at this temperature.

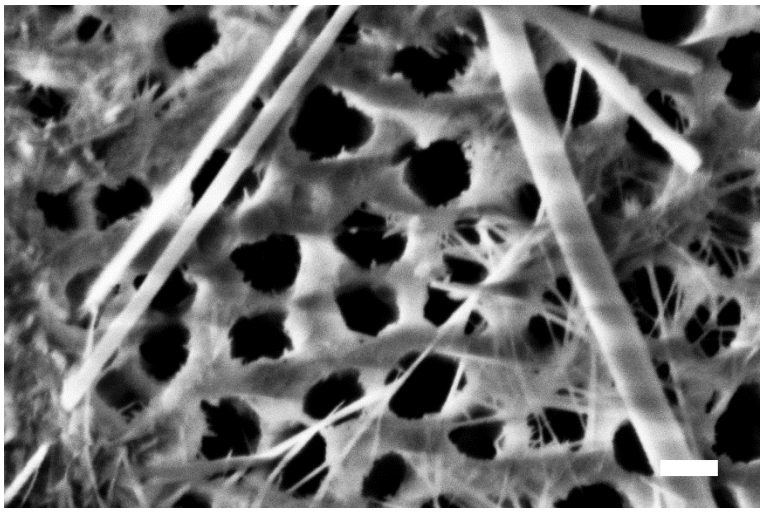

Figure 4.9. SE image illustrating the structure resulting from the reaction of AAO with SbF_3 at 375°C for 8 h. Scale bar corresponds to 200 nm.

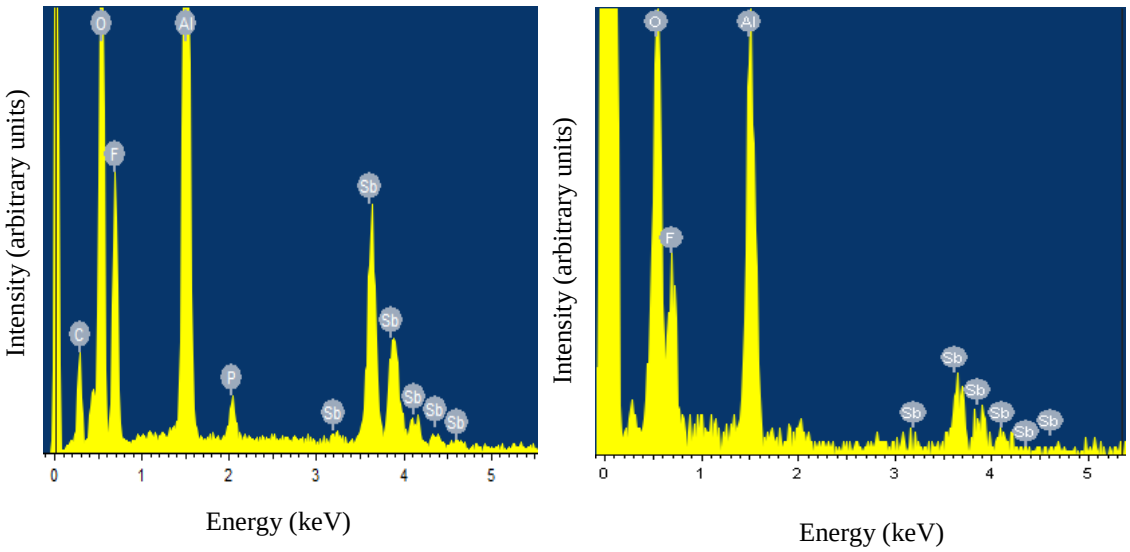

Figure 4.10. EDX reveals the presence of a significant amount of antimony and fluorine on the surface (left) and throughout the thickness (analysis taken near the center of a cross-section shown at right) of the AAO reaction product with SbF_3. Semi-quantitative analyses suggest a ratio between 1:2 and 1:4 Sb antimony to aluminum in the analyzed volumes after reaction at 375 °C for 8 h.

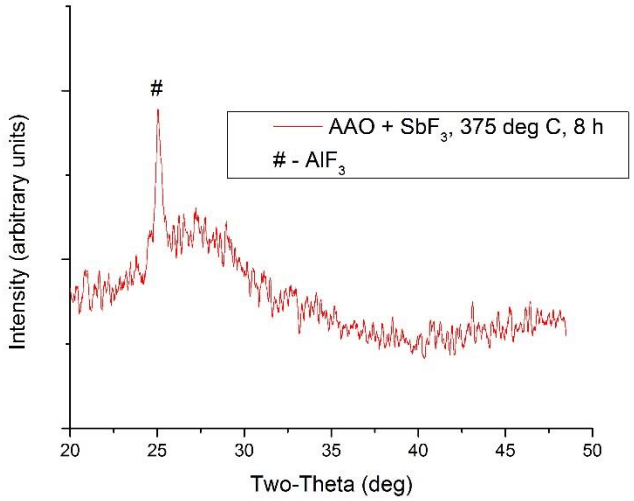

Figure 4.11. X-ray diffraction spectrum of product from the reaction between AAO and SbF_3 at 375°C for 8 h.

4.4.5 Reactive Conversion with ZrF_4

After reaction with ZrF_4(g) at 800°C for 2 h, Al_2O_3 was converted into one or more zirconium oxyfluorides including $ZrF_{3.12}O_{0.44}$, and possibly also $ZrF_{2.67}O_{0.67}$, and $ZrF_{2.46}O_{0.87}$, and crystalline AlF_3 as indicated by the XRD spectrum in Figure 4.12. At this temperature, overgrowth and uneven growth of the product layer was seen by SEM (Figure 4.13). Scaling the reaction back to 600°C for 2 h resulted in AlF_3 crystallites apparent on the surface of the template but no formation of the oxyfluorides seen at 800°C (Figure 4.14). Further refinement of the reaction temperature and time may result in more uniform growth of the products and it is possible that the oxyfluorides will all convert to ZrO_2 upon applying appropriate oxygenation conditions.

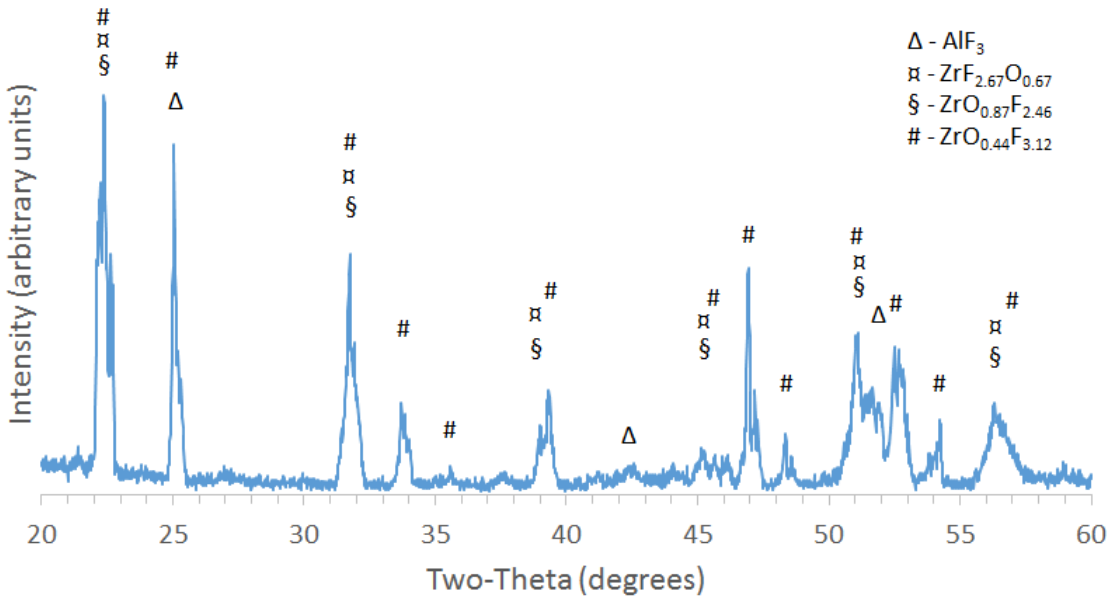

Figure 4.12. X-ray diffraction spectrum of product of reaction between ZrF_4 and AAO at 800°C for 2 h.

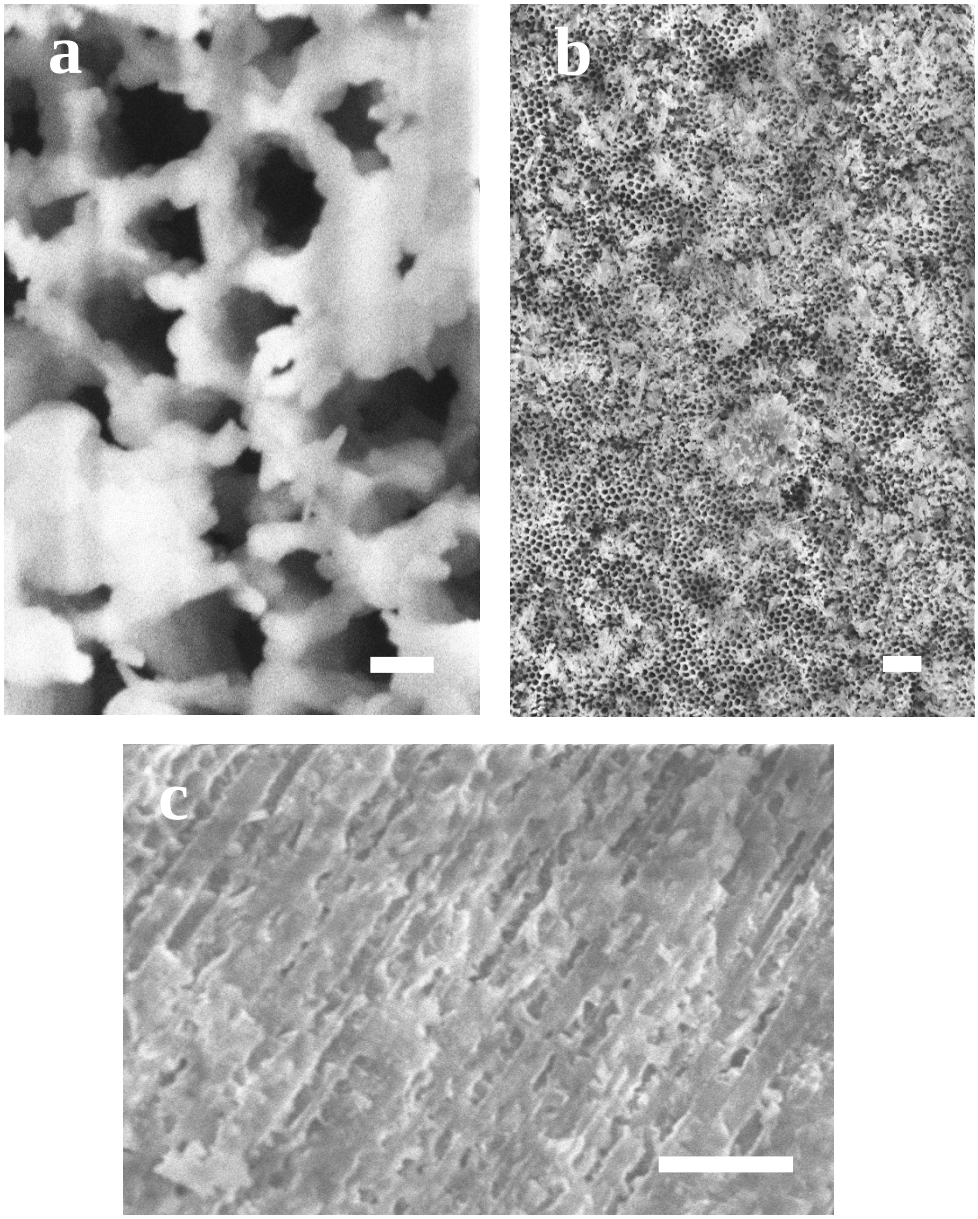

Figure 4.13. SE images taken after reaction of AAO membrane with ZrF_4(g) at 800°C for 2 h. (a) High magnification of the top shows pore channels roughened by reaction. (b) Low magnification of the top shows uneven growth on the surface. (c) Cross-sectional view shows significant reaction inside the pore channels. Scale bars correspond to (a) 200 nm and (b, c) 2 μm.

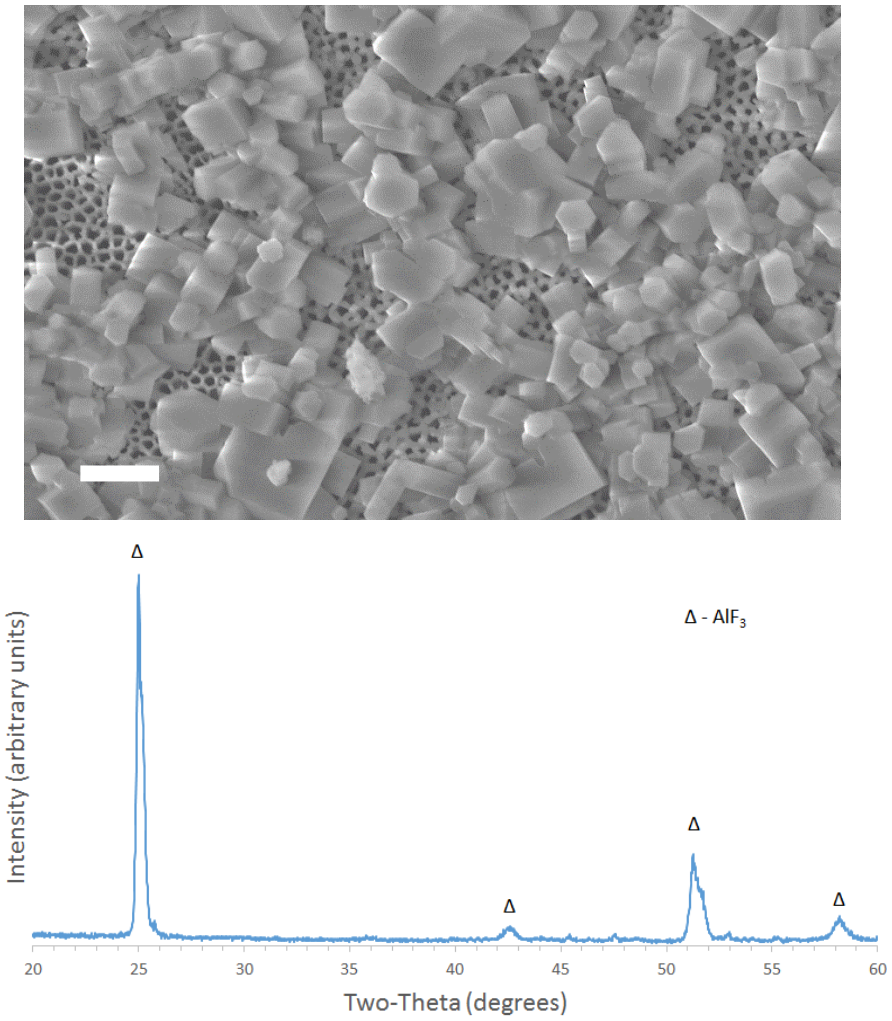

Figure 4.14. SE image and XRD spectrum of AAO membrane after reaction with ZrF_4 at 600°C for 2 h. Scale bar corresponds to 2 μm.

4.5 Conclusions

This chapter has gone beyond the study of the interaction of TiF_4(g) with Al_2O_3 to uncover other potential metal oxide structures that can be formed via gas/solid reactive conversion of Al_2O_3. We have explored the thermodynamics and experimental conditions for the formation of Nb_2O_5, SnO_2, Sb_2O_3, Bi_2O_3, and ZrO_2 from porous anodic Al_2O_3. While shape-preserving chemical conversion was not realized with all of the reactions

examined, we have shown that freestanding Nb_2O_5 nanochannel arrays can be formed from AAO membranes with similar success as was seen in previous chapters with the formation of TiO_2 replicas. Such Nb_2O_5 arrays could be useful in a variety of catalytic and other devices.

APPENDIX A: Calculation of the Diffusion Coefficient of TiF_4(g) in Argon

The diffusion coefficient for TiF_4(g) in argon, assuming both are nonpolar, nonreacting molecules and using the Lennard Jones potential to evaluate the influence of the molecular forces can be calculated using[119]:

$$D_{AB} = \frac{0.001858T^{\frac{3}{2}}\left[\frac{1}{M_A}+\frac{1}{M_B}\right]^{\frac{1}{2}}}{P\sigma_{AB}^2\Omega_D}$$

where D_{AB} is the diffusion coefficient of A through B, in cm^2/s; T is the absolute temperature, in K; M_A and M_B are the molecular weights of A and B, respectively; P is the absolute pressure, in atmospheres; σ_{AB} is the ‘‘collision diameter,’’ a Lennard–Jones parameter, in Å; and Ω_D is the ‘‘collision integral’’ for molecular diffusion, a dimensionless function of $\kappa T/\epsilon_{AB}$; κ is the Boltzmann constant, which is 1.38×10^{-16} ergs/K; and ϵ_{AB} is the energy of molecular interaction for the binary system A and B, a Lennard-Jones parameter, in ergs.

For argon, the values of σ and ϵ_A/κ, are 3.418 Å and 124 K, respectively, as calculated from viscosity data.[119] There is no published data for the Lennard-Jones parameters of TiF_4(g), however, the parameters may be estimated from similar molecules (i.e., same coordination number and comparable atomic radii), such as SiH_4 and $SiCl_4$. Since for SiH_4, σ and ϵ_A/κ, are 4.08 Å and 207.6 K, respectively, and for $SiCl_4$, σ and ϵ_A/κ, are 5.08 Å and 358 K, respectively, the σ and ϵ_A/κ values of TiF_4, by taking the average of that of SiH_4 and $SiCl_4$, are estimated to be ~4.5 Å and ~280 K, respectively.[119] Thus,

$$\sigma_{AB} = \frac{\sigma_A + \sigma_B}{2} = \frac{3.418 + 4.5}{2} = 3.9 \text{ Å}$$

$$\frac{\epsilon_{AB}}{\kappa} = \sqrt{\left(\epsilon_A/\kappa\right)\left(\epsilon_B/\kappa\right)} = \sqrt{124 \times 280} = 186 \text{ K}$$

When T = 310°C =583 K and P = 1atm:

$$\frac{\varepsilon_{AB}}{\kappa T} = \frac{186}{583} = 0.319 \Longrightarrow \frac{\kappa T}{\varepsilon_{AB}} = 3.1$$

Using the function table listing Ω_D as a function of this parameter from Welty[119]:

$$\Omega_D = f\left(\frac{\kappa T}{\varepsilon_{AB}}\right) = f(3.1) = 0.94$$

Since M_{TiF4} = 124 and M_{Ar} = 40, then:

$$D_{AB} = \frac{0.001858(583)^{\frac{3}{2}}\left[\frac{1}{40} + \frac{1}{124}\right]^{\frac{1}{2}}}{1 \times 3.9^2 \times 0.94} = 0.33\,\frac{\text{cm}^2}{\text{s}} = 3.3 \times 10^{-5}\,\frac{\text{m}^2}{\text{s}}$$

REFERENCES

[1] R. Jose, V. Thavasi and S. Ramakrishna. Metal Oxides for Dye-Sensitized Solar Cells, *Journal of the American Ceramic Society*, 2009, **92**, 289-301.

[2] J.D. Berrigan, T. McLachlan, J.R. Deneault, Y. Cai, T.S. Kang, M.F. Durstock and K.H. Sandhage. Conversion of Porous Anodic Al_2O_3 into Freestanding, Uniformly Aligned, Multi-Wall TiO_2 Nanotube Arrays for Electrode Applications, *Journal of Materials Chemistry A*, 2013, **1**, 128-134.

[3] R.R. Unocic, F.M. Zalar, P.M. Sarosi, Y. Cai and K.H. Sandhage. Anatase Assemblies from Algae: Coupling Biological Self-Assembly of 3-D Nanoparticle Structures with Synthetic Reaction Chemistry, *Chem Commun*, 2004, 796-797.

[4] K.H. Sandhage, M.B. Dickerson, P.M. Huseman, M.A. Caranna, J.D. Clifton, T.A. Bull, T.J. Heibel, W.R. Overton and M.E.A. Schoenwaelder. Novel, Bioclastic Route to Self-Assembled, 3d, Chemically Tailored Meso/Nanostructures: Shape-Preserving Reactive Conversion of Biosilica (Diatom) Microshells, *Adv Mater*, 2002, **14**, 429-+.

[5] M.R. Weatherspoon, S.M. Allan, E. Hunt, Y. Cai and K.H. Sandhage. Sol-Gel Synthesis on Self-Replicating Single-Cell Scaffolds: Applying Complex Chemistries to Nature's 3-D Nanostructured Templates, *Chem. Commun.*, 2005, 651-653.

[6] Z. Bao, M.R. Weatherspoon, S. Shian, Y. Cai, P.D. Graham, S.M. Allan, G. Ahmad, M.B. Dickerson, B.C. Church, Z. Kang, H.W. Abernathy, III, C.J. Summers, M. Liu and K.H. Sandhage. Chemical Reduction of Three-Dimensional Silica Micro-Assemblies into Microporous Silicon Replicas, *Nature*, 2008, **446**, 172-175.

[7] S. Shian, Y. Cai, M.R. Weatherspoon, S.M. Allan and K.H. Sandhage. Three-Dimensional Assemblies of Zirconia Nanocrystals Via Shape-Preserving Reactive Conversion of Diatom Microshells, *Journal of the American Ceramic Society*, 2006, **89**, 694-698.

[8] O. Levenspiel, *Chemical Reaction Engineering*, 3rd edn., Wiley, New York, 1999.

[9] K.H. Sandhage, M.B. Dickerson, P.M. Huseman, F.M. Zalar, M.C. Carrol, M.R. Rondon and E.C. Sandhage. Novel Hybrid Route to Chemically-Tailored, Three-Dimensional Oxide Nanostructures: The Basic (Bioclastic and Shape-Preserving Inorganic Conversion) Process, *Ceramic Engineering and Science Proceedings*, 2002, **24**, 653-664.

[10] S. Shian. Shape Preserving Conversion Reaction of Siliceous Structures Using Metal Halides: Properties, Kinetics, and Potential Applications. Ph.D. Dissertation, Georgia Institute of Technology, 2008.

[11] S.J. Lee, C.H. Huang, S. Shian and K.H. Sandhage. Rapid Hydrolysis of Organophosphorous Esters Induced by Nanostructured, Fluorine-Doped Titania Replicas of Diatom Frustules, *Journal of the American Ceramic Society*, 2007, **90**, 1632-1636.

[12] Y. Lin, G.S. Wu, X.Y. Yuan, T. Xie and L.D. Zhang. Fabrication and Optical Properties of TiO_2 Nanowire Arrays Made by Sol–Gel Electrophoresis Deposition into Anodic Alumina Membranes, *Journal of Physics*, 2003, **15**, 2917-2922.

[13] J.M. Macak, H. Tsuchiya, A. Ghicov, K. Yasuda, R. Hahn, S. Bauer and P. Schmuki. TiO_2 Nanotubes: Self-Organized Electrochemical Formation, Properties and Applications, *Curr Opin Solid St M*, 2007, **11**, 3-18.

[14] J. Nowotny, T. Bak, M.K. Nowotny and L.R. Sheppard. Defect Chemistry and Electrical Properties of Titanium Dioxide. 2. Effect of Aliovalent Ions, *J Phys Chem C*, 2008, **112**, 602-610.

[15] O. Diwald, T.L. Thompson, T. Zubkov, E.G. Goralski, S.D. Walck and J.T. Yates, Jr. Photochemical Activity of Nitrogen - Doped Rutile TiO_2 (110) in Visible Light, *J Phys Chem B*, 2004, **108**, 6004-6008.

[16] B. O'Regan and M. Graetzel. A Low-Cost, High-Efficiency Solar Cell Based on Dye-Sensitized Colloidal Titanium Dioxide Films, *Nature*, 1991, **353**, 737-740.

[17] G.K. Mor, O.K. Varghese, M. Paulose, K. Shankar and C.A. Grimes. A Review on Highly Ordered, Vertically Oriented TiO_2 Nanotube Arrays: Fabrication, Material Properties, and Solar Energy Applications, *Solar Energy Materials and Solar Cells*, 2006, **90**, 2011-2075.

[18] J. Park, S. Kim and A. Bard. Novel Carbon-Doped TiO_2 Nanotube Arrays with High Aspect Ratios for Efficient Solar Water Splitting, *Nano Letters*, 2005, **6**, 24-28.

[19] O.K. Varghese, M. Paulose, T.J. Latempa and C.A. Grimes. High-Rate Solar Photocatalytic Conversion of CO_2 and Water Vapor to Hydrocarbon Fuels, *Nano Letters*, 2009, **9**, 731-737.

[20] K. Shankar, G.K. Mor, H.E. Prakasam, O.K. Varghese and C.A. Grimes. Self-Assembled Hybrid Polymer-TiO_2 Nanotube Array Heterojunction Solar Cells, *Langmuir*, 2007, **23**, 12445-12449.

[21] G. Ortiz, I. Hanzu, T. Djenizian, P. Lavela, J. Tirado and P. Knauth. Alternative Li-Ion Battery Electrode Based on Self-Organized Titania Nanotubes, *Chem Mater*, 2008, **21**, 63-67.

[22] G. Armstrong, A.R. Armstrong, P.G. Bruce, P. Reale and B. Scrosati. TiO_2 (B) Nanowires as an Improved Anode Material for Lithium-Ion Batteries Containing $LiFePO_4$ or $LiNi_{0.5}Mn_{1.5}O_4$ Cathodes and a Polymer Electrolyte, *Adv Mater*, 2006, **18**, 2597-2600.

[23] H. Wang, H. Nakamura, M. Uehara, M. Miyazaki and H. Maeda. Preparation of Titania Particles Utilizing the Insoluble Phase Interface in a Microchannel Reactor, *Chem Commun*, 2002, 1462-1463.

[24] J.G. Yu, Y.R. Su and B. Cheng. Template-Free Fabrication and Enhanced Photocatalytic Activity of Hierarchical Macro-/Mesoporous Titania, *Adv Funct Mater*, 2007, **17**, 1984-1990.

[25] J. Yu, S. Liu and H. Ju. Glucose Sensor for Flow Injection Analysis of Serum Glucose Based on Immobilization of Glucose Oxidase in Titania Sol-Gel Membrane, *Biosensors & bioelectronics*, 2003, **19**, 401-409.

[26] S. Huang, H. Efstathiadis and P. Haldar. Fabrication of Nanorod Arrays for Organic Solar Cell Applications, *Mater Res Soc Symp P*, 2005, **836**, 49-53.

[27] X.S. Fang, C.H. Ye, X.S. Peng, Y.H. Wang, Y.C. Wu and L.D. Zhang. Temperature-Controlled Growth of A-Al_2O_3 Nanobelts and Nanosheets, *Journal of Materials Chemistry*, 2003, **13**, 3040-3043.

[28] M.A. Shah. Al_2O_3 Nanobricks Via an Organic Free Route Using Water as Solvent, *International Journal of Manufacturing, Materials, and Mechanical Engineering*, 2011, **1**, 56-61.

[29] P.G. Li, M. Lei and W.H. Tang. Raman and Photoluminescence Properties of $\mathfrak{I}$-Al_2O_3 Microcones with Hierarchical and Repetitive Superstructure, *Materials Letters*, 2010, **64**, 161-163.

[30] G.K. Mor, K. Shankar, M. Paulose, O.K. Varghese and C.A. Grimes. Use of Highly-Ordered TiO_2 Nanotube Arrays in Dye-Sensitized Solar Cells, *Nano Letters*, 2005, **6**, 215-218.

[31] M. Adachi. Synthesis of Morphology-Controlled Titania Nanocrystals and Application for Dye-Sensitized Solar Cells, *Current Nanoscience*, 2007, **3**, 285-295.

[32] T.S. Kang, A.P. Smith, B.E. Taylor and M.F. Durstock. Fabrication of Highly-Ordered TiO_2 Nanotube Arrays and Their Use in Dye-Sensitized Solar Cells, *Nano Letters*, 2009, **9**, 601-606.

[33] J.D. Berrigan, T.S. Kang, Y. Cai, J.R. Deneault, M.F. Durstock and K.H. Sandhage. Protein-Enabled Layer-by-Layer Syntheses of Aligned, Porous-Wall, High-Aspect-Ratio TiO_2 Nanotube Arrays, *Adv Funct Mater*, 2011, **21**, 1693-1700.

[34] N.G. Park, J. van de Lagemaat and A.J. Frank. Comparison of Dye-Sensitized Rutile- and Anatase-Based TiO_2 Solar Cells, *J Phys Chem B*, 2000, **104**, 8989-8994.

[35] M. Gratzel. Highly Efficient Nanocrystalline Photovoltaic Devices. - Charge Transfer Sensitizers Based on Ruthenium and Osmium Achieve Outstanding Performance, *Platinum Metals Review*, 1994, **38**, 151-159.

[36] C.J. Barbe and M. Graetzel. Mesoporous TiO_2 Electrodes for Photovoltaic Applications, *Mat Res S C*, 1996, **431**, 129-134.

[37] C.J. Barbe, F. Arendse, P. Comte, M. Jirousek, F. Lenzmann, V. Shklover and M. Gratzel. Nanocrystalline Titanium Oxide Electrodes for Photovoltaic Applications, *Journal of the American Ceramic Society*, 1997, **80**, 3157-3171.

[38] A. Fujishima and K. Honda. Electrochemical Photolysis of Water at a Semiconductor Electrode, *Nature*, 1972, **238**, 37-38.

[39] M. Matsumura, S. Matsudaira, H. Tsubomura, M. Takata and H. Yanagida. Dye Sensitization and Surface Structures of Semiconductor Electrodes, *Ind. Eng. Chem. Prod. Res. Dev.*, 1980, **19**, 415-421.

[40] Q. Wang, S. Ito, M. Graetzel, F. Fabregat-Santiago, I. Mora-Sero, J. Bisquert, T. Bessho and H. Imai. Characteristics of High Efficiency Dye-Sensitized Solar Cells, *J Phys Chem B*, 2006, **110**, 25210-25221.

[41] C.A. Grimes. Synthesis and Application of Highly Ordered Arrays of TiO_2 Nanotubes, *Journal of Materials Chemistry*, 2007, **17**, 1451-1457.

[42] J. Hagen, W. Schaffrath, P. Otschik, R. Fink, A. Bacher, H.-W. Schmidt and D. Haarer. Novel Hybrid Solar Cells Consisting of Inorganic Nanoparticles and an Organic Hole Transport Material, *Synthetic Materials*, 1997, **89**, 215-220.

[43] M.A. Henderson. A Surface Perspective on Self-Diffusion in Rutile TiO_2, *Surface Science*, 1999, **419**, 174-187.

[44] A. Le Viet, R. Jose, M. Reddy, B. Chowdari and S. Ramakrishna. Nb2o5 Photoelectrodes for Dye-Sensitized Solar Cells: Choice of the Polymorph, *The Journal of Physical Chemistry C*, 2010, **114**, 21795-21800.

[45] F. Lenzmann, J. Krueger, S. Burnside, K. Brooks, M. Grätzel, D. Gal, S. Rühle and D. Cahen. Surface Photovoltage Spectroscopy of Dye-Sensitized Solar Cells with TiO2, Nb2O5, and $SrTiO_3$ Nanocrystalline Photoanodes: Indication for Electron Injection from Higher Excited Dye States, *The Journal of Physical Chemistry B*, 2001, **105**, 6347-6352.

[46] H. Snaith. Estimating the Maximum Attainable Efficiency in Dye-Sensitized Solar Cells, *Adv Funct Mater*, 2010, **20**, 13-19.

[47] J.H. Yoon, S.R. Jang, R. Vittal, J. Lee and K.J. Kim. TiO_2 Nanorods as Additive to TiO_2 Film for Improvement in the Performance of Dye-Sensitized Solar Cells, *J Photoch Photobio A*, 2006, **180**, 184-188.

[48] G. Mor, O. Varghese, M. Paulose, K. Shankar and C. Grimes. A Review on Highly Ordered, Vertically Oriented TiO_2 Nanotube Arrays: Fabrication, Material Properties, and Solar Energy Applications, *Solar Energy Materials and Solar Cells*, 2006, **90**, 2011-2075.

[49] T. Bak, M.K. Nowotny, L.R. Sheppard and J. Nowotny. Mobility of Electronic Charge Carriers in Titanium Dioxide, *J Phys Chem C*, 2008, **112**, 12981-12987.

[50] K.D. Benkstein, N. Kopidakis, J. Van De Lagemaat and A.J. Frank. Influence of the Percolation Network Geometry on Electron Transport in Dye-Sensitized Titanium Dioxide Solar Cells, *J Phys Chem B*, 2003, **107**, 7759-7767.

[51] K.M. Coakley and M.D. McGehee. Photovoltaic Cells Made from Conjugated Polymers Infiltrated into Mesoporous Titania, *Applied Physics Letters*, 2003, **83**, 3380-3382.

[52] T. Ma, M. Akiyama, E. Abe and I. Imai. High-Efficiency Dye-Sensitized Solar Cell Based on a Nitrogen-Doped Nanostructured Titania Electrode, *Nano Letters*, 2005, **5**, 2543-2547.

[53] N.N. Bwana. Use of Photoresist Templates in the Synthesis of Highly-Ordered Arrays of Titania Nanorods, *J Nanopart Res*, 2007, **9**, 1139-1143.

[54] A. Chen, X. Peng and P. Holt-Hindle, in *Frontal Nanotechnology Research*, ed. M. V. Berg, Nova Scence Publishers, Inc., New York, 2007, pp. 131-160.

[55] H.-J. Her, J.-M. Kim, C.J. Kang and Y.-S. Kim. Hybrid Photovoltaic Cell with Well - Ordered Nanoporous Titania - P3HT by Nanoimprinting Lithography, *Journal of Physics and Chemistry of Solids*, 2007, **69**, 1301-1304.

[56] X. Peng and A. Chen. Aligned Tio_2 Nanorod Arrays Synthesized by Oxidizing Titanium with Acetone, *Journal of Materials Chemistry*, 2004, **14**, 2542-2548.

[57] X.M. Song, J.M. Wu, M.Z. Tang, B. Qi and M. Yan. Enhanced Photoelectrochemical Response of a Composite Titania Thin Film with Single-Crystalline Rutile Nanorods Embedded in Anatase Aggregates, *J Phys Chem C*, 2008, **112**, 19484-19492.

[58] E. Joanni, R. Savu, M. de Sousa Góes, P. Bueno, J. de Freitas, A. Nogueira, E. Longo and J. Varela. Dye-Sensitized Solar Cell Architecture Based on Indium–Tin Oxide Nanowires Coated with Titanium Dioxide, *Scripta Materialia*, 2007, **57**, 277-280.

[59] M.S. Sander, M.J. Côté, W. Gu, B.M. Kile and C.P. Tripp. Template-Assisted Fabrication of Dense, Aligned Arrays of Titania Nanotubes with Well-Controlled Dimensions on Substrates, *Adv Mater*, 2004, **16**, 2052-2057.

[60] C. Grimes and G. Mor, *Tio_2 Nanotube Arrays: Synthesis, Properties, and Applications*, Springer, 2009.

[61] A.E.R. Mohamed and S. Rohani. Modified Tio_2 Nanotube Arrays (TNTAs): Progressive Strategies Towards Visible Light Responsive Photoanode, a Review, *Energy Environ. Sci.*, 2011, **4**, 1065-1086.

[62] Y. Zhao, M. Chen, Y. Zhang, T. Xu and W. Liu. A Facile Approach to Formation of through-Hole Porous Anodic Aluminum Oxide Film, *Materials Letters*, 2005, **59**, 40-43.

[63] A.P. Li, F. Müller, A. Birner, K. Nielsch and U. Gösele. Hexagonal Pore Arrays with a 50-420 nm Interpore Distance Formed by Self-Organization in Anodic Alumina, *J. Appl. Phys.*, 1998, **84**, 6023-6026.

[64] O. Jessensky, F. Mueller and U. Goesele. Self-Organized Formation of Hexagonal Pore Arrays in Anodic Alumina, *Applied Physics Letters*, 1998, **72**, 1173–1175.

[65] J.D. Berrigan. Biomimetic and Synthetic Syntheses of Nanostructured Electrode Materials. Ph.D. Dissertation, Georgia Institute of Technology, 2012.

[66] S.-W. Lee, K.-S. Ahn, K. Zhu, N.R. Neale and A.J. Frank. Effects of $Ticl_4$ Treatment of Nanoporous TiO_2 Films on Morphology, Light Harvesting, and Charge-Carrier Dynamics in Dye-Sensitized Solar Cells, *The Journal of Physical Chemistry C*, 2012, **116**, 21285-21290.

[67] I. Barin, *Thermochemical Data of Pure Substances, 3rd Edition*, VCH Verlagsgesellschaft mbH, Weinheim, Germany, 1995.

[68] R.S. Sethu. Reducing Non-Stick on Pad for Wire Bond: A Review, *Australian Journal of Mechanical Engineering*, 2012, **9**, 147-159.

[69] I. Yasui, H. Hagihara and H. Inoue. The Effect of Addition of Oxides on the Crystallization Behavior of Aluminum Fluoride-Based Glasses, *Journal of Non-Crystalline Solids*, 1992, **140**, 130-133.

[70] K. Nielsch, J. Choi, K. Schwirn, R.B. Wehrspohn and U. Gösele. Self-Ordering Regimes of Porous Alumina: The 10 Porosity Rule, *Nano letters*, 2002, **2**, 677-680.

[71] D. Dollimore, D.L. Griffiths and D. Nicholson. 488. The Thermal Decomposition of Oxalates. Part II. Thermogravimetric Analysis of Various Oxalates in Air and in Nitrogen, *Journal of the Chemical Society (Resumed)*, 1963, 2617-2623.

[72] G. Xiong, J.W. Elam, H. Feng, C.Y. Han, H.-H. Wang, L.E. Iton, L.A. Curtiss, M.J. Pellin, M. Kung and H. Kung. Effect of Atomic Layer Deposition Coatings on the Surface Structure of Anodic Aluminum Oxide Membranes, *The Journal of Physical Chemistry B*, 2005, **109**, 14059-14063.

[73] P. Walker and W.H. Tarn, *Crc Handbook of Metal Etchants*, CRC press, 1990.

[74] J.M. Macak, H. Tsuchiya and P. Schmuki. High-Aspect-Ratio TiO_2 Nanotubes by Anodization of Titanium, *Angew. Chem., Int. Ed.*, 2005, **44**, 2100-2102.

[75] C. Ruan, M. Paulose, O.K. Varghese, G.K. Mor and C.A. Grimes. Fabrication of Highly Ordered TiO_2 Nanotube Arrays Using an Organic Electrolyte, *J Phys Chem B*, 2005, **109**, 15754–15759.

[76] K. Zhu, T.B. Vinzant, N.R. Neale and A.J. Frank. Removing Structural Disorder from Oriented TiO_2 Nanotube Arrays: Reducing the Dimensionality of Transport and Recombination in Dye-Sensitized Solar Cells, *Nano Letters*, 2007, **7**, 3739–3746.

[77] S. Shian and K.H. Sandhage. Hexagonal and Cubic $TiOF_2$, *J Appl Crystallogr*, 2010, **43**, 757-761.

[78] C.M. Baldwin and J.D. Mackenzie. Fundamental Condition for Glass Formation in Fluoride Systems, *Journal of the American Ceramic Society*, 1979, **62**, 537–538.

[79] C.M. Baldwin, R.M. Almeida and J.D. Mackenzie. Halide Glasses, *Journal of Non-crystalline Solids*, 1981, **43**, 309–344.

[80] J. Moss and A. Wright. Titanium (IV) Oxydifluoride, *Journal of Fluorine Chemistry*, 1975, **5**, 163-167.

[81] J.R. Deneault, X. Xiao, T.S. Kang, J.S. Wang, C.M. Wai, G.J. Brown and M.F. Durstock. Free-Standing Arrays of Isolated TiO_2 Nanotubes through Supercritical Fluid Drying, *Chemphyschem*, 2012, **13**, 256-260.

[82] J.R. Jennings, A. Ghicov, L.M. Peter, P. Schmuki and A.B. Walker. Dye-Sensitized Solar Cells Based on Oriented TiO_2 Nanotube Arrays: Transport, Trapping, and Transfer of Electrons, *Journal of the American Chemical Society*, 2008, **130**, 13364–13372.

[83] A. Hagfeldt, G. Boschloo, L. Sun, L. Kloo and H. Pettersson. Dye-Sensitized Solar Cells, *Chemical reviews*, 2010, **110**, 6595-6663.

[84] K.H. Sandhage, M.B. Dickerson, P.M. Huseman, F.M. Zalar, M.C. Carroll, M.R. Rondon and E.C. Sandhage, in *26th Annual Conference on Composites, Advanced Ceramics, Materials, and Structures: B: Ceramic Engineering and Science Proceedings*, John Wiley & Sons, Inc., 2008, pp. 653-664.

[85] T.M. McLachlan, 2013.

[86] B.J. Chen, M.A. Rodriguez, S.T. Misture and R.L. Snyder. Effect of Undercooling Temperature on the Solidification Kinetics and Morphology of Y-Ba-Cu-O During Melt Texturing, *Physica C*, 1993, **217**, 367-375.

[87] C. Lind, A.P. Wilkinson, C.J. Rawn and E.A. Payzant. Kinetics of the Cubic to Trigonal Transformation in $ZrMo_2O_8$ and Their Dependence on Precursor Chemistry, *Journal of Materials Chemistry*, 2002, **12**, 990-994.

[88] A.K. Sheridan and J. Anwar. Kinetics of the Solid-State Phase Transformation of Form Beta to Gamma of Sulfanilamide Using Time-Resolved Energy-Dispersive X-Ray Diffraction, *Chem Mater*, 1996, **8**, 1042-1051.

[89] A. Wilkinson, J. Speck, A. Cheetham, S. Natarajan and J. Thomas. In Situ X-Ray Diffraction Study of Crystallization Kinetics in $PbZr_{1-X}Ti_xO_3$, (PZT, X = 0.0, 0.55, 1.0), *Chem Mater*, 1994, **6**, 750-754.

[90] P. Norby, A. Norlund Christensen and J.C. Hanson. Crystallization in Nonaqueous Media of Co- and Mn-Substituted Microporous Aluminophosphates Investigated by in Situ Synchrotron X-Ray Powder Diffraction, *Inorg Chem*, 1999, **38**, 1216-1221.

[91] M.D. Dolan and S.T. Misture. A High-Temperature Diffraction Study of Reduction and Reoxidation of Nickel Oxide, *Rigaku Journal*, 2004, **21**, 12-16.

[92] M. Ozawa and C.K. Loong. In Situ X-Ray and Neutron Powder Diffraction Studies of Redox Behavior in CeO_2-Containing Oxide Catalysts, *Catalysis Today*, 1999, **50**, 329-342.

[93] N. Wakiya, S.Y. Chun, K. Shinozaki and N. Mizutani. Redox Reaction of Praseodymium Oxide in the ZnO Sintered Ceramics, *Journal of Solid State Chemistry*, 2000, **149**, 349-353.

[94] S. Shian and K. Sandhage. A Gas-Tight Cu K Alpha X-Ray Transparent Reaction Chamber for High-Temperature X-Ray Diffraction Analyses of Halide Gas/Solid Reactions, *Review of Scientific Instruments*, 2009, **80**, 115108.

[95] M.S. Haluska, R. Snyder, K.H. Sandhage and S. Misture. Closed, Heated Reaction Chamber Design for Dynamic High-Temperature X-Ray-Diffraction Analyses of Gas/Solid Displacement Reactions, *Review of Scientific Instruments*, 2005, **76**, 126101/126101-126101/126104.

[96] D.R. Lide, *Handbook of Chemistry and Physics*, 77th ed. edn., CRC Press, Inc., Roca Baton, 1996.

[97] K.P. Almtoft, J. Bottiger, J. Chevallier, N. Schell and R.M.S. Martins. Influence of the Substrate Bias on the Size and Thermal Stability of Grains in Magnetron-Sputtered Nanocrystalline Ag Films, *J. Mater. Res.*, 2005, **20**, 1071-1080.

[98] V.A. Kyun and G.T. Roslik. Selection of Material for the Window of the Radiation Chamber During the X-Ray Spectral Analysis of Slurries and Solutions, *Zavodskaya Laboratoriya*, 1976, **42**, 948-949.

[99] J.H. Hubbell and S.M. Seltzer, Ionizing Radiation Div., National Inst. of Standards and Technology, Gaithersburg, MD, 1995.

[100] J. Lützenkirchen. Specific Ion Effects at Two Single-Crystal Planes of Sapphire, *Langmuir*, 2013, **29**, 7726-7734.

[101] R.J. Kershner, J.W. Bullard and M.J. Cima. Zeta Potential Orientation Dependence of Sapphire Substrates, *Langmuir*, 2004, **20**, 4101-4108.

[102] M. Mastro, J. Freitas, R. Holm, C. Eddy, J. Caldwell, K. Liu, O. Glembocki, R. Henry and J. Kim. Rare-Earth Chloride Seeded Growth of Gan Nano-and Micro-Crystals, *Applied surface science*, 2007, **253**, 6157-6161.

[103] S. Han, X. Liu and C. Zhou. Template-Free Directional Growth of Single-Walled Carbon Nanotubes on A- and R-Plane Sapphire, *Journal of the American Chemical Society*, 2005, **127**, 5294-5295.

[104] P.A. Stampe, M. Bullock, W.P. Tucker and J.K. Robin. Growth of MgO Thin Films on M-, A-, C- and R -Plane Sapphire by Laser Ablation, *Journal of Physics D: Applied Physics*, 1999, **32**, 1778.

[105] A.R. Drews. Calibration of a High Temperature X-Ray Diffraction Stage by Differential Thermal Expansion, *Advances in X-ray Analysis*, 2001, **44**, 44-49.

[106] R. Young. Introduction to the Rietveld Method, *The Rietveld Method*, 1993, **5**, 1-38.

[107] A. Beer. Bestimmung Der Absorption Des Rothen Lichts in Farbigen Flüssigkeiten, *Annalen der Physik*, 1852, **162**, 78-88.

[108] B.D. Cullity and S.R. Stock, *Elements of X-Ray Diffraction*, Prentice Hall, 2001.

[109] J.H. Hubbell and S.M. Seltzer, Physical Measurement Laboratory, National Institute of Standards and Technology, Gaithersburg, MD, USA, 2009.

[110] J. Szekely, J.W. Evans and F.Y. Sohn, *Gas-Solid Reactions*, Academic Press, New York, 1976.

[111] P.A. Ramachandran and L.K. Doraiswamy. Modeling of Noncatalytic Gas-Solid Reactions, *AIChE J.*, 1982, **28**, 881-900.

[112] S.K. Bhatia and D.D. Perlmutter. A Random Pore Model for Fluid-Solid Reactions: I. Isothermal, Kinetic Control, *AIChE J.*, 1980, **26**, 379-386.

[113] N. Karatepe, N. Erdoğan, A. Ersoy-Meriçboyu and S. Küçükbayrak. Preparation of Diatomite/$Ca(OH)_2$ Sorbents and Modelling Their Sulphation Reaction, *Chem Eng Sci*, 2004, **59**, 3883-3889.

[114] J. Park and O. Levenspiel. The Crackling Core Model for the Reaction of Solid Particles, *Chem Eng Sci*, 1975, **30**, 1207-1214.

[115] W.V. Schulmeyer and H.M. Ortner. Mechanisms of the Hydrogen Reduction of Molybdenum Oxides, *Int J Refract Met H*, 2002, **20**, 261-269.

[116] R.E. Carter. Kinetic Model for Solid-State Reactions, *J Chem Phys*, 1961, **34**, 2010-2015.

[117] C. Wen. Noncatalytic Heterogeneous Solid-Fluid Reaction Models, *Industrial & Engineering Chemistry*, 1968, **60**, 34-54.

[118] M. Ishida and C. Wen. Comparison of Zone-Reaction Model and Unreacted-Core Shrinking Model in Solid—Gas Reactions—I Isothermal Analysis, *Chem Eng Sci*, 1971, **26**, 1031-1041.

[119] J. Welty, *Fundamentals of Momentum, Heat, and Mass Transfer*, Wiley, 2001.

[120] E.L. Cussler and E.L. Cussler, *Fundamentals of Mass Transfer Diffusion*, Cambridge University Press, 2009.

[121] C. Wagner. Contribution to the Theory of Formation of Oxidation Films, *Z. Physik. Chem. B*, 1933, **21**, 25.

[122] W. Jost, *Diffusion in Solids, Liquids, Gases*, Academic Press, Inc., New York, 1952.

[123] M.W. Chase, American Institute of Physics, -1, 1998.

[124] J. Machin and D. Deadmore. Thermal Stability of Titanium Dioxide, *Nature*, 1961, **189**, 223-224.

[125] G. Dittmer and U. Niemann. Evaluation of Thermodynamic Data on Zirconium and Hafnium Halides and Oxyhalides by Means of Transport Experiments, 1987.

[126] Landolt-Börnstein, ed. S. G. T. E. (SGTE), Springer-Verlag, Berlin-Heidelberg, 1999, vol. Part 1.

[127] O. Knacke, O. Kubaschewski and K. Hesselmann, *Thermochemical Properties of Inorganic Substances*, Springer Berlin, 1991.

[128] M. Ziolek. Niobium-Containing Catalysts—the State of the Art, *Catalysis Today*, 2003, **78**, 47-64.

[129] Y. Rao, M. Trudeau and D. Antonelli. Sulfated and Phosphated Mesoporous Nb Oxide in the Benzylation of Anisole and Toluene by Benzyl Alcohol, *Journal of the American Chemical Society*, 2006, **128**, 13996-13997.

[130] X. Chen, T. Yu, X. Fan, H. Zhang, Z. Li, J. Ye and Z. Zou. Enhanced Activity of Mesoporous Nb_2O_5 for Photocatalytic Hydrogen Production, *Applied surface science*, 2007, **253**, 8500-8506.

[131] A.L. Viet, M. Reddy, R. Jose, B. Chowdari and S. Ramakrishna. Nanostructured Nb_2O_5 Polymorphs by Electrospinning for Rechargeable Lithium Batteries, *The Journal of Physical Chemistry C*, 2009, **114**, 664-671.

[132] M. Wei, K. Wei, M. Ichihara and H. Zhou. Nb_2o_5 Nanobelts: A Lithium Intercalation Host with Large Capacity and High Rate Capability, *Electrochemistry Communications*, 2008, **10**, 980-983.

[133] C.G. Granqvist, *Handbook of Inorganic Electrochromic Materials*, Elsevier, 1995.

[134] W. Wei, K. Lee, S. Shaw and P. Schmuki. Anodic Formation of High Aspect Ratio, Self-Ordered Nb_2O_5 Nanotubes, *Chem Commun*, 2012, **48**, 4244-4246.

[135] T. Murase, H. Irie and K. Hashimoto. Ag+-Inserted NbO_2F as a Novel Photocatalyst, *The Journal of Physical Chemistry B*, 2005, **109**, 13420-13423.

[136] S.S. El-Egamy. Electrochemical Behavior of Antimony and Antimony Oxide Films in Acid Solutions, *Corrosion*, 2006, **62**, 739-744.

[137] L. Li, Y.X. Zhang, X.S. Fang, T.Y. Zhai, M.Y. Liao, H.Q. Wang, G.H. Li, Y. Koide, Y. Bando and D. Golberg. Sb_2o_3 Nanobelt Networks for Excellent Visible-Light-Range Photodetectors, *Nanotechnology*, 2011, **22**, 165704.

[138] H. Chin, K. Cheong and K. Razak. Review on Oxides of Antimony Nanoparticles: Synthesis, Properties, and Applications, *Journal of Materials Science*, 2010, **45**, 5993-6008.

[139] L. Chen and Y.Z. Wang. A Review on Flame Retardant Technology in China. Part I: Development of Flame Retardants, *Polymers for Advanced Technologies*, 2010, **21**, 1-26.

[140] I. Ammar and A. Saad. Anodic Oxide Film on Antimony: I. Role of Experimental Conditions and Growth Kinetics in Acid Media, *Journal of Electroanalytical Chemistry and Interfacial Electrochemistry*, 1971, **30**, 395-406.

[141] N. Barsan, M. Schweizer-Berberich and W. Göpel. Fundamental and Practical Aspects in the Design of Nanoscaled SnO_2 Gas Sensors: A Status Report, *Fresenius' journal of analytical chemistry*, 1999, **365**, 287-304.

[142] A. Kowal, M. Li, M. Shao, K. Sasaki, M. Vukmirovic, J. Zhang, N. Marinkovic, P. Liu, A. Frenkel and R. Adzic. Ternary $Pt/Rh/Sno_2$ Electrocatalysts for Oxidizing Ethanol to CO_2, *Nat. Mater.*, 2009, **8**, 325-330.

[143] X.W. Lou, J.S. Chen, P. Chen and L.A. Archer. One-Pot Synthesis of Carbon-Coated SnO_2 Nanocolloids with Improved Reversible Lithium Storage Properties, *Chem Mater*, 2009, **21**, 2868-2874.

[144] H.C. Shin, J. Dong and M. Liu. Porous Tin Oxides Prepared Using an Anodic Oxidation Process, *Adv Mater*, 2004, **16**, 237-240.

[145] S.-Z. Chu, Y. Hitoshi, H. Segawa, S. Inoue and K. Wada, Meeting Abstracts, 2012.

[146] J.R. Wilson, J.S. Cronin and S.A. Barnett. Linking the Microstructure, Performance and Durability of Ni-Yttria-Stabilized Zirconia Solid Oxide Fuel Cell Anodes

Using Three-Dimensional Focused Ion Beam–Scanning Electron Microscopy Imaging, *Scripta Materialia*, 2011, **65**, 67-72.

[147] S. Berger, F. Jakubka and P. Schmuki. Formation of Hexagonally Ordered Nanoporous Anodic Zirconia, *Electrochemistry Communications*, 2008, **10**, 1916-1919.

[148] L. Zhou, W. Wang, H. Xu, S. Sun and M. Shang. Bi_2O_3 Hierarchical Nanostructures: Controllable Synthesis, Growth Mechanism, and Their Application in Photocatalysis, *Chemistry-A European Journal*, 2009, **15**, 1776-1782.

[149] Y. Leng and S. Chan. Anode-Supported Sofcs with Y_2O_3-doped Bi_2O_3⁄ Gd_2O_3-Doped CeO_2 Composite Electrolyte Film, *Electrochem. Solid-State Lett.*, 2006, **9**, A56-A59.

[150] G. Paściak, J. Chmielowiec and P. Bujło. New Ceramic Superionic Materials for IT-SOFC Applications, *Materials Science-Poland*, 2005, **23**, 209-219.

[151] I. Kanazirski, M. Bojinov and A. Girginov. Electrical Properties of the Barrier Layer/Solution Interface and Its Role During Breakdown of Anodic Bismuth Oxide Films, *Electrochimica acta*, 1993, **38**, 511-517.

[152] D. Williams and G. Wright. Structure and Electronic Properties of Bismuth Anodic Oxide Films—I. Photoeffects, *Electrochimica Acta*, 1979, **24**, 1179-1187.

[153] Z. Zhang, D. Gekhtman, M.S. Dresselhaus and J.Y. Ying. Processing and Characterization of Single-Crystalline Ultrafine Bismuth Nanowires, *Chem Mater*, 1999, **11**, 1659-1665.

[154] M.M. Zamora and J. Saniger. Thermal Evolution of Porous Anodic Aluminas: A Comparative Study, *Revista Mexicana de Física*, 2005, **51**, 502-509.